GEODYNAMIC DEVELOPMENT OF THE SOUTH CHINA BLOCK FROM PRECAMBRIAN TO CRETACEOUS: CONSTRAINTS FROM GEOLOGY GEOCHEMISTRY AND GEOCHRONOLOGY

A Thesis Submitted to the College of

Graduate and Postdoctoral Studies

In Partial Fulfillment of the Requirements

For the Degree of Master of Science

In the Department of Geological Sciences

University of Saskatchewan

Saskatoon

By

YUXIN MAO

PERMISSION TO USE

In presenting this thesis in partial fulfillment of the requirements for a Postgraduate degree from the University of Saskatchewan, I agree that the Libraries of this University may make it freely available for inspection. I further agree that permission for copying of this thesis in any manner, in whole or in part, for scholarly purposes may be granted by the professor or professors who supervised my thesis work or, in their absence, by the Head of the Department or the Dean of the College in which my thesis work was done. It is understood that any copying or publication or use of this thesis or parts thereof for financial gain shall not be allowed without my written permission. It is also understood that due recognition shall be given to me and to the University of Saskatchewan in any scholarly use which may be made of any material in my thesis. Requests for permission to copy or to make other uses of materials in this thesis/dissertation in whole or part should be addressed to:

Head of the Department of Geological Sciences
University of Saskatchewan
114 Science Place
Saskatoon, Saskatchewan S7N 5E2 Canada

OR

Dean
College of Graduate and Postdoctoral Studies
University of Saskatchewan
116 Thorvaldson Building, 110 Science Place
Saskatoon, Saskatchewan S7N 5C9 Canada

ABSTRACT

The geo-tectonic evolution of the South China block is subject to debate. Most articles tend to subdivide the South China block into two sub-ordinate blocks (Yangtze and Cathaysia), with a central Sibao (Jiangnan) Orogen, although there are also suggestions for a separate eastern (Tolo) block. Debate primarily occurs around the timing of amalgamation of the Yangtze and Cathaysia blocks and the processes causing various episodes of magmatism. Some publications indicate that the South China block amalgamated between 800 and 900 Ma, but others propose amalgamation between 400 and 500 Ma. A recent paper suggests that the eastern portion of Cathaysia only collided with Cathaysia in the Jurassic. In this project, we bring together multiple data sets to develop a more constrained plate tectonic model for the South China block between ~1000 Ma and ~100 Ma. Compiled data include: zircon geochronology data, whole rock Lu-Hf isotope data, whole rock Sm-Nd and Rb-Sr isotopes data, rock major and trace element data. Geochronology data concentrate on U-Pb zircon and monazite data for the crystallisation ages of igneous rocks and near-peak metamorphism although lower-temperature closure ages have also been compiled where included in papers on crystallisation and metamorphism. Detrital zircon U-Pb data have also been compiled to aid in understanding changing sources of sediments through time to further constrain potential geodynamic processes. Lithochemistry data are used to infer geodynamic setting for igneous activity or for protolith formation. Together, these various data permit one to distinguish between upper and lower plate settings and to identify rifted environments. Precise location information is captured where available or approximated from published diagrams, correlated with available geological GIS maps.

U-Pb and Sm-Nd isotope data for rocks formed between 900 and 800 Ma demonstrate primarily juvenile sources whereas the 400 to 500 Ma igneous activity reworked substantially older crust. Detrital zircon data show that the grains from South China block are primarily self-sourced. The combined data thus support models inferring collision of Cathaysia with Yangtze between 900 and 800 Ma and later SCB collide with potentially Australia at ~400 Ma.

TABLE OF CONTENTS

LIST OF FIGURES

CHAPTER 1
INTRODUCTION

1.1 Major tectonic blocks of the South China block

China's major continental blocks consist of the Tarim block, North China block, and South China block (Ma et al., 2002). No digital GIS map of the geology of China is available because the Chinese government does not permit release of such maps. Paper copies of geological maps for China (Ma et al., 2002) and Asia (Petrov et al., 2014; Ren, 2013) are available, and were considered when investigating the geology of the different blocks. No geological map diagrams are included in this thesis because it was not possible to customize diagrams to illustrate specific, relevant aspects of the geology. Figure 1.1 illustrates the position of the South China block (hereafter referred to as SCB) in Asia. The SCB has been further subdivided into Yangtze, Cathaysia, Qinling-Dabie, Sulu and Tolo blocks to facilitate explaining the geological history of this area and to describe the movement of SCB. In Figure 1.1, the blocks in the study area are marked as colours which are distinct from other blocks in Asia. SCB's adjacent blocks include: North China block, and Indochina block; these two blocks are also marked as some samples in this study were compiled for these blocks where appropriate to aid in understanding development of the SCB. The boundary between the South China block and North China block is still under debate (Faure et al., 2001; Wu et al., 2004). The Qinling-Dabie orogenic belt and the Sulu block are considered as two suture zones resulting from the collision of the SCB with the North China block as many high pressure metamorphic rocks are found in these areas (Faure et al., 2001). The southwest boundary of the SCB is the Red River fault zone between SCB and the Indochina block (Chen et al., 2017). Additionally, Figure 1.1 illustrates the Jiangnan Orogen in the middle of the SCB, which is suggested by many published articles (Chen et al., 2013; Li et al., 2016; Li et al., 2016; Li et al., 2008; Liu et al., 2012). The boundary between Yangtze and Cathaysia block is inside the Jiangnan Orogen and has not been strictly defined(Yu et al., 2017). The comparison of blocks that assembled the SCB is discussed in later chapters, where igneous (Chapter 3), metamorphic (Chapter 4) and detrital data (Chapter 5) are applied to identify differences between each block. These data are also used to more precisely define the boundary of each of the blocks in this study.

In this thesis, the constraints of tectonic histories are derived from igneous, sedimentary, and metamorphic rock sample data for the following aspects: lithochemistry, geochronology and isotope geochemistry. Igneous and metamorphic geochronology constrains the location of igneous belts and collision zones, respectively, so aiding understanding of the tectonic history of the SCB. Detrital zircon data are also compiled to understand the possible provenance of the sediments and to further understand the position of the SCB relative to other crustal blocks.

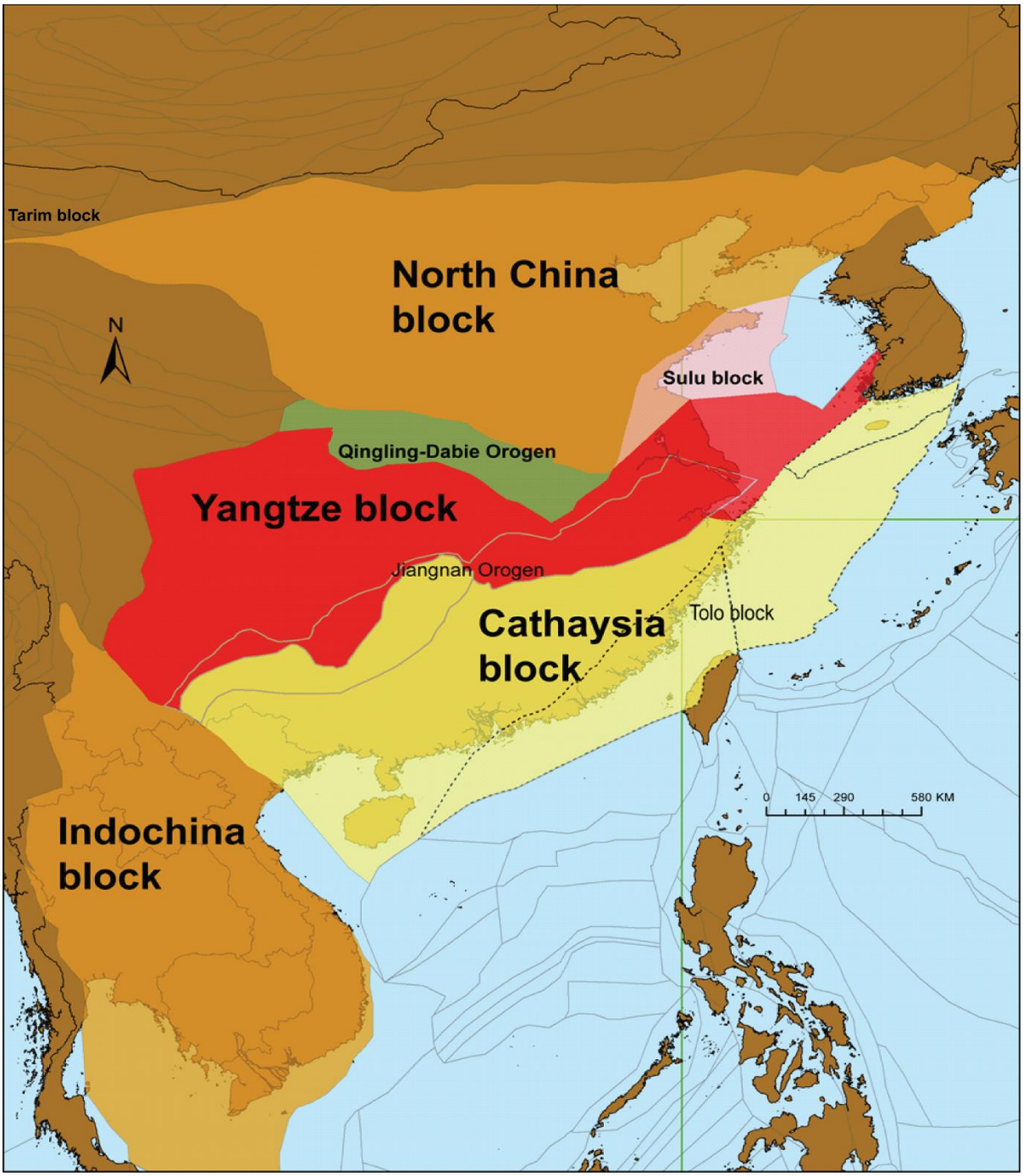

Figure 1.1 The South China block and the blocks that build up the SCB. The study area is coloured separately from adjacent blocks, showing subdivision of the SCB into Yangtze (Yangtze and western part of Jiangnan), Cathaysia (Cathaysia, eastern part of Jiangnan and Tolo), Qingling-Dabie and Sulu components. Boundaries are taken from the PalaeoPlates model (Eglington, personal communication, 2017)

1.2 Previous tectonic interpretations for the South China block

1.2.1 Geological history of the SCB

The SCB's whole tectonic history involves 6 stages:

1. formation of the protolith of the Yangtze block basement around 3.5 Ga with the oldest igneous rocks being ~3.0 Ga (Qiu et al., 2018);
2. formation of the protolith of the Cathaysia block basement around 3.0 Ga with the oldest igneous rocks being ~1.8 Ga (Wang et al., 2015);
3. amalgamation of Yangtze and Cathaysia block;
4. movement of SCB as a unified entity (in this stage, the SCB could collide or break apart from other blocks);
5. the amalgamation of SCB and North China block at around 200 Ma;
6. the relative movement to present day position.

Most published articles focus on only small-scale areas within South China and there are few studies that investigate the broad-scale structure and movement of SCB. This thesis focuses on regional geological patterns of development of the SCB while also considering the influence of adjacent blocks. The possible geochronological history of the SCB, as suggested by data from previous publications is as follows:

1. The Cathaysia block subducted under the southern margin of the Yangtze block starting at around 1000 Ma (Li et al., 2009).
2. Subduction continued until collision of the Yangtze and Cathaysia blocks between 900 and 800 Ma (Li et al., 2009), resulting in uplift of the central part of the SCB to form the Jiangnan Orogen. Formation of juvenile oceanic crust and reworking of the old crust happened during the Jiangnan Orogen.
3. Various igneous activities happened within the SCB signalling intra-craton activities during 800-500 Ma period.
4. During the Paleozoic era, specifically between 400 and 500 Ma, older crust was reworked, possibly with uplift of the Cathaysia block. Sedimentary paleocurrents indicators from the Cathaysia to the Yangtze blocks suggest that the SCB collided with some other continent to produce the uplift (Yao and Li, 2016).

5. At around 200 Ma, a major event occurred at the northern margin of the Yangtze block. Both igneous and sedimentary rock records give evidence for the collision between the SCB and North China plates (Li et al., 2017). A volcanic arc created on the Yangtze block shows that the North China block subducted beneath the SCB. Detrital records reveal metamorphic events in this region, which imply that rocks were exhumed immediately after the metamorphism.

6. Approximately around 160 Ma, the Tolo block collided with the Cathaysia block (Sewell et al., 2016), following which, the Pacific plate subducted beneath Asia, producing igneous activities from ~100 Ma to the present.

7. Igneous records from the Tibet plateau show the last collision of the Eurasian continent with the India plate, leading to tectonic reactivation of some of the pre-existing crustal boundaries and sediment transport across the Indochina and the South China blocks ultimately to the South China Sea (Wang et al., 2014).

1.2.2 Debate on the time of the formation of the South China block

The first vital question is: when did the SCB amalgamate? The Yangtze and Cathaysia blocks are the main discussion objects before the amalgamation of the SCB. The majority of published articles suggest an amalgamation time of the SCB at around 950-800 Ma (Li et al., 2013, 2003; Wang et al., 2008, 2006; Zhou et al., 2009), but there are also other suggestions; for instance Hsü (Hsü et al., 1990) and Wilhem (Wilhem et al., 2012) suggested the amalgamation time of SCB at 500-400 Ma (Li, 2014). This chapter will focus on the variety of suggestions for formation of SCB.

Li's Rodinia model (Li et al., 2008) assumed that the South China block formed earlier than 900 Ma (Figure 1.2), with the Yangtze and Cathaysia blocks colliding between 900 and 1000 Ma, based on orogenic history, basin history, global plate kinematics and paleomagnetism.

A number of other authors have suggested a younger Neoproterozoic age for amalgamation, typically about 850-800 Ma (Chen et al., 2014; Xia et al., 2015; Zhang et al., 2013; Zhang et al., 2015b)

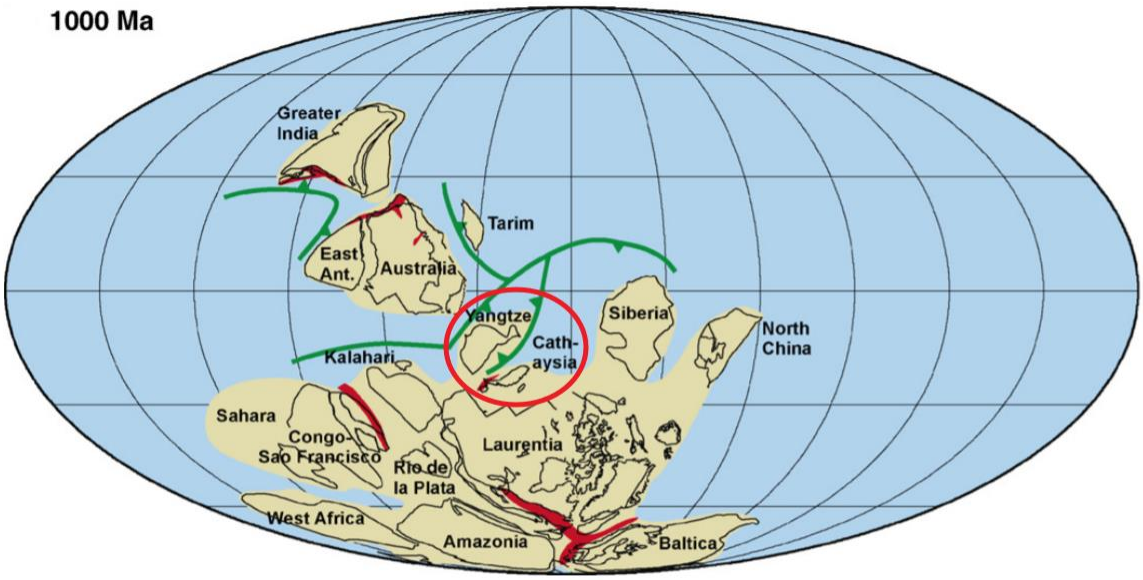

A.

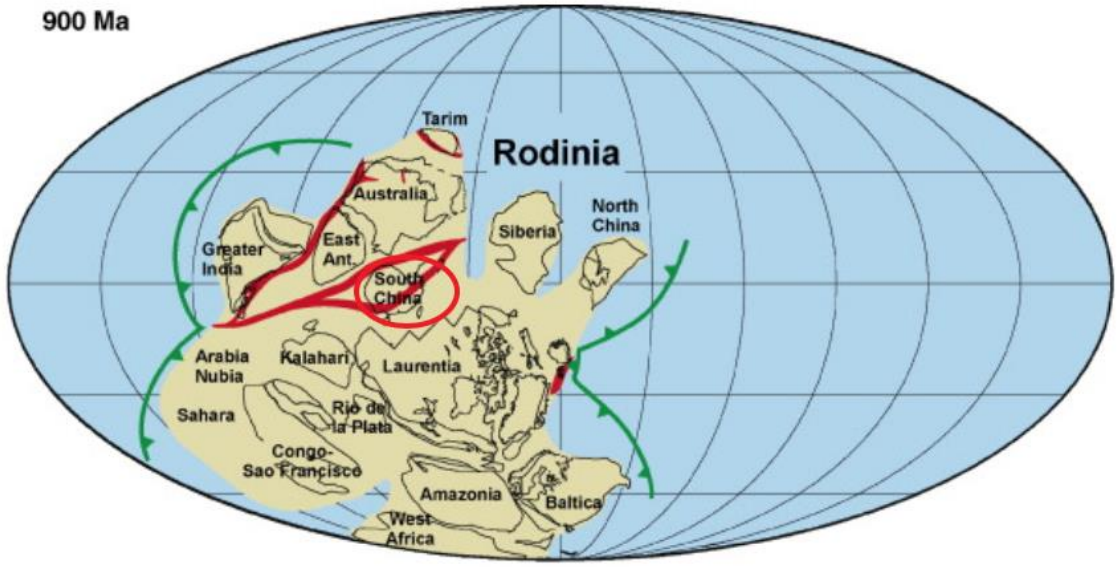

B.

Figure 1.2 Position of the SCB in the Rodinia supercontinent at A.1000 Ma; B. 900 Ma (After Li et al., 2008)

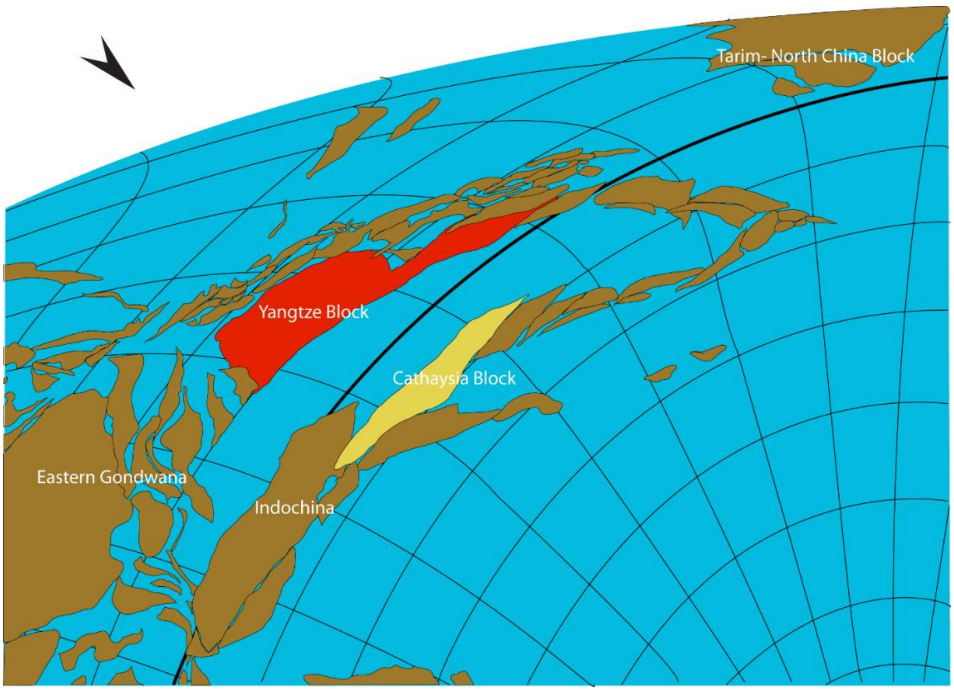

A.

B.

Figure 1.3 A. Relative position of SCB (Yangtze and Cathaysia) in supercontinent at 461 Ma; B. Relative position of SCB in supercontinent at 442 Ma (Modified after Wilhem et al., 2012)

In contrast, Hsü suggested that Yangtze block was still separated from the Gondwana supercontinent at Devonian period (Hsü et al., 1990). This suggestion is applied by a later study (Wilhem et al., 2012) to create a plate reconstruction model which accepted that collision between the Yangtze and Cathaysia blocks occurred in the early Silurian. Figure 1.3 shows the position of the SCB in the Gondwana supercontinent, as suggested by Wilhem's research (Wilhem et al., 2012). In this model, the Yangtze block and the Cathaysia block are separate at 461 Ma and finally collide at about 442 Ma. Wilhem's model also includes the relative positions of many other Asian and global blocks, some of which may influence interpretations for the regional history of the geology of the SCB.

1.2.3 Process leading to amalgamation of the Yangtze and Cathaysia blocks

In addition to the different views on the amalgamation age of the SCB, the processes leading to joining of the Yangtze and Cathaysia blocks are also debated. Previous studies have suggested several possible processes, the most distinct being:

1. Zhang suggested that formation of the SCB resulted from subduction of the Cathaysia block underneath the Yangtze block (Zhang et al., 2013). From igneous zircon dating results of about 800 Ma, and geochemistry and rare earth element fingerprinting, Zhang concluded that the Yangtze and Cathaysia blocks first joined together in the south west (Figure 1.4), with subduction starting before about 1000 Ma. Further east, subduction continued with the Yangtze block as the upper plate. As subduction progressed, the ocean between the two blocks progressively closed towards the north east. Arc type settings on the Yangtze block were converted into an orogenic belt. Figure 1.4 shows the process suggested by Zhang et al (2013). Data from Zhang's samples are compiled in this research to better show the process of the formation of the SCB.

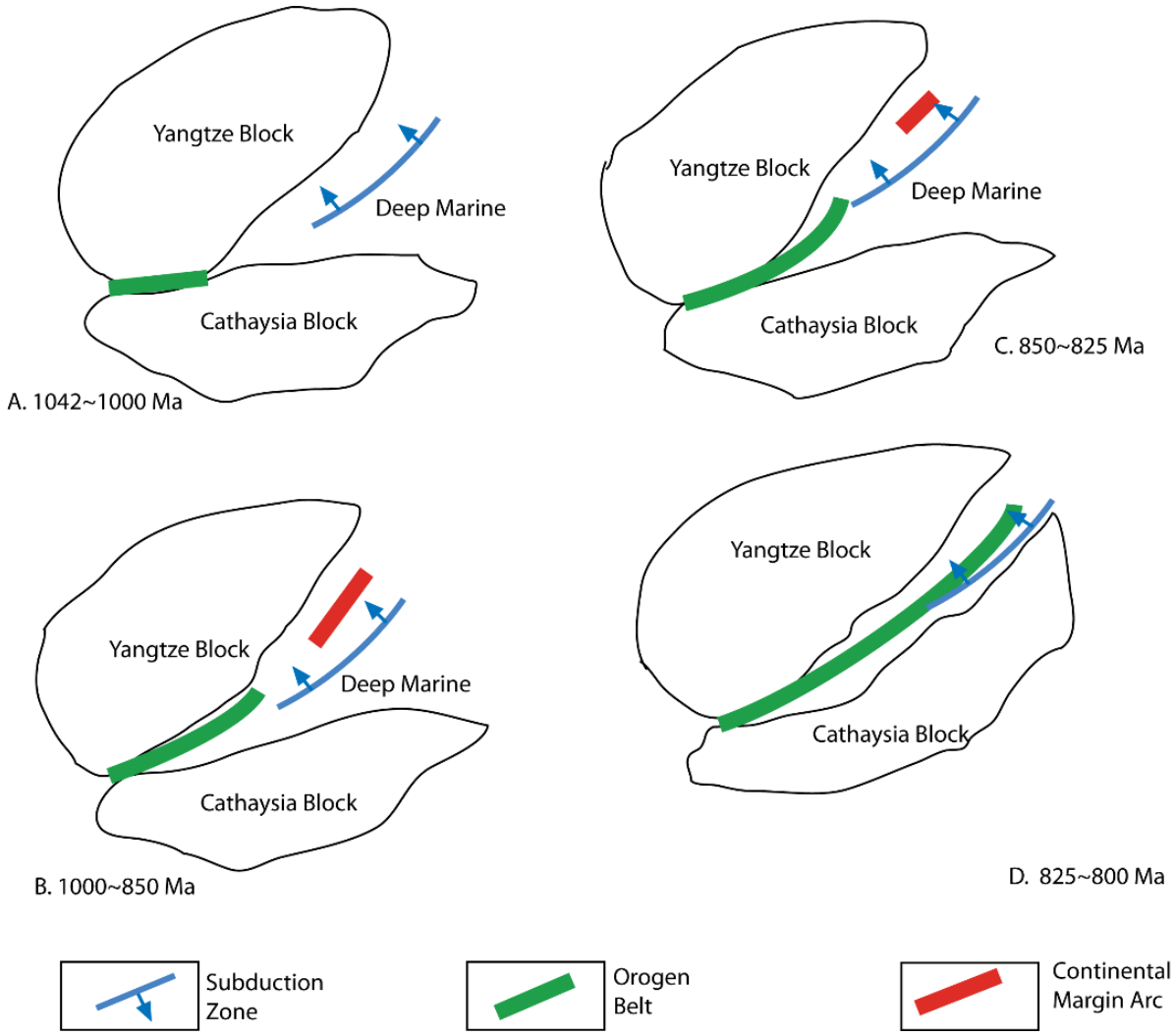

Figure 1.4 A possible process of how the SCB could have formed (after Zhang et al., 2013). Subduction occurred along the eastern margin of the Yangtze block from ~1000 Ma while the Yangtze and Cathaysia blocks merged between 900 and 800 Ma.

2. Chen et al (2014) disagreed with the hinged closure of the ocean between Cathaysia and Yangtze (Zhang et al., 2013), preferring a more orthogonal subduction. Chen's igneous rock samples had Th and Nb anomalies, which they interpreted to indicate subduction in the southwestern part of the Jiangnan Orogen (Chen et al., 2014). U-Pb zircon dating data from Chen's samples dates their crystallization at ~830 Ma, suggesting that the collision between Cathaysia and Yangtze block is around that age.

3. Xia et al (2015) proposed an amalgamation process for the SCB which is very different from Zhang's model (Zhang et al., 2013), with Yangtze as the lower plate and Cathaysia on the upper plate. Xia's samples were from the eastern part of Jiangnan Orogen in the Cathaysia block. From geochemistry data of their rocks, Xia drew the conclusion that the Cathaysia block was

subducted from 1000 to 825 Ma until the ocean disappeared (Xia et al., 2015). Figure 1.5 is the schematic diagram illustrating the process of subduction and collision of the Yangtze and Cathaysia blocks. Figure 1.5 also shows several types of igneous rock association generated from mantle and crustal melting as part of this process.

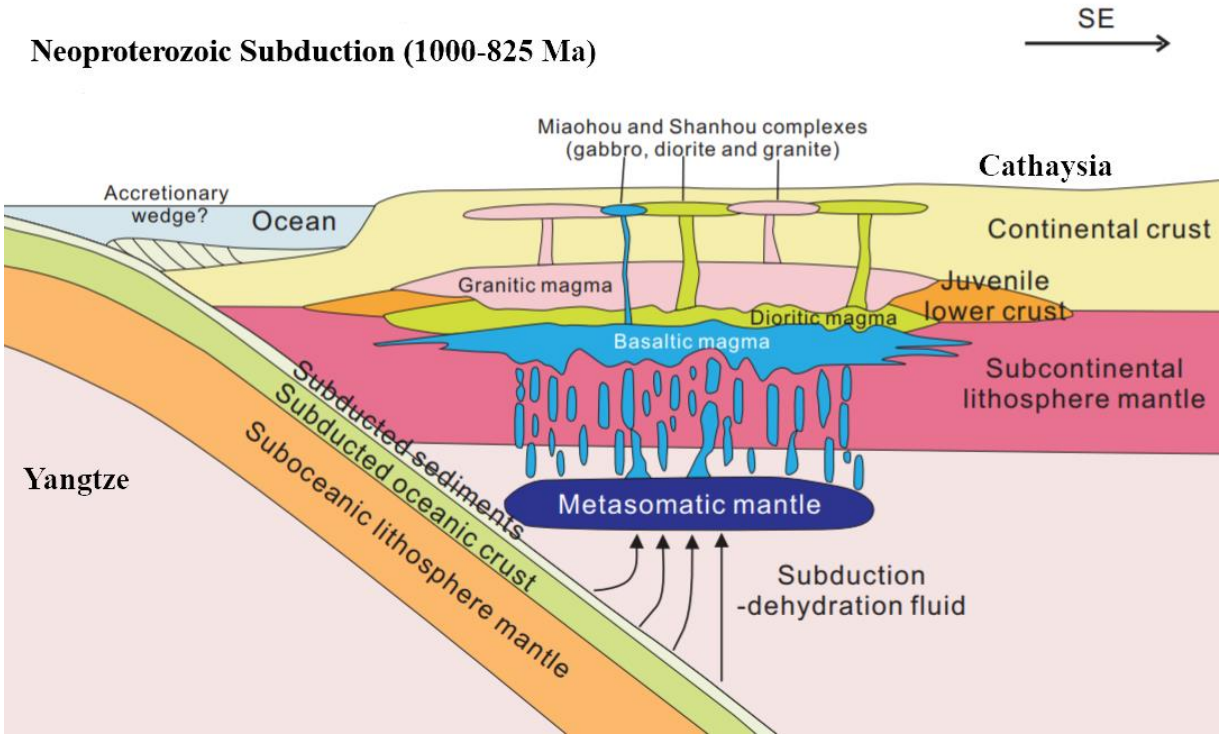

Figure 1.5 Collision process of Yangtze and Cathaysia block (Xia et al., 2015)

4. It is not only the igneous rocks which reveal the tectonic history of the SCB. Sedimentary rocks also show significant details. Zhang et al (2015b) studied a group of conglomerates and agglomerates in the Jiangnan Orogen which reveal possible processes of SCB's formation. Zhang drew their conclusion from chemical and isotope chemical data of volcanic gravel in the sedimentary rocks (Zhang et al., 2015b), inferring back-arc settings on the eastern margin of the Yangtze block. Figure 1.6 is the schematic of Zhang's model, in which subduction at the central part of the Jiangnan Orogen began at around 900 Ma with the Yangtze block as the lower plate that is subducted beneath the Cathaysia block. However, at around 860 Ma, the upper plate and lower plate are swapped, the process ending up forming a back-arc basin on the eastern margin of the Yangtze block. Around 830 Ma the two blocks finally collided and formed a united SCB.

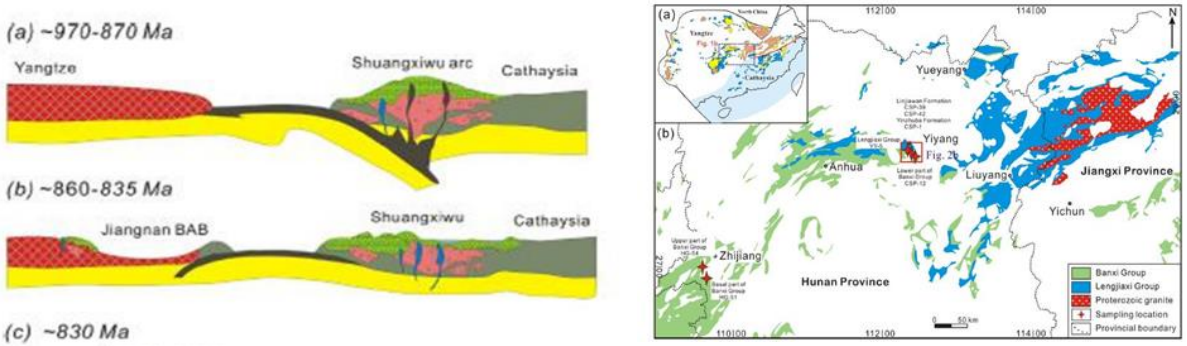

Figure 1.6 Left: the time interval schematic of SCB's formation.
Right: The position of Zhang's studied area Zhang et al., 2015b

Each of these different models for amalgamation of the SCB is based on data from very limited areas. In this thesis, however, I collate data from across the entire SCB to identify patterns in both space and time which should better constrain the origin of the block. The combined data also provide information for a global tectonic reconstruction model.

1.2.4 Post-amalgamation tectonic history of the SCB

After the amalgamation of the SCB, there were continued interactions with many other blocks until the present-day configuration was created. This thesis compares the data for the SCB during the Cambrian to Ordovician relative to the Neoproterozoic. The purpose is to eventually show which age interval and what processes are the most reasonable for formation of the SCB.

Yao's recent study on the sedimentary rocks of South China reflects the tectonic development of the SCB from 500 Ma to 400 Ma (Yao and Li, 2016). Figure 1.7 shows paleocurrent directions in the model of Yao. Additionally, Figure 1.7 also shows Yao's suggestion for how the SCB changed position relative to the Gondwana supercontinent during this time interval. From Figure 1.7 one can see that at 450 Ma the South China block might be linked to the northern part of the India block as a result of post-Neoproterozoic collision. The sedimentary data of Yao's research is included in this study to further understand the position of the SCB and geodynamic activity during the Paleozoic.

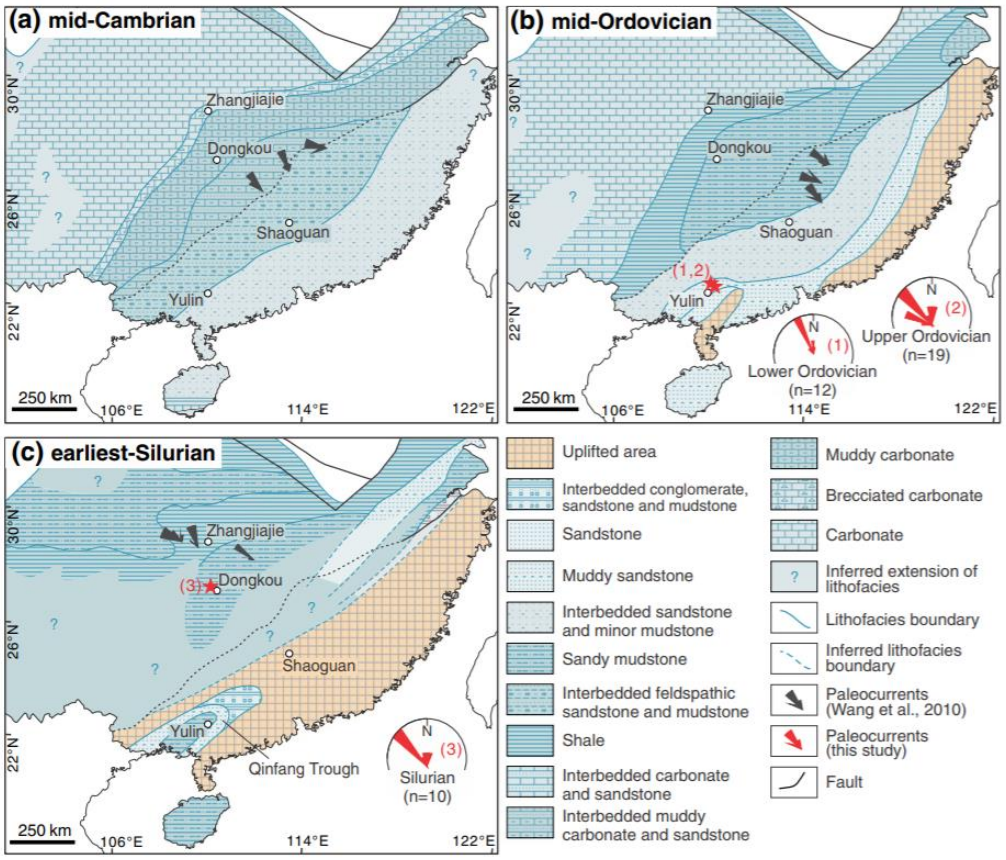

A.

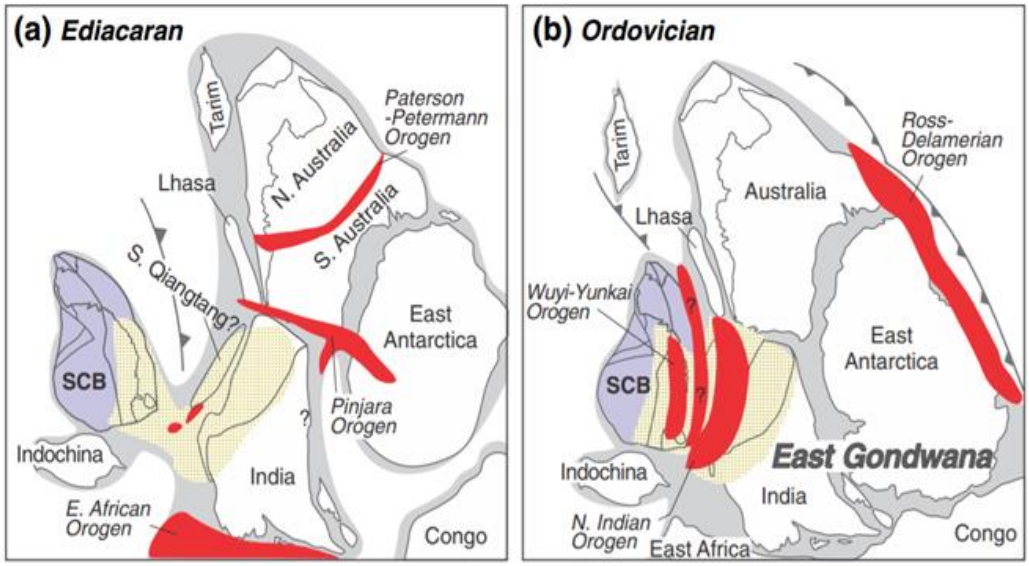

B.

Figure 1.7 A. Paleogeographic maps of the South China block showing the evolution of the Nanhua foreland basin and the Wuyi–Yunkai Orogen during: (a) mid-Cambrian, (b) mid-Ordovician, and (c) earliest-Silurian periods; B. SCB's position at ~450 Ma and SCB's possible link with the east Gondwana supercontinent (North India). (After Yao and Li, 2016)

After the possible 450 Ma collision of the SCB with Gondwana, collision of the SCB and the NCB happened during the Jurassic period (Enkin et al., 1992) according to the subduction model suggested by Li (Li et al., 2017). For this thesis, data for rock samples from near the boundary of the SCB and NCB were compiled to further assess evidence for this collision.

1.3 Structure of thesis chapters

Chapter 2 describes the methods used to compile, process and view the regional data. Chapter 3 reviews and assesses relevant igneous data, Chapter 4 considers the metamorphic rock data and Chapter 5 considers detrital zircon information. Where appropriate, these chapters also summarize interpretations which can be made from the individual lines of evidence and techniques considered in each chapter. **Error! Reference source not found.** considers situations where multiple lines of evidence support particular interpretations and links these interpretations to the regional geodynamic history and plate tectonic setting of the SCB.

CHAPTER 2
METHODOLOGY

2.1 Introduction of software, databases and tools used in this study

As mentioned in Chapter 1, most previous studies of the South China block are through studying samples from individual small areas. However, this study uses a compilation of many published data across the entire SCB to achieve an overview at the scale of the continental block. All raw data and their original references compiled from published records were stored in the DateView and StratDB online database (http://sil.usask.ca/databases.htm). References to all the sources of data used in diagrams and graphs presented in this thesis are therefore not provided, only those relating to topics where appropriate.

Specific aspect for which data were compiled for this thesis were: geochronology, geochemistry, isotope geochemistry and sedimentology; bringing these data together to infer the most likely scenario for the development history of the SCB.

To collect data and manage them, proper databases should be utilized. Access is Microsoft office database software which also provides a way to create a GIS geodatabase. Apart from Access databases, Firebird is an open access data storage system also used in this study; it is used to store large quantities of lithochemistry data for the SCB. Other software used in this thesis include: ArcGIS for sample location information and for creating maps (https://www.arcgis.com/home/index.html); GPlates for reconstructions showing changing location in time and space (https://www.gplates.org/); ioGAS for rock geochemistry composition analysis (https://reflexnow.com/iogas/); FitPDF (Eglington, 2018a) for drawing probability curves illustrating geochronology and for detrital zircon diagrams of deposition time vs crystallization time; DVRawData (Eglington, 2018b) for compiling original spreadsheet data into a temporary database before uploading to the DateView database. Geodate (Eglington, 2018c) was used for graphing of individual detrital zircon grain populations and for calculation model ages, initial ratios and epsilon values.

2.2 Data collection for the thesis

Geochronology data of igneous and metamorphic rocks are an important dataset for this thesis. Cooling, crystallization, metamorphic, crustal formation and crustal residence ages can be derived from different isotopic dating systems of a variety of minerals (Dickin, 2005). Figure 2.1 shows the blocking temperatures of several isotope systems and minerals. One can see that in Figure 2.1, zircon (U-Pb),

monazite (U-Pb), titanite (U-Pb) have high blocking temperatures, indicating that the crystallization ages of zircon or monazite can represent the magmatic age of an igneous rock. Zircon and monazite in metamorphic rocks preserve ages close to peak metamorphism instead of the cooling age (Rollinson, 2014). Most of the geochronology data collected in the DateView database for the SCB are U-Pb zircon and monazite data plus whole rock Sm-Nd and zircon Lu-Hf data. For igneous rocks these represent the age when the rocks were formed; for sedimentary rocks they may represent formation ages for multiple protoliths, which can sometimes be traced back to their source rocks in order to understand where the sediment comes from. For metamorphic rocks, the ages represent major individual metamorphic events in the studied area. This thesis concentrated on compiling data for South China but also considered data for some adjacent areas which helped understand the evolution of the SCB.

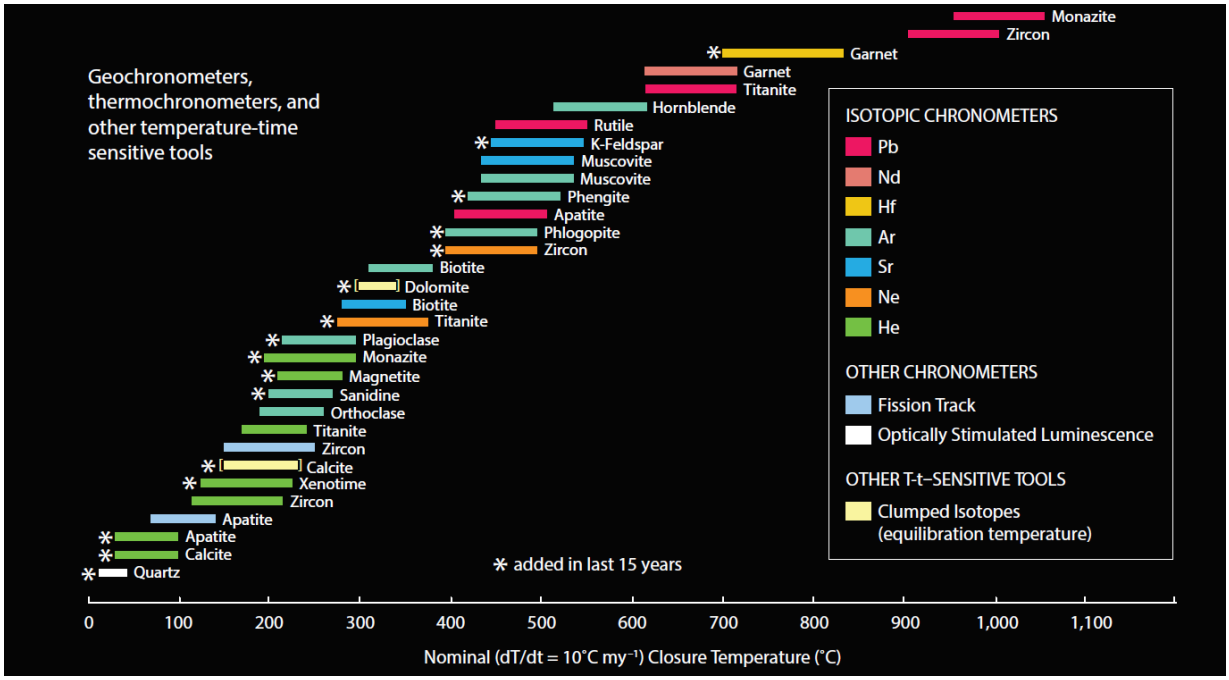

Figure 2.1 Mineral isotope systems and their blocking temperatures (Huntington and Klepeis, 2018)

2.3 Method of calculation for age probability curves

Age distribution for data compilations and for detrital zircons may be shown as histograms or probability distribution graphs (Eglington, 2018a; Ludwig, 2012; Vermeesch, 2012). Most approaches to the calculation of probability distributions use Gaussian 'AND' summation with the width of individual peaks determined either by the analytical precision (Eglington, 2018c; Ludwig, 2012) or by some averaged optimised bin width, as in kernel density estimates (Vermeesch, 2012). It is also possible to calculate either

Gaussian ‘AND’ or Gaussian ‘OR’ probabilities, as shown by Eglington et al., (2018). Figure 2.2 illustrates the differences between Gaussian ‘AND’ and Gaussian ‘OR’ approaches, based on four hypothetical analyses. Where analyses overlap substantially, the ‘AND’ approach produces higher and higher summed probability peaks whereas the ‘OR’ approach provides a maximum determined by the greatest probability from on individual analysis. These different approaches produce very different distributions. In cases where there are many grains of equivalent age in a specific sample, the ‘AND’ calculation produces a high probability peak whereas the ‘OR’ version does not. An example from igneous dating demonstrates the limitations of the ‘AND’ methodology: imagine that the age of a single intrusion is analysed by multiple techniques and researchers, all resulting in equivalent ages. If all data are compiled into a probability distribution, then the ‘AND’ approach will over-emphasise the influence of these multiple analyses. In contrast, the ‘OR’ approach will reflect a probability related to only the most precise analysis. For detrital zircon investigations, one might ask: is a single grain analysis representative of its provenance age source just as important as multiple grains from another source which just happen to have been transported into a basin more efficiently? In this sense, the ‘OR’ calculation is more robust than the ‘AND’ version since one need only one precise analysis to fill a gap in an ‘OR’ distribution. In general, ‘AND’ and ‘OR’ distributions for large datasets look very different since the ‘AND’ approach emphasises multiple similar analyses in a sample (high probability peaks get emphasised) whereas the ‘OR’ approach emphasises intervals with few or no overlapping analytical uncertainties.

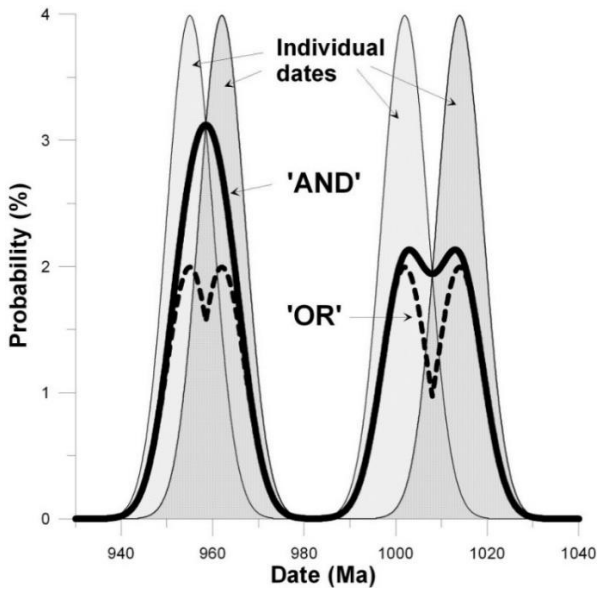

Figure 2.2 Gaussian ‘AND’ (solid thick line) and ‘OR’ (dashed thick line) representation of a simple test dataset comprising four analyses (solid thin lines) (Eglington et al., in press). Note the difference in peak height between the two approaches.

2.4 Comparison of data from the blocks assembled to form the SCB

As outlined in Chapter 1, the SCB is made up of four blocks, among which the most important two blocks are the Yangtze and Cathaysia blocks. Most previous studies have applied this subdivision without assessing the distinction between the Yangtze and Cathaysia blocks. Igneous rock U-Pb data show the age difference of Yangtze and Cathaysia blocks: old basement rocks with ages of about 3.0 Ga (Qiu et al., 2018) are found in the Yangtze block, but the Cathaysia block's oldest rocks formed in the late Paleoproterozoic around 1.9~1.8 Ga (Li et al., 2014). Maximum T_{2DM} protolith ages for the Yangtze block are ~3.5 Ga (Qiu et al., 2018) while those for the Cathaysia block are ~3.0 Ga (Wang et al., 2015). To emphasise the basement geochronology data and de-emphasise the younger age groups in the Yangtze block, the igneous probability curves in Figure 2.3 were calculated by Gaussian 'OR' summation. T_{DM} curves illustrate the possible protolith ages of the lithosphere in these blocks. The igneous zircon probability curves for the Yangtze and Cathaysia blocks before 1000 Ma are different from each other and have no significant overlap in age distribution. Thus, I infer that these two blocks were separated from each other prior to ~1000 Ma. Furthermore, the isotope geochemistry data of igneous rock samples in the two blocks are different. The probability of T_{DM} ages in the Yangtze block shows one significant peak around 1000 Ma and a less significant peak around 2800 Ma. In Cathaysia, the major T_{DM} peak is slightly older than for Yangtze. Apart from that, other T_{DM} peaks in the Cathaysia block curve do not match the 2800 Ma Yangtze peak. Cathaysia also shows several peaks at 1500 Ma to 2600 Ma. Figure 2.4 shows initial Sm-Nd epsilon values for igneous rocks. Together with Figure 2.3, the data suggested that the Yangtze and Cathaysia blocks formed at different times but they each contain igneous rocks that originate from reworking of very old protolith, specifically 3.5 Ga and 3.0 Ga.

Some publications distinguish an eastern section of the Cathaysia block (Liu et al., 2012 and reference therein), named the Tolo block by Sewell et al (Sewell et al., 2016). Sewell et al suggested that the Tolo block was joined to the rest of Cathaysia at around 160 Ma. However, from Figure 2.4, one can see that the epsilon Nd data from the Tolo block are not very different from the Cathaysia block. There is no indication of extensive approximately 160 Ma magmatism near the margins of the Tolo and Cathaysia blocks. It is therefore possible that the Tolo block is just a section of Cathaysia which was rifted off before 180 Ma and then rejoined with the main Cathaysia block at ~160 Ma.

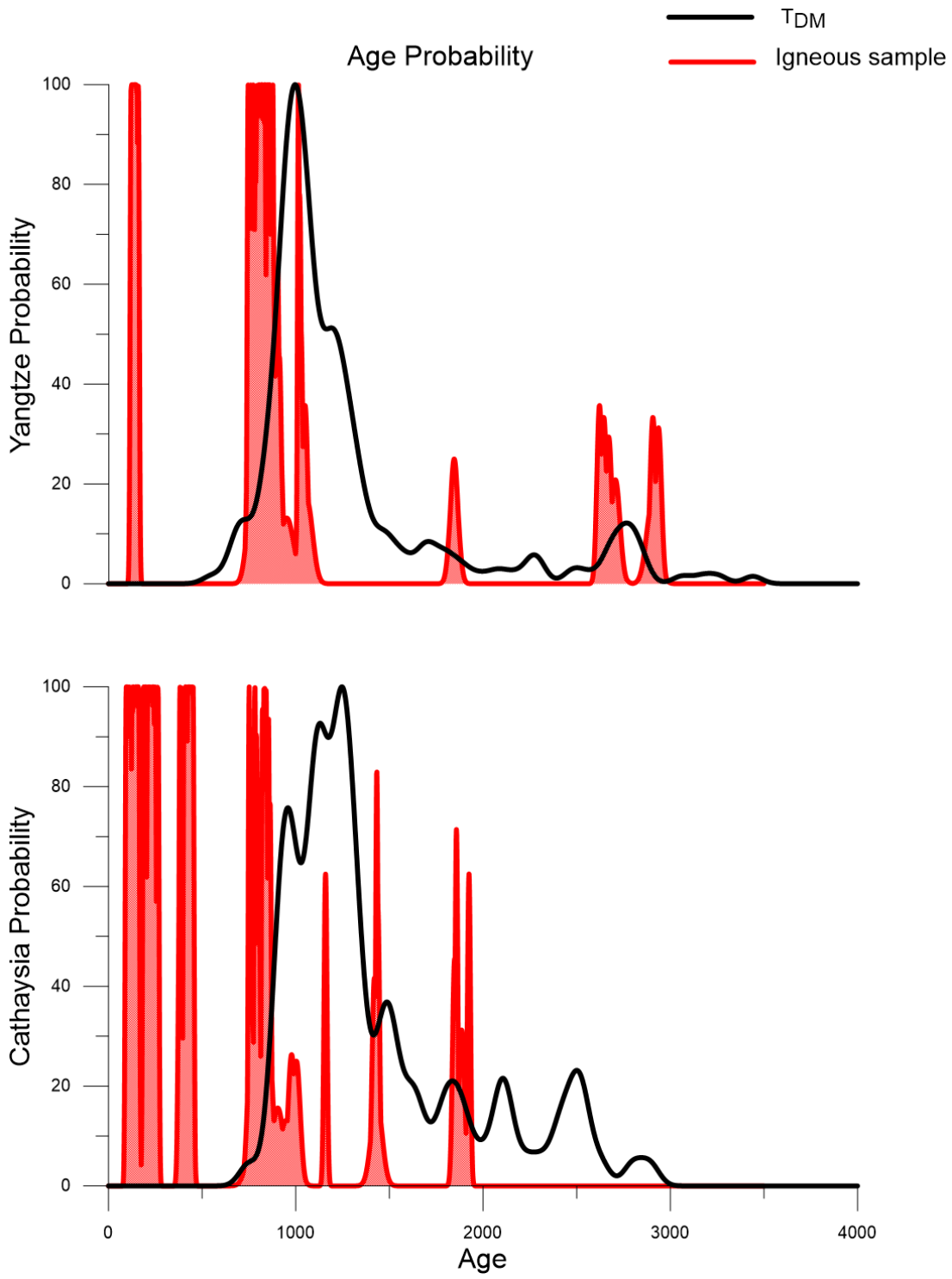

Figure 2.3 Probability density curves of Hf isotope T_{DM} model and igneous rock sample crystallization ages from the DateView database for the Cathaysia and Yangtze blocks. Crystallization age curves (red) calculated using Gaussian 'OR' method and T_{DM} curves (black) calculated using Gaussian 'AND'. Number of samples: Hf T_{DM} age: Yangtze 241, Cathaysia 118; Number of igneous U-Pb samples: Yangtze 310, Cathaysia 248.

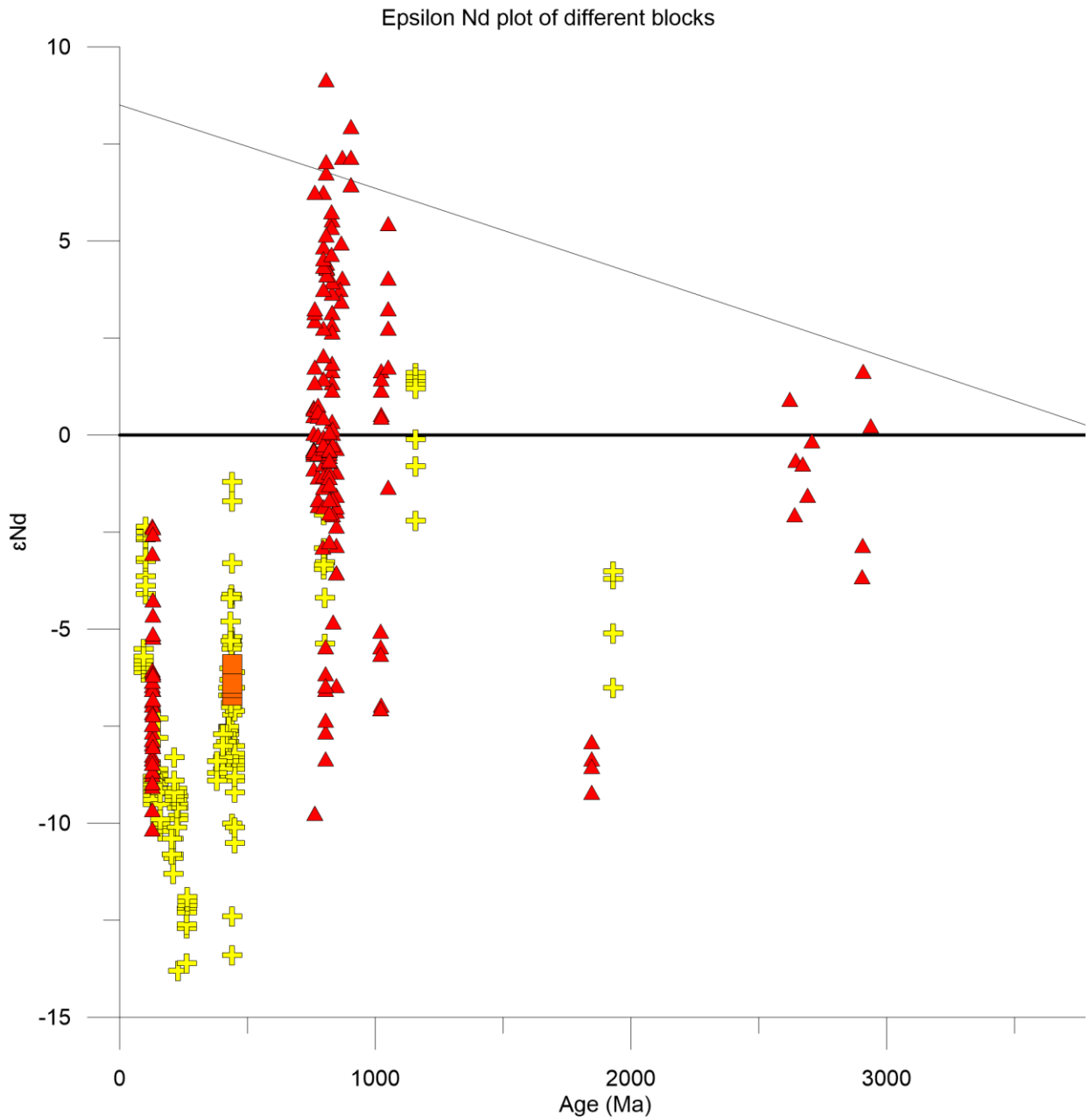

Figure 2.4 Epsilon Nd compositions of igneous rocks from the Cathaysia, Yangtze and Tolo blocks. Red-Yangtze samples; Yellow-Cathaysia samples (except Tolo); Orange-Tolo samples.

2.5 Igneous rocks

2.5.1 Geochronology

Zircon U-Pb data from igneous rocks are of vital importance for this study. The interpreted U-Pb zircon ages from published articles were compiled to represent the formation age of the rocks. A total of 729 igneous rock samples are included for this study and their locations are shown in Figure 2.5. Where available, coordinate information was directly compiled from published papers but, some published papers didn't provide numeric sample location information. Samples without location coordinates were approximated by the available location on the maps presented in the publications or by the locations of geochronology samples in nearby areas. Since this thesis is focused on the scale of the whole SCB, using approximate locations of the regional study case samples will not influence interpretations very much.

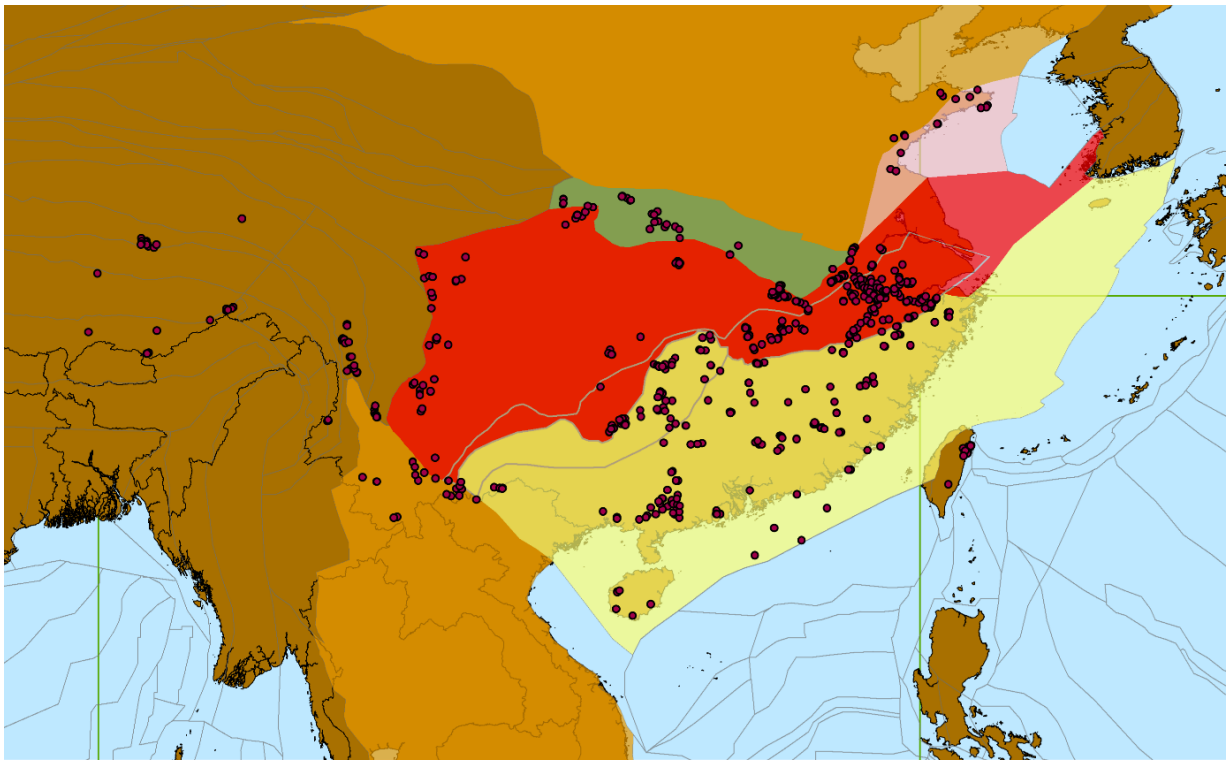

Figure 2.5 Locations of igneous rock samples compiled in the DateView database

2.5.2 Isotope geochemistry

In addition to the magmatic ages of igneous rocks, Sm-Nd and Lu-Hf isotope data were compiled and have been used to better understand protolith age and composition. Lu-Hf data were given in two forms in published articles, either whole-rock values or individual zircon grain/spot values. For Lu-Hf isotope whole-rock data, compilation of the data was simply capturing the value of each sample. However, for the samples with multiple zircon grain analyses, 'raw' individual analyses for each zircon grain were compiled and average values were entered for the samples in the 'summary' section of the DateView database.

Lu-Hf data were compiled for 338 samples, 25 with whole rock average values and 313 with zircon grain data. Location for these samples are shown in Figure 2.6A. Sm-Nd data were compiled for 393 igneous rocks and their locations are shown in Figure 2.6B. There are 88 igneous rock samples with both Lu-Hf and Sm-Nd data.

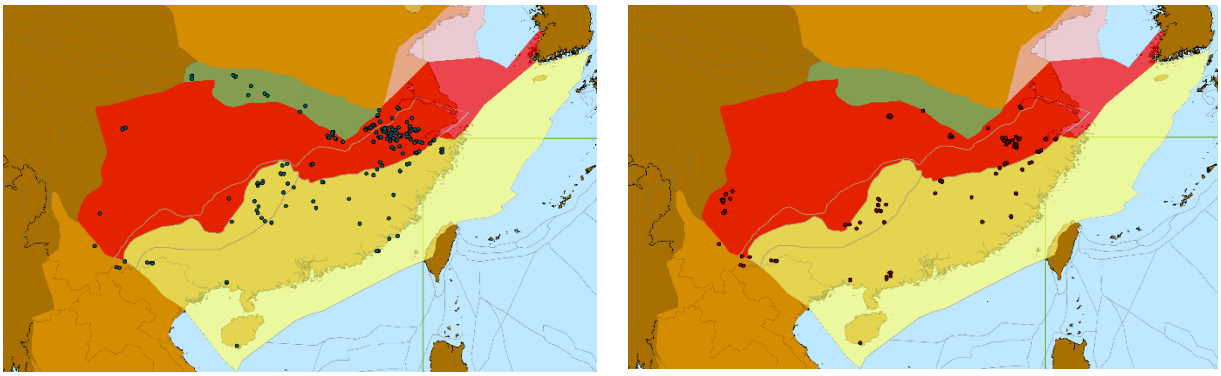

A. B.

Figure 2.6 A. Location of Lu-Hf igneous rock data of this study; B. Location of Sm-Nd igneous rock data of this study.

Depleted mantle model ages and epsilon values were calculated assuming the following values and formulae:

^{176}Lu decays to ^{176}Hf by beta decay with a half-life of 37.12 Ga and decay constant of $(1.867\pm0.008)*10^{-11}$ (Vervoort, 2014). Initial ratios were calculated by the following formula where $(^{176}Hf/^{177}Hf)_0$ and $(^{176}Lu/^{177}Hf)_0$ represent present day value of the sample, the t value in all formulae of this section represent the U-Pb dating age result:

$$(^{176}Hf/^{177}Hf)_{\text{initial ratio}} = (^{176}Hf/^{177}Hf)_{0} - (^{176}Lu/^{177}Hf)_{0} \times (e^{\lambda t}-1)$$

Epsilon Hf value at the crystallization age of samples were calculated with the following formula (Vervoort, 2014):

$$\varepsilon Hf(t) = (((^{176}Hf/^{177}Hf)_{\text{initial sample}} - (^{176}Hf/^{177}Hf)_{\text{initial CHUR}}) / (^{176}Hf/^{177}Hf)_{\text{initial CHUR}}) \times 10000$$

Present day CHUR values for Lu-Hf isotope calculations are from Bouvier (Bouvier et al., 2008): $(^{176}Lu/^{177}Hf)_{0\ \text{CHUR}} = 0.0336$ and $(^{176}Hf/^{177}Hf)_{0\ \text{CHUR}} = 0.282785$.

Depleted mantle model age(T_{DM}) for Hf isotopes is the calculated age representing the assumed seperation time of the protolith from depleted mantle (Vervoort, 2014). Present day depleted mantle values for Lu-Hf isotope calculations are from Griffin (Griffin et al., 2000): $(^{176}Lu/^{177}Hf)_{0\ DM} = 0.0384$ and $(^{176}Hf/^{177}Hf)_{0\ DM} = 0.28325$. The crustal protolith two stage depleted mantle age (T_{2DM}) is further based on the assumption that the source rock from which the zircons crystallize has a very different $^{176}Lu/^{177}Hf$ ratio to the zircons themselves (Champion and Huston, 2016), therefore the protolith evolution curve prior to zircon crystallization is different to the one after crystallization. In this thesis, a present day average crustal value $^{176}Lu/^{177}Hf$, as suggested by Griffin (Griffin et al., 2002): $(^{176}Lu/^{177}Hf)_{0\ \text{CRUST}} = 0.015$ has been used. The calculation formulae of T_{DM} and T_{2DM} are as follow:

$$T_{DM} = (1/\lambda) \times \ln(((^{176}Hf/^{177}Hf)_{0\ \text{Sample}} - (^{176}Hf/^{177}Hf)_{0\ DM}) / ((^{176}Lu/^{177}Hf)_{0\ \text{Sample}} - (^{176}Lu/^{177}Hf)_{0\ DM}) + 1)$$

$$T_{2DM} = (1/\lambda) \times \ln(((^{176}Hf/^{177}Hf)_{0\ \text{CRUST}} - (^{176}Hf/^{177}Hf)_{0\ DM}) / ((^{176}Lu/^{177}Hf)_{0\ \text{CRUST}} - (^{176}Lu/^{177}Hf)_{0\ DM}) + 1)$$

$$(^{176}Hf/^{177}Hf)_{0\ \text{CRUST}} = (^{176}Hf/^{177}Hf)_{\text{initial sample}} + (^{176}Lu/^{177}Hf)_{0\ \text{CRUST}} \times (e^{\lambda t}-1)$$

In cases where both U-Pb and Lu-Hf analysis are available for spots in zircon, the U-Pb data are first assessed for concordance and igneous age relevance. Only those Lu-Hf analysis spots which coincide with concordant ages for igneous crystallization were used for calculating average epsilon, T_{DM} and T_{2DM} values.

Figure 2.7 shows the difference between T_{DM} and T_{2DM} for an example dataset. The dashed curves show projected zircon evolution (top) and calculated T_{DM} ages while the solid lines illustrate protolith evolution and T_{2DM} values. Each point represents a zircon grain from the example rock sample. The dashed line array is calculated with only the sample's Lu/Hf ratio. The bold lines are calculated using both sample Lu/Hf values and the average crust Lu/Hf value.

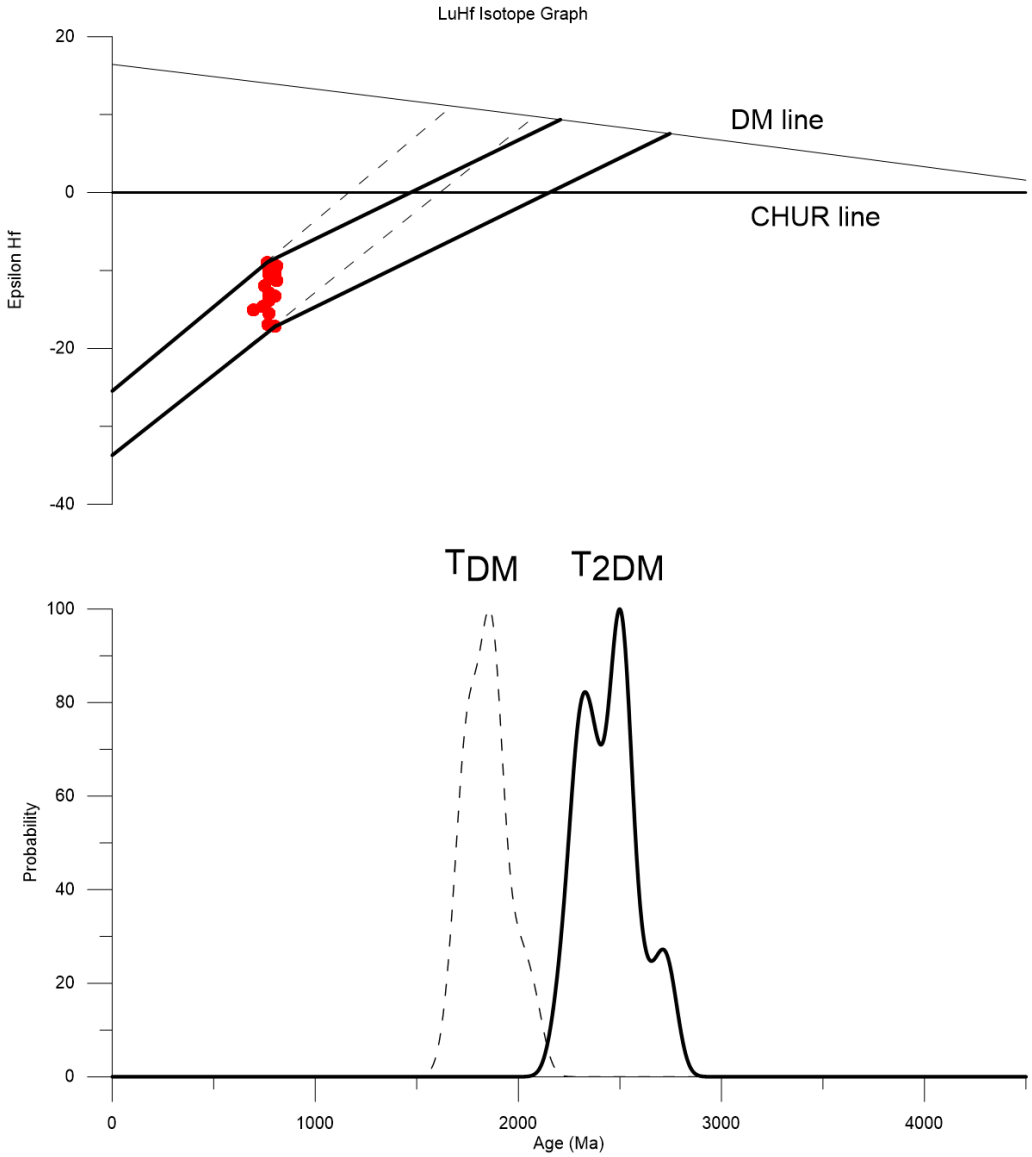

Figure 2.7 εHf(t) vs Age graph of igneous rock zircon sample12HZ02-1 (Hu et al., 2016). T_{DM} and T_{2DM} age peak are calculated by Gaussian 'AND' with age uncertainty of 25 Ma and highest probability normalised to 100 percent.

Sm-Nd data were compiled for whole rock analysis of igneous samples. Initial ratio, epsilon, T_{DM} and T_{2DM} values were calculated using similar formulae to those shown for Lu-Hf earlier. Values used for calculations are:

Decay constant for $^{147}Sm=6.54*10^{-12}$

Present day CHUR values for Sm-Nd isotope calculations are from Bouvier (Bouvier et al., 2008): $(^{147}Sm/^{144}Nd)_{0\,CHUR}= 0.1967$ and $(^{143}Nd/^{144}Nd)_{0\,CHUR}= 0.51264$.

Present day values of depleted mantle for Sm-Nd isotope calculations are from DePaolo (DePaolo, 1981): $(^{147}Sm/^{144}Nd)_{0\,DM}$= 0.2136 and $(^{143}Nd/^{144}Nd)_{0\,DM}$= 0.513074.

Present day average crustal $^{147}Sm/^{144}Nd$ value is taken as 0.11 (Champion and Huston, 2016).

Since most of the samples have either Nd or Hf isotope data, but not both, it is convenient to adopt a method to derive equivalent values for one of the systems to visualise the results with common symbology. Vervoort et al (Vervoort et al., 2011) showed that terrestrial samples have correlated Nd and Hf isotope compositions and that the epsilon values in the two isotope systems are reasonably related according to the following formula:

$$\varepsilon Nd = (\varepsilon Hf - 1.21)/1.55$$ (Modified after Vervoort et al., 2011)

In this thesis 88 igneous rocks have data from both Lu-Hf and Sm-Nd systems, therefore these samples were graphed to compare the correlation with Vervoort's suggestion (Vervoort et al., 2011). From Figure 2.8 we can see that igneous samples in this study shows similar pattern to the terrestrial line suggested by Vervoot (Vervoort et al., 2011).Thus, I adapt the equation for all the Lu-Hf data which do not have Sm-Nd isotope values. This allows one to represent both Lu-Hf and Sm-Nd data on maps with a single symbology colour scale although different symbols were used to distinguish values derived from the different isotope systems.

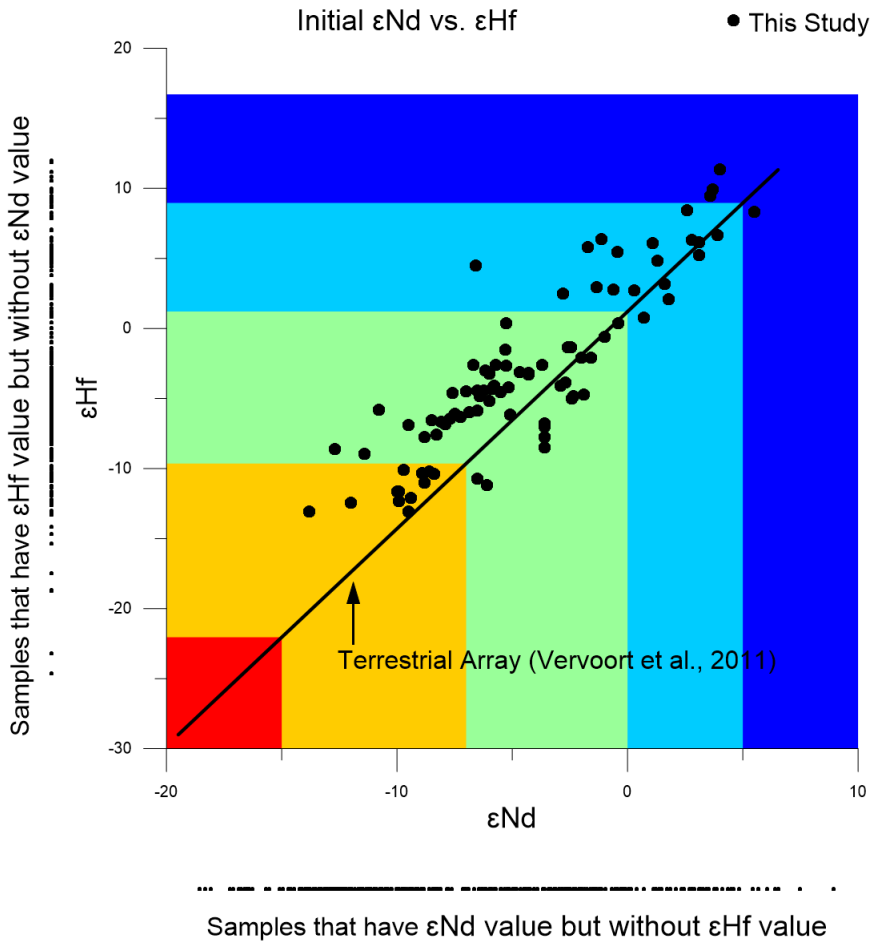

Figure 2.8 εHf vs εNd diagram comparison with Vervoort's (Vervoort et al., 2011) study on terrestrial samples. Plotted data are from 88 igneous rock samples, from 18 published articles, with both Sm-Nd and Lu-Hf isotope data. Reference information is available in the DateView database. εNd value colour range is the same as used in various location maps, e.g. Figure 3.3.

2.5.3 Lithochemistry

Many published articles also provide rock chemistry composition data, which can be useful to either assess what type of tectonic setting the rock formed in (Pearce et al., 1984; Pearce, 2014, 2008) or to assess geological processes related to development of the samples (fractionation, partial melting, mineral species, etc.). Lithochemical data were compiled for 1018 igneous samples, locations for which are shown in Figure 2.9.

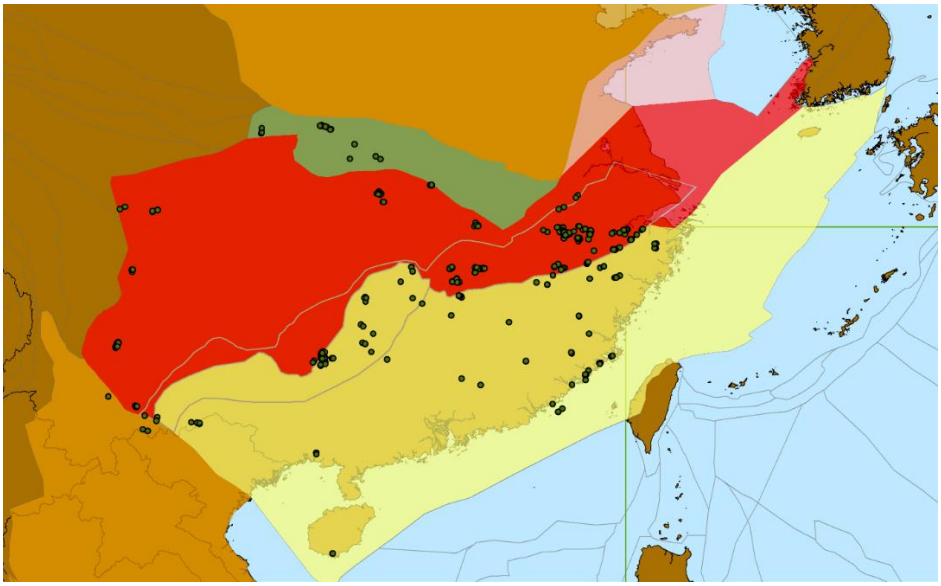

Figure 2.9 The location of the lithochemical data compiled in this study.

Some lithochemical elements, often referred to as mobile elements, are affected by weathering and alteration. All sample data were therefore classified into rock types using immobile element plots (Pearce, 2014). Figure 2.10 provides an example from the Troodos and Semail ophiolites for how immobile elements (like Zr, Ti, Nb and Y) can better identify primary rock compositions even when mobile elements (like Na_2O, K_2O and SiO_2) are altered (Pearce, 2014). Figure 2.10A shows lots of scatter and very variable rock classification, ranging from ultramafic to felsic compositions even though all samples are from a basaltic stratigraphy. In Figure 2.10B all the samples plot in either basaltic andesite or basalt areas, as expected (Pearce, 2014). Thus Figure 2.10B was used in this study as the diagram to classify the rock samples and to distinguish between mafic and felsic lithologies. This distinction is needed before one can assess tectonic settings using many of the published tectonic discrimination diagrams. In this study all the igneous rock samples were separated as either felsic rocks or mafic rocks regardless of whether it is intrusive or extrusive. For samples generated from intermediate magma, andesite is classified as felsic rock while basaltic andesite is classified as mafic rock in Figure 2.10B. All the rock sample data compiled for this thesis are plotted in Figure 2.11, illustrating what are thought to be the primary rock compositions.

Figure 2.10A was then used to identify which samples had experienced alteration. Samples which has clearly been altered were excluded from this study to ensure that interpretations are based only on good samples. Figure 2.12 shows all samples which had been classified as felsic using Figure 2.11. The samples that plot in the andesitic, rhyolitic and dacitic areas were accepted for tectonic discrimination, while those plotting in, for instance, the basaltic field were excluded. A similar process was used to identify unaltered mafic samples.

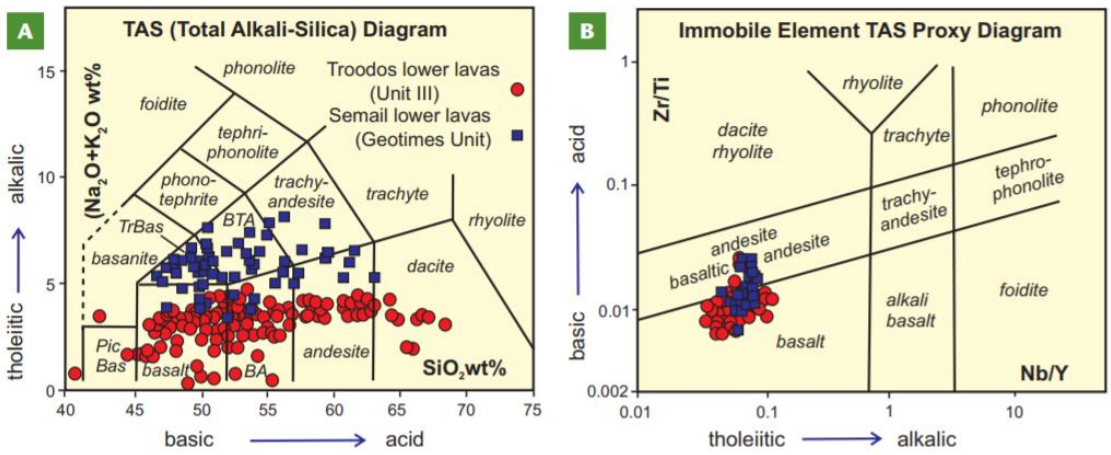

Figure 2.10 The different methods of separating different types of igneous rock (Pearce, 2014) A. major element Si, Na and K value served as parameter. B. immobile element served as proxy (sample in the figure are from the original article, it is only shown to explain the separation effect of these two diagrams and has no connection with the samples from this thesis)

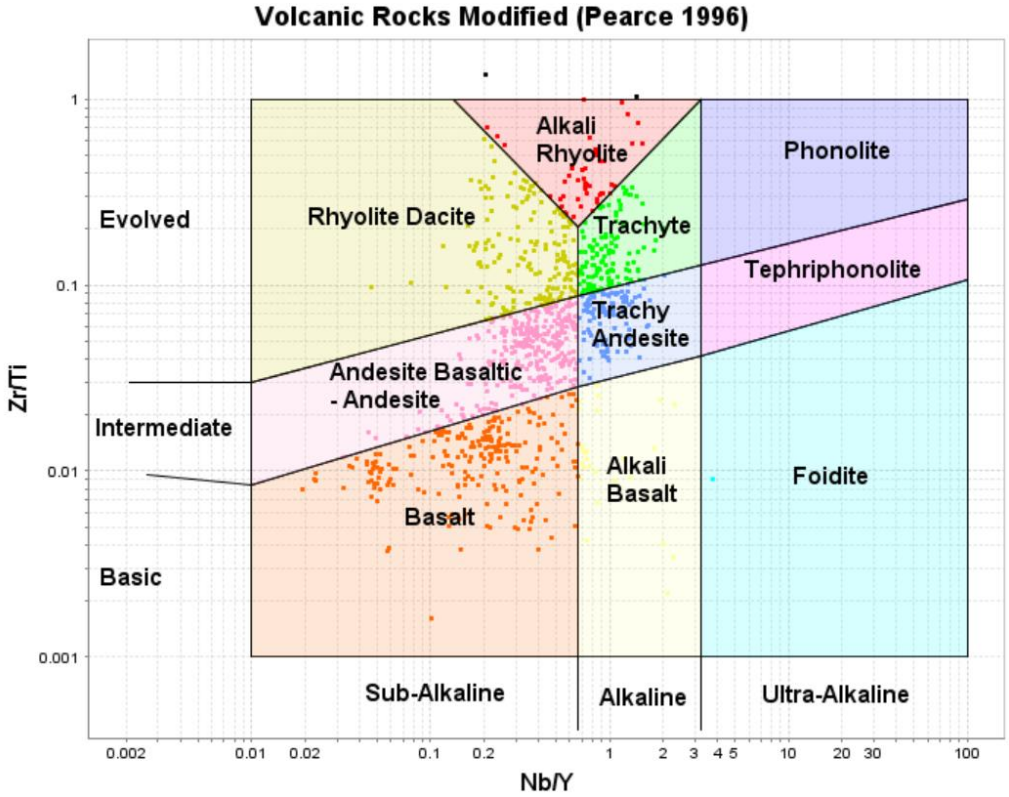

Figure 2.11 Litholigical classification of all the igneous samples in this study (Modified after Pearce, 1996a) and produced using ioGas software (www.reflex.com). Lithology terminology used is for volcanic rocks but should also be taken to include plutonic equivalents.

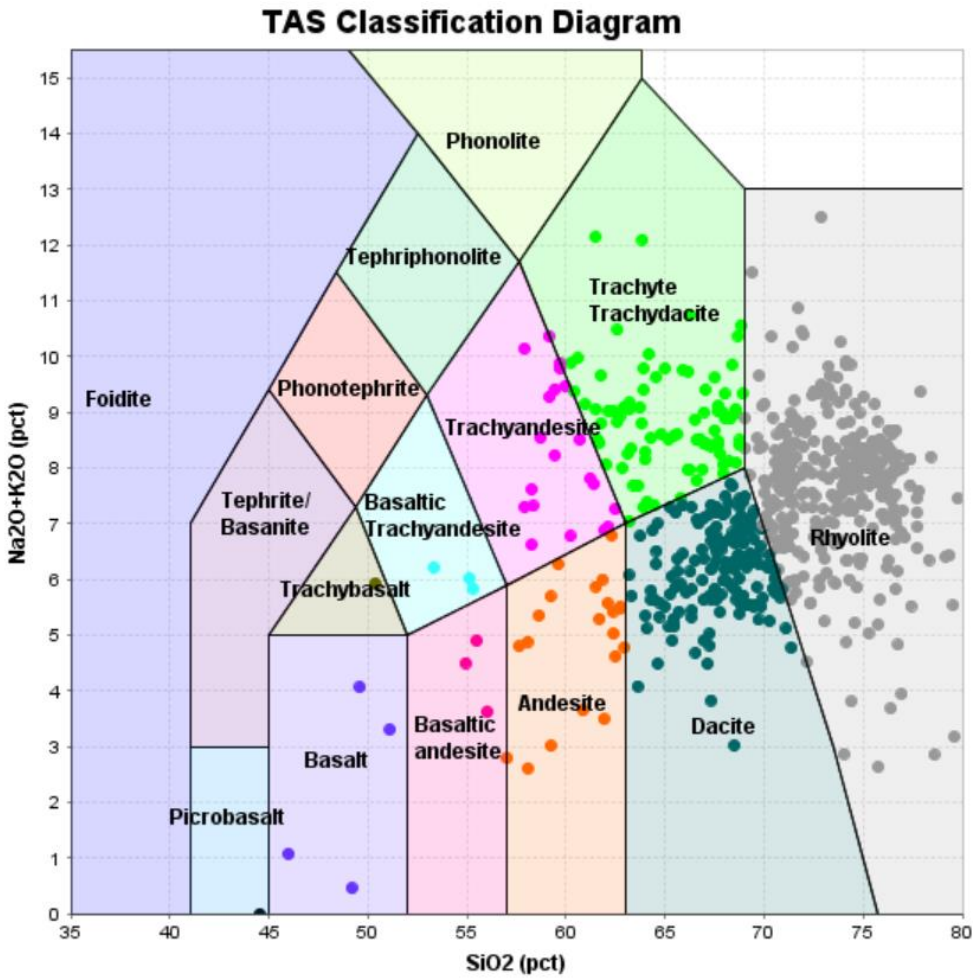

Figure 2.12 Diagram to check alteration for rocks division for felsic rock of this study. Discriminated felsic and mafic rocks is brought to this diagram again to check for alteration. Lithology terminology used is for volcanic rocks but should also be taken to include plutonic equivalents.

It has been shown that igneous rocks form different tectonic settings tend to have different geochemical compositions (Pearce et al., 1984; Pearce, 2014, 2008, 1983; Rollinson, 2014). For this thesis, the geotectonic setting of felsic rocks has been assessed using immobile element plots involving Nb, Y, Ta and Yb (Figure 2.13), as suggested by Pearce (Pearce et al., 1984).

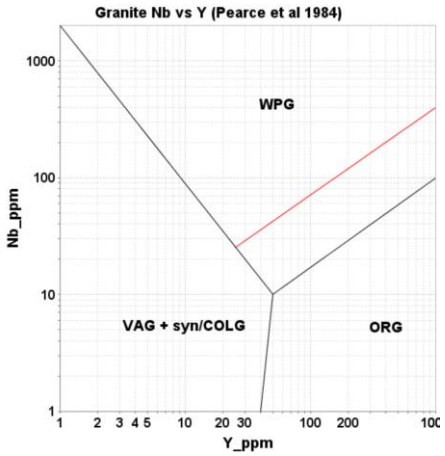

A. Y vs Nb graph

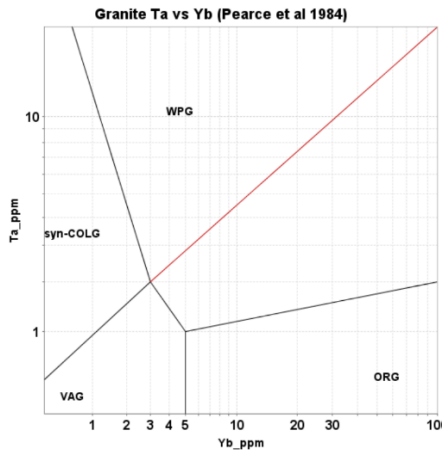

B. Yb vs Ta graph

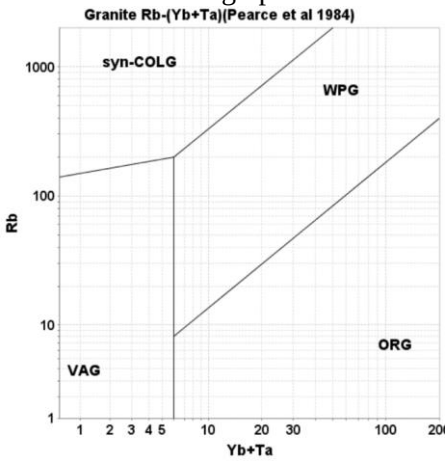

C. Yb+Ta vs Rb graph

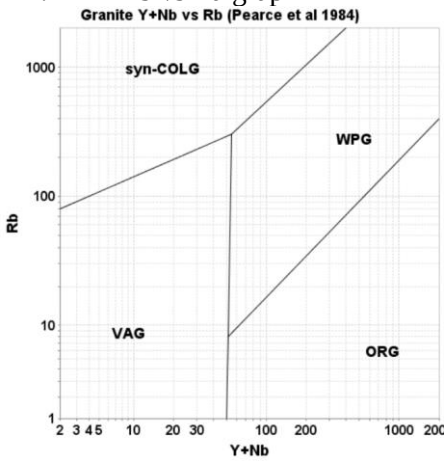

D. Y+Nb vs Rb graph

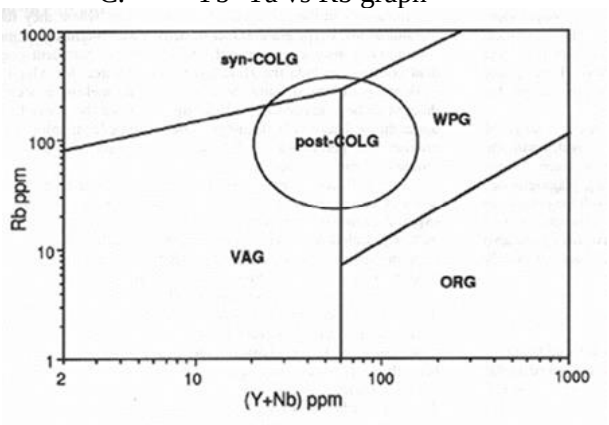

E. Y+Nb vs Rb graph (post-collisional region added on the graph)

Figure 2.13 The felsic rock tectonic setting division: VAG:volcanic arc granite, syn-COLG: syn-collisional granite, WPG: within plate granite, ORG: ocean ridge granite and post-COLG:post-collisional granite (Pearce et al., 1984; Pearce, 1996b).

The felsic discrimination diagrams (Figure 2.13) do not distinguish post-collisional granites from syn-collisional, volcanic arc and within plate granites. As shown in Figure 2.13E, the post-collisional field

overlaps fields for these other granites. Since the compiled data includes ages for the various intrusions, felsic igneous rocks which are younger than major intrusive episodes have been assumed to be post collisional and have been omitted from the initial geochemical geotectonic classification. Based on the igneous activity assessment in Chapter 4, samples considered to have formed in post-collisional settings occur in the age ranges and locations: 750-600 Ma (Jiangnan Orogen, Qingling-Dabie Orogen, and Sulu block), 280-181 Ma (SCB's southwest adjacent area with Indochina block) and 114-0 Ma (all samples in SCB). With these sample excluded, Figure 2.13A-D effectively discriminate the felsic samples in this study. The discrimination results are shown in Chapter 3.

Geochemical discriminations of tectonic settings for mafic rocks follows Pearce (Pearce, 2014, 2008) using immobile element ratios Nb/Yb vs Th/Yb (Figure 2.14). Those mafic samples selected by diagrams in Figure 2.11 and Figure 2.12 were used in this diagram to show which types of settings they come from, specifically: continental arcs which are more evolved arcs; oceanic arcs which are juvenile arcs; N-MORB which are normal type of mid ocean ridges; E-MORB which are enriched type of mid ocean ridges and OIB which are ocean island basalts. Rocks from back-arc settings generally plot in the space between the arcs (purple and green fields) and the mantle array (red field).

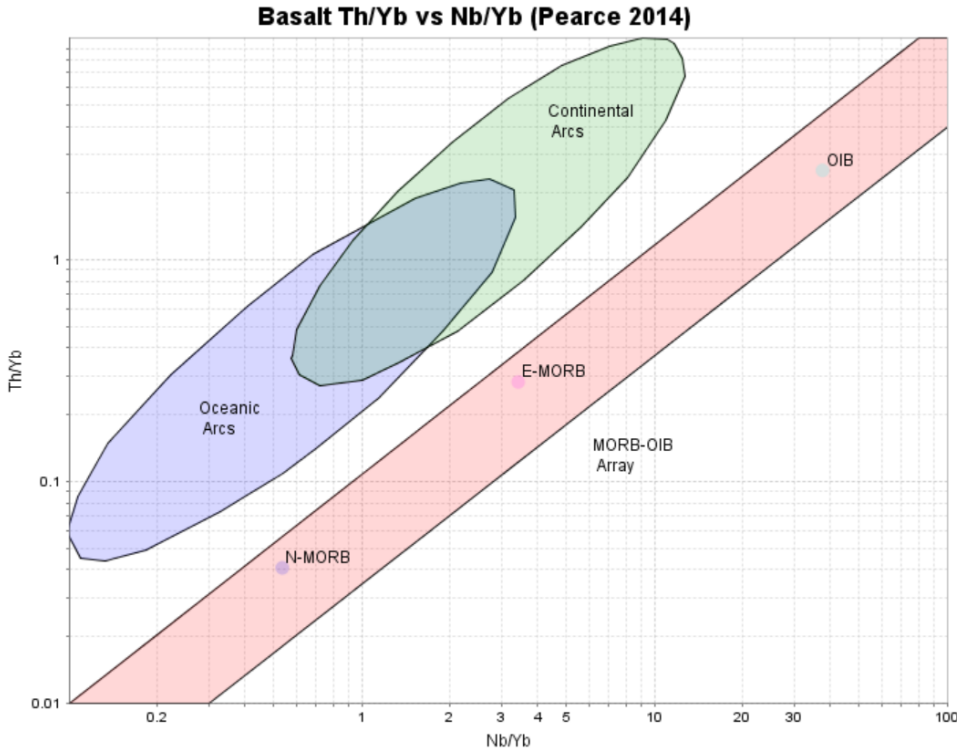

Figure 2.14 Basaltic rock discrimination diagram (Pearce, 2014)

2.6 Metamorphic rocks

Geochronology data used in this thesis for metamorphic rocks are from zircon and monazite U-Pb dating. No titanite data are available in the literature. As mentioned above, zircon and monazite U-Pb dating system have high blocking temperature (Rollinson, 2014). Therefore, each individual record of the metamorphic samples in this study represents the near peak metamorphic crystallization or recrystallization age of the sample instead of the cooling age. These data are used to compare age probability peaks with sedimentary rocks or igneous rocks samples and are thought to represent collisional events in the SCB. In this study, 66 samples (56 zircon U-Pb samples and 10 monazite U-Pb samples) from published articles were compiled in the database. Locations of the metamorphic samples are shown in Figure 2.15. The details of the data are discussed in Chapter 4 and Chapter 5.

Only one metamorphic age is available for the 900-800 Ma time period. In part, this may be because Chinese researchers are mainly focused on dating of igneous lithologies, but may also be because younger (Paleozoic) overprinting has obscured the older ages. More metamorphic dating should be done to further understand the geological history.

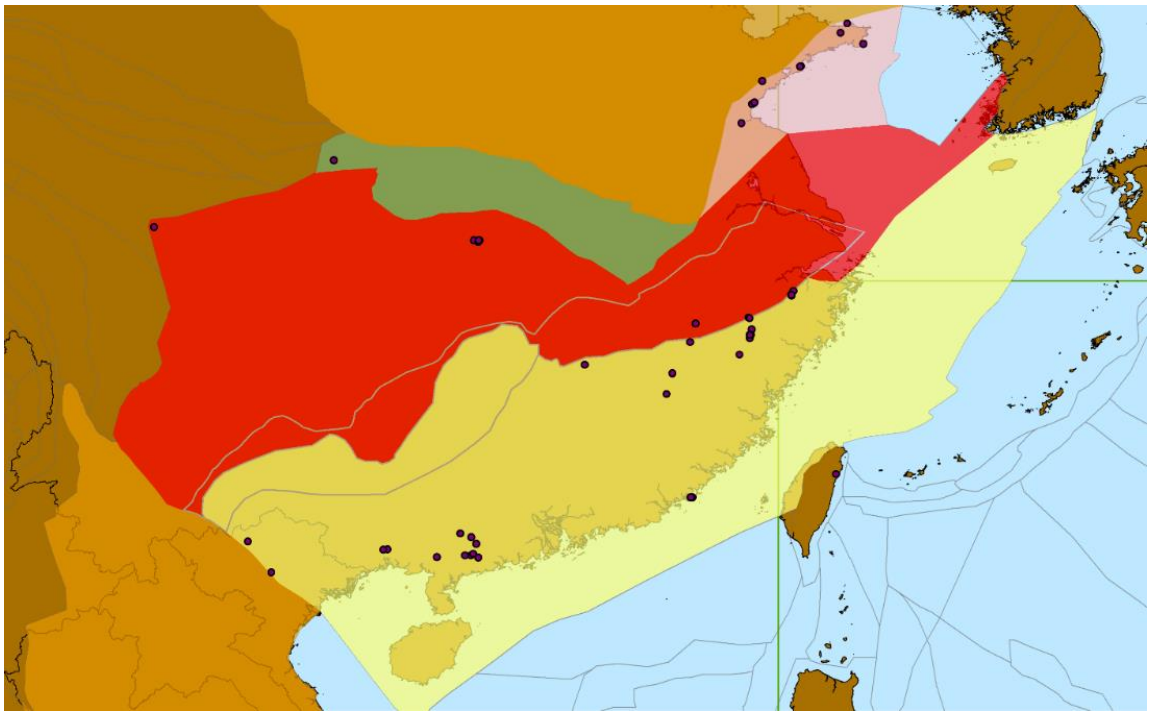

Figure 2.15 Location of SCB metamorphic rock samples used in this study

2.7 Sedimentary rocks

Detrital zircon compositions in sedimentary rocks can be very useful for determining the provenance of the rocks. Detrital zircon U-Pb and Lu-Hf isotope data were compiled from published references. Since detrital zircons in a sedimentary rock could come from multiples sources, data for each zircon grain in the sample were compiled in the database. More than 10000 detrital zircon grains from 135 rock samples from 24 published articles were compiled for this study. Two thousand five hundred and four grains from 82 of these sedimentary rock samples include Lu-Hf data and were also compiled for further study in this thesis. Reference information of all these samples are available in DateView.

Detrital zircon analyses need to be treated differently from those for igneous zircons in concordia diagrams because one cannot expect them to plot as one group (Spencer et al., 2016). There is also no within -sample way to check what is discordant. Discordance is therefore calculated for each analysis independent of all other grains in the sample. Therefore, the first thing to do when dealing with detrital zircon data is to identify these discordant samples and ignore them. Sample YN07-309 from Zhao's publication (Zhao et al., 2010) is used to illustrate this method (Figure 2.16). All analyses with percentage discordance, calculated as $(1-((^{206}Pb/^{238}U)/(^{207}Pb/^{206}Pb))) *100$, worse than 10% are shown in blue and would be omitted from subsequent calculations. Analyses with one sigma age uncertainties greater than 30 are considered imprecise and were also excluded from the study.

The map distribution of sedimentary samples is shown in Figure 2.17.

Graphical comparison of multiple sample detrital zircon U-Pb and Lu-Hf data was done using FitPDF (Eglington, 2018a; Eglington et al., in press), especially by plotting grain age vs deposition age (Figure 2.18). Major peaks from probability distributions for individual samples are shown in red and orange. Grain analyses should not plot to the left of the diagonal line unless produced by post depositional metamorphism.

FitPDF was also used to calculate cumulative probability distributions for assessing tectonic settings of detrital zircon data (Cawood et al., 2012).

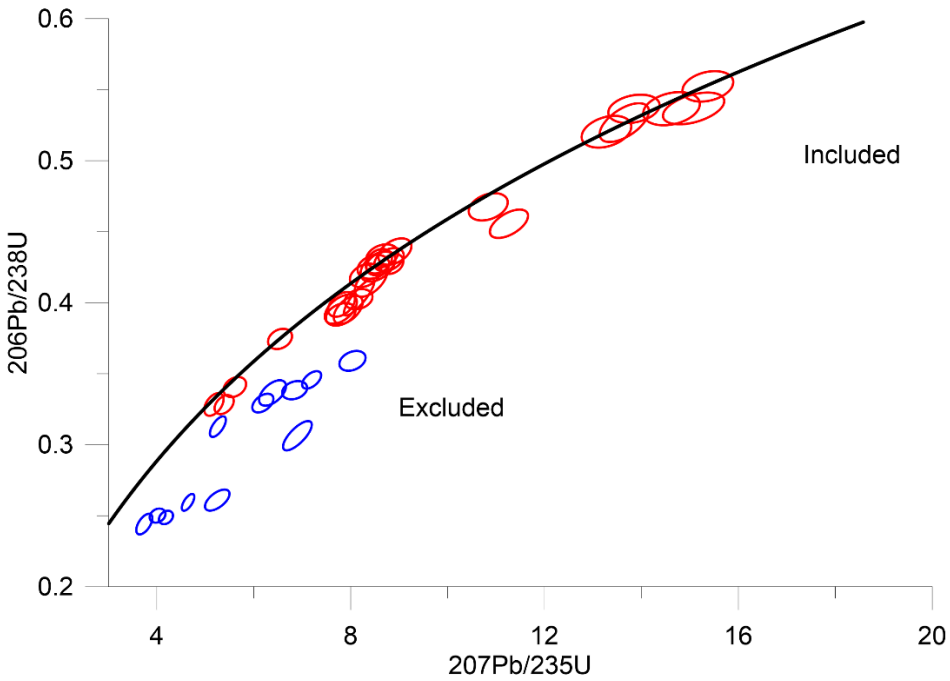

Figure 2.16 Zircon sample YN07-379 (Zhao et al., 2010). Although every grain's U-Pb data are graphed in this figure, only the concordant ones, which are shown in red in this diagram, are accepted for further study.

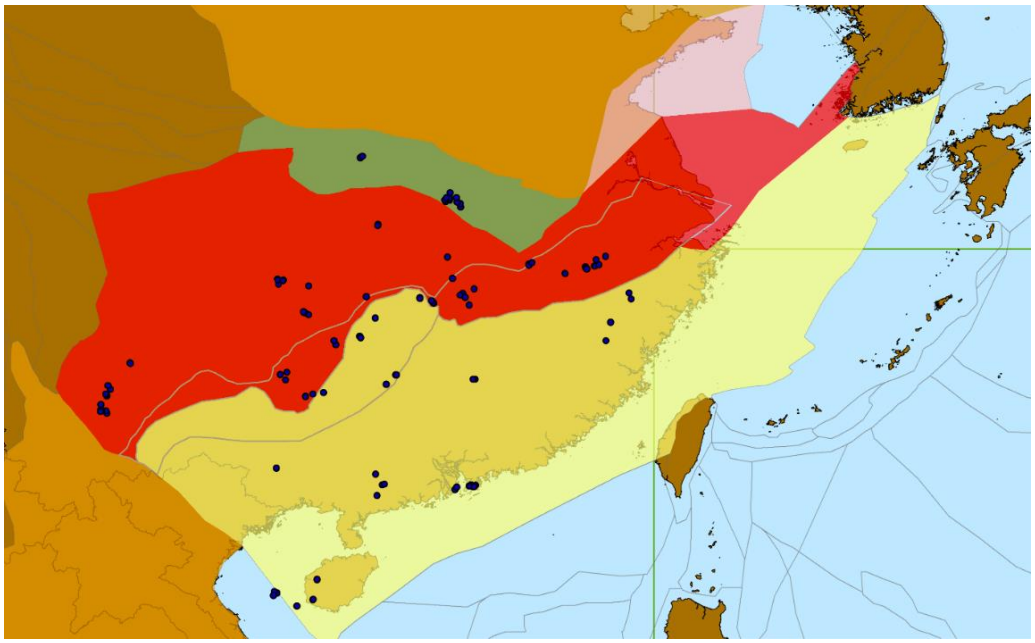
Figure 2.17 Location for the sedimentary rocks used in this study.

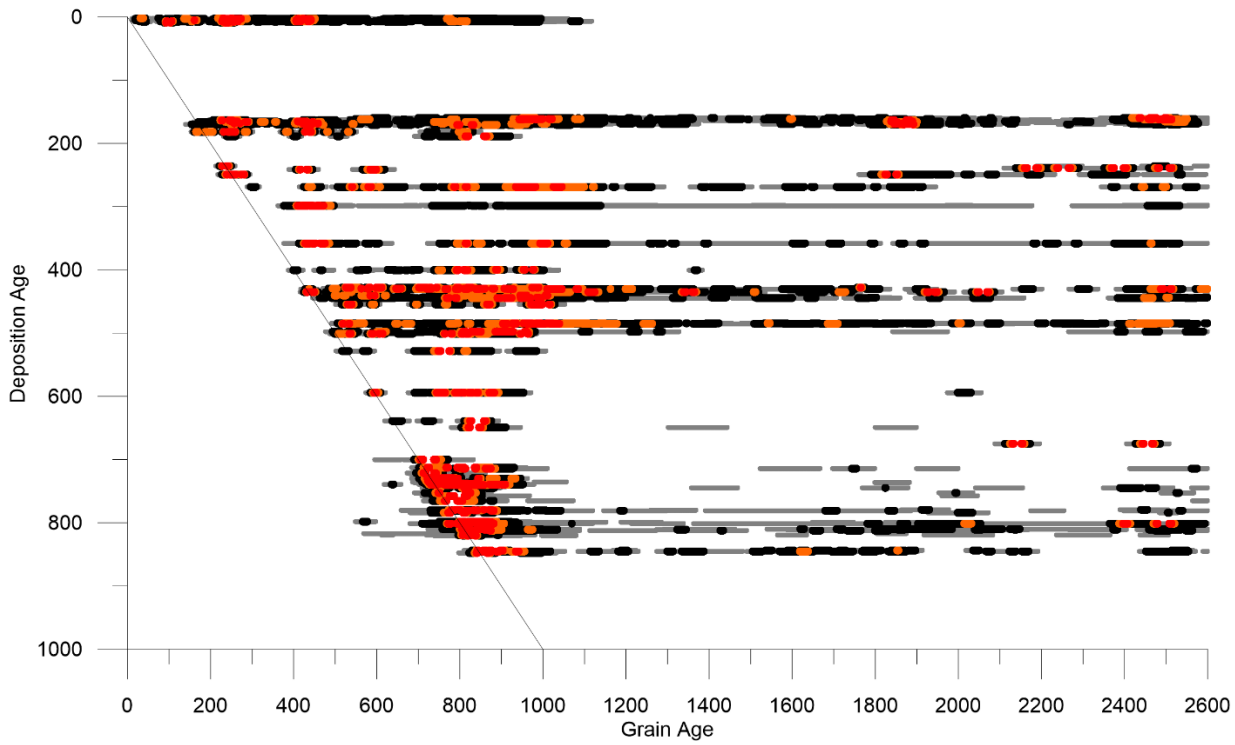

Figure 2.18 Plot of grain age relative to deposition age for detrital zircon data, as produced using output from the FitPDF program. Red: detrital zircon crystallization age peak probability 80%-100% of maximum peak height; Orange: detrital zircon crystallization age peak probability 60%-80%; Black: detrital zircon crystallization age peak probability 40%-60%; Grey: detrital zircon crystallization age peak probability 10%-40% (Eglington, 2018a)

CHAPTER 3
IGNEOUS ACTIVITY

3.1 U-Pb geochronology

Igneous activity in the SCB provides one view of the geological history of the region. Igneous data is mostly used to facilitate comparisons between the various blocks relative to time and space. Unlike many previous studies, the wide regional coverage of the compilation for this thesis allows one to see patterns and changes that are important for the development of the entire SCB. Figure 3.1A shows the location of igneous samples compiled in DateView, which are considered relevant to this project. Many more data are available in DateView but are not considered here because they do not appear to influence or relate directly to the development of the SCB. Data from Tibet and Northern India are included because this region may have been an important source of detrital zircons deposited on the SCB, as will be discussed in Chapter 5. Figure 3.1B shows the variation in age probability distribution for the region, with several distinct episodes of igneous activity. Eight intervals of igneous activity have been distinguished by colour in this latter diagram, each of which is also restricted in geographic space, as shown in Figure 3.2.

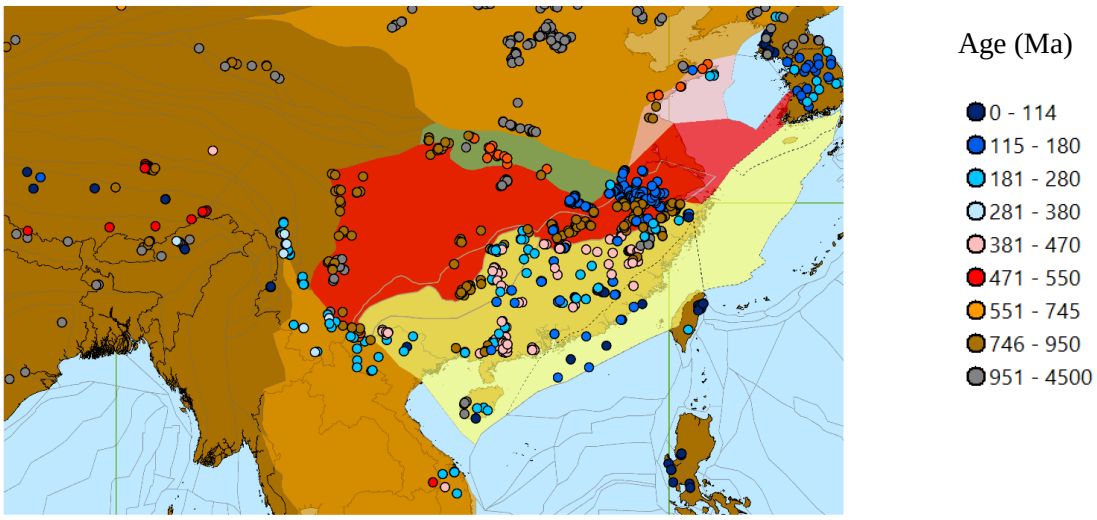

A.

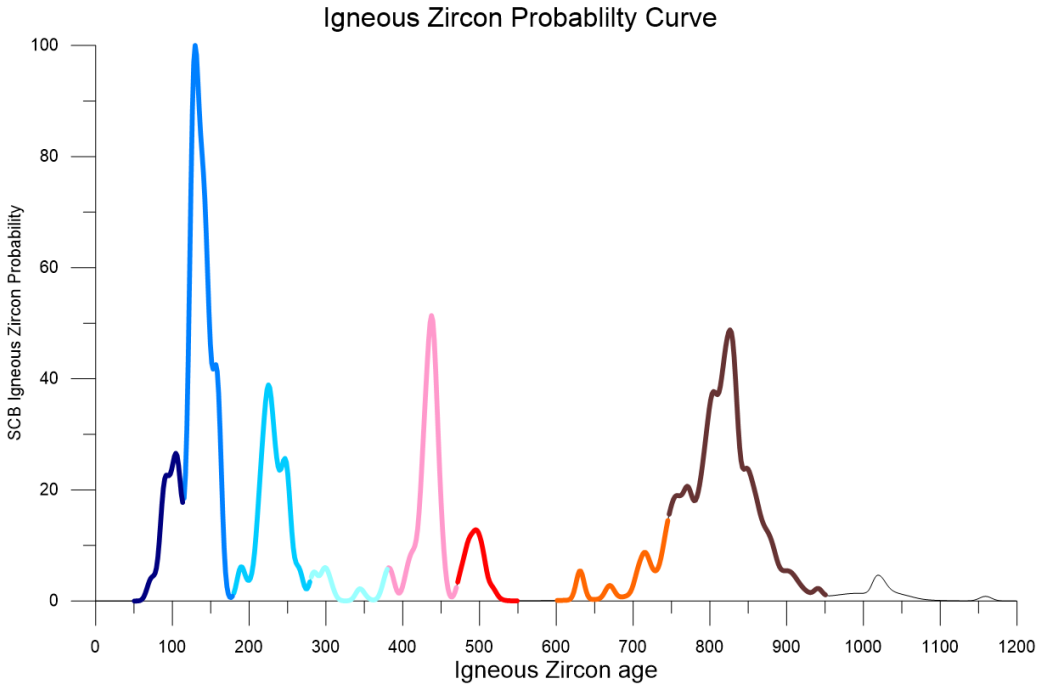

B.

Figure 3.1 A. Distribution of igneous samples from Asia, concerntrating on samples from the SCB and immediately adjacent blocks where relevant to the geological history of South China. All data were compiled in and extracted from the DateView database. B. Age probability distribution of the igneous ages of the SCB (Gaussian 'AND' summation), Tibetan area and Indochina block (locations shown in Figure 3.2). Colours used for the age peaks are the same as shown in the colour legend in A. The probability curve for samples with crystallization ages older than 950 Ma have not been labelled in B as most of the samples are probably not linked with the assembly of the SCB

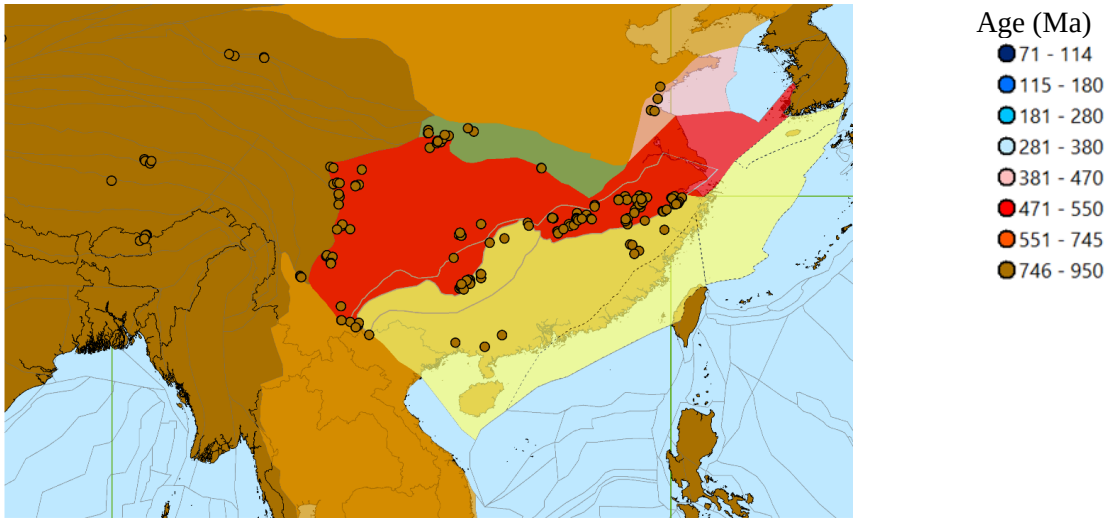

A. 950-746 Ma age group

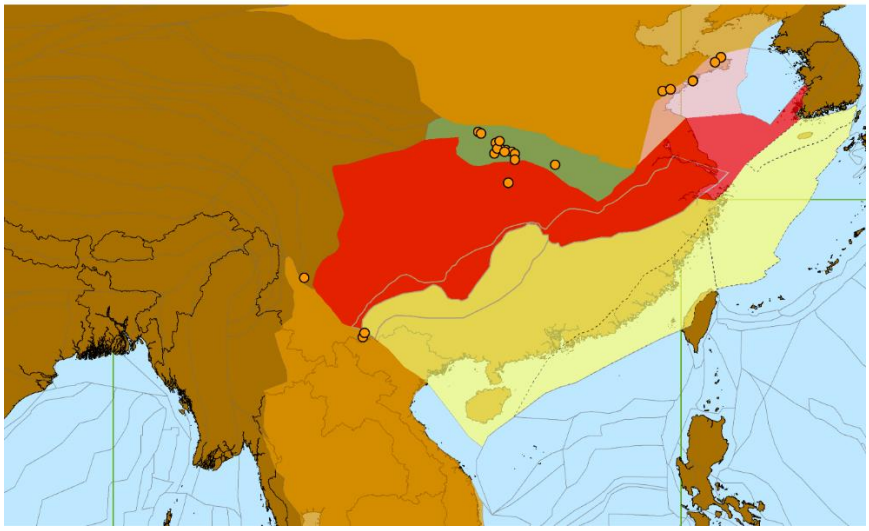

B. 745-551 Ma age group

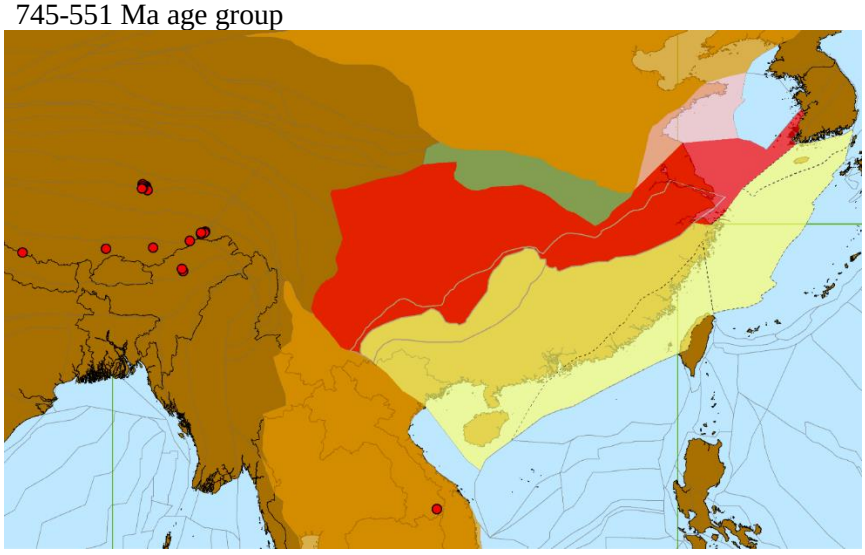

C. 550-471 Ma age group

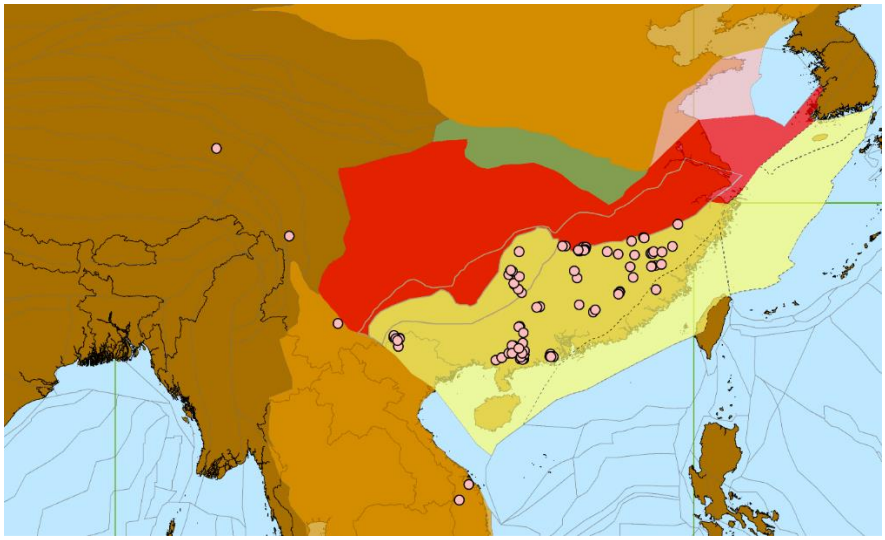

D. 470-381 Ma age group

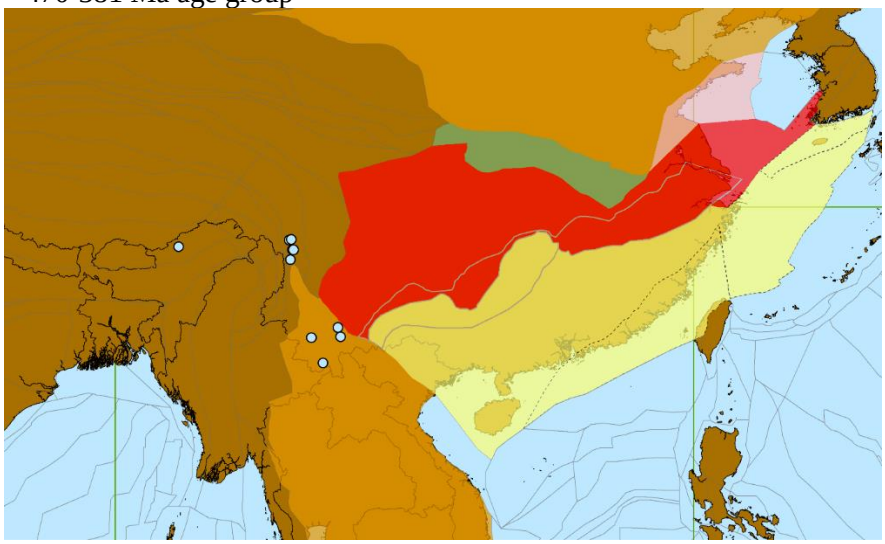

E. 380-281 Ma age group

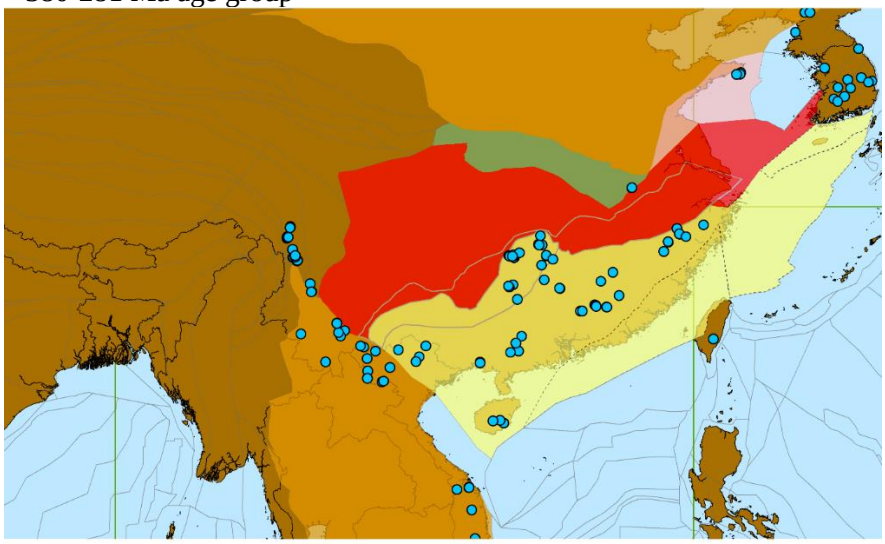

F. 280-181 Ma age group

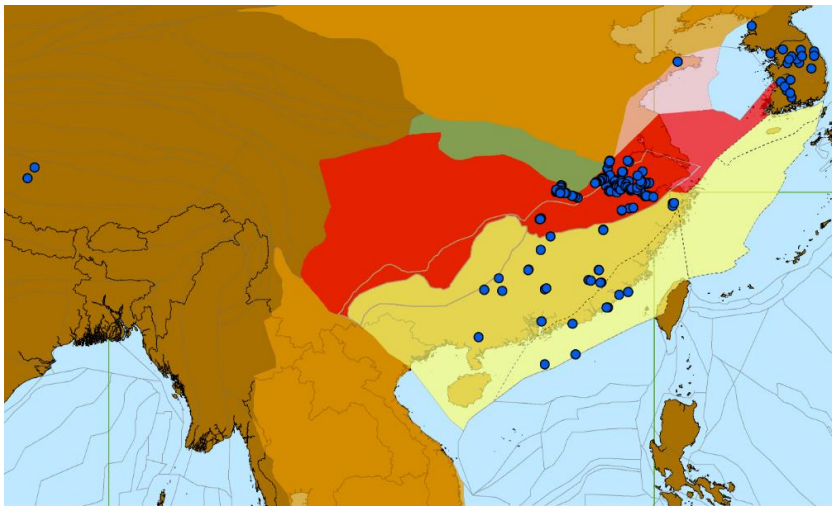

G. 180-115 Ma age group

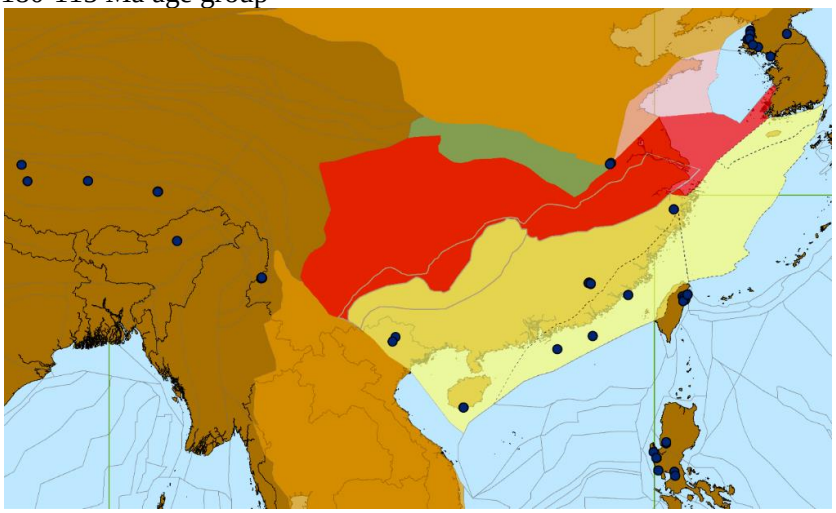

H. 114-0 Ma age group

Figure 3.2 Igneous samples grouped by age, illustrating the location of igneous activity in the eight time intervals important for development of the SCB.

Each of the coloured age intervals from Figure 3.1 represents different stages in the development of the SCB, as described below:

950 Ma to 746 Ma (Figure 3.2A)

Widespread Neoproterozoic igneous activity occurred around the northwestern and western margins of the Yangtze block from 950 Ma to 746 Ma and in the Jiangnan Orogen from 950 Ma to 850 Ma (Figure 3.2A). Very little igneous activity occurred in the Cathaysia block during this time interval. Igneous activity in volcanic arc settings occurs on the upper plate. The only igneous activities likely on a lower plate is plume related, none of which produces linear belts at right angles to plate motion. In this case, the

concentration of igneous activities on the Yangtze block suggests that it was in an upper plate setting and Cathaysia in a lower plate setting.

745 Ma to 551 Ma (Figure 3.2B)

Samples of this age are distributed in regions adjacent to the Yangtze block; in the Qingling-Dabie belt, the Sulu belt and south of the Red River fault in Indochina. Presumably, none of this activity was directly related to the development of the SCB itself.

550 Ma to 471 Ma (Figure 3.2C)

Almost all activity in this time interval occurred in Tibet and northern India. One sample is seen in the Indochina block, but no record has been seen from the SCB.

470 Ma to 381 Ma (Figure 3.2D)

This was a major interval of igneous activity in the SCB, with most activity seen in the Cathaysia block. The Geological Atlas of China (Ma et al., 2002) shows the Yangtze block covered by an epeiric sea at this time. Tectonic inversion of the basement is recorded for the Cathaysia block and paleocurrent directions support derivation of sediments in the Yangtze block from the south east (Yao and Li, 2016).

380 Ma to 281 Ma (Figure 3.2E)

According to the probability curve and the position of the samples in this time interval, a small event happened in blocks currently located adjacent to the western margin of the SCB. The activities in this age spectrum might represent interactions between the SCB and the Indochina block.

280 Ma to 181 Ma (Figure 3.2F)

Igneous activity during this interval was common throughout the Cathaysia block, in northern Indochina and in the Korean peninsula. This magmatism was associated with the approach and collision of the SCB and the NCB at about 200 Ma (Enkin et al., 1992; Li et al., 2017; Li, 2014).

181 Ma to 115 Ma (Figure 3.2G)

Many of these samples may represent post collisional magmatism after collision of the SCB and the NCB (Li et al., 2017), but those in the east could also be due to the start of subduction of the Pacific oceanic plate beneath Asia. The Cathaysia block collided with the Tolo block at ~160 Ma (Sewell et al., 2016), but little igneous activity is evident.

114 Ma to 0 Ma (Figure 3.2H)

Limited igneous activity has been dated in this age spectrum, mostly around the southern coast of the Cathaysia block. These ages probably represent continued subduction of the Pacific plate beneath Asia and, for samples in northern India, collision of India with Asia to form the Himalayas.

3.2 Isotope geochemistry

Isotope geochemical data provide an indication of the nature of pre-existing crust in a region. Isotope signatures allow one to distinguish between juvenile formation of crust and reworking of older crust and therefore adds additional information to the record of igneous activity to be described in section 4.1.

Chapter 2 described a method to combine Lu-Hf and Sm-Nd epsilon values to the same colour range (Figure 2.8). Figure 3.3 shows maps illustrating the real and calculated equivalent epsilon Nd composition of igneous rocks for each of the time intervals which will be described in section 4.1. Samples which originally had Sm-Nd data have their εNd values plotted as triangles in Figure 3.3; and on the other hand, samples for which equivalent εNd is calculated from εHf are marked as circles. Three hundred and thirty-eight samples have data for which εHf were transposed to equivalent εNd and are plotted together with 393 original εNd values.

Most of the samples plotted in Figure 3.3 show negative εNd values. More positive values are seen in three age groups. These age groups are consistent with age groups noted in section 4.1. The oldest age group is for crystallization ages greater than 950 Ma and has both positive and negative values. All samples occur in or near the Yangtze block (Figure 3.3A). This indicates that these oldest igneous rocks involved formation of both juvenile crust and reworking of older basement. In the 950-746 Ma age group (Figure 3.3B) however, most of the samples show relatively positive epsilon Nd values; only some of the samples located in the Jiangnan Orogen show negative values. This indicates that, at this age, most of the igneous lithologies were juvenile. Samples from the younger age groups (<745 Ma) (Figure 3.3C-G) of the SCB don't have positive epsilon values, thus juvenile crustal involvement is not seen in these samples. Some samples in the Qingling-Dabie Orogen, formed at 745-551 Ma, are also juvenile.

In short, the isotope data shows that in the 950-746 Ma and older age groups, juvenile magmatism occurred, mostly in the Yangtze block. These positive epsilon Nd and equivalent epsilon Nd values are thought to be due to the formation of volcanic arcs as a result of subduction of the Cathaysia block beneath the Yangtze block. Negative Nd values seen in the Jiangnan Orogen result from the reworking of older crustal sources. Since this is the only interval involving substantial formation of juvenile crust, this is probably the period when the amalgamation of the SCB happened. More negative epsilon Nd values in the younger age groups (<745 Ma) indicate that all these lithologies were generated by reworking of older protoliths.

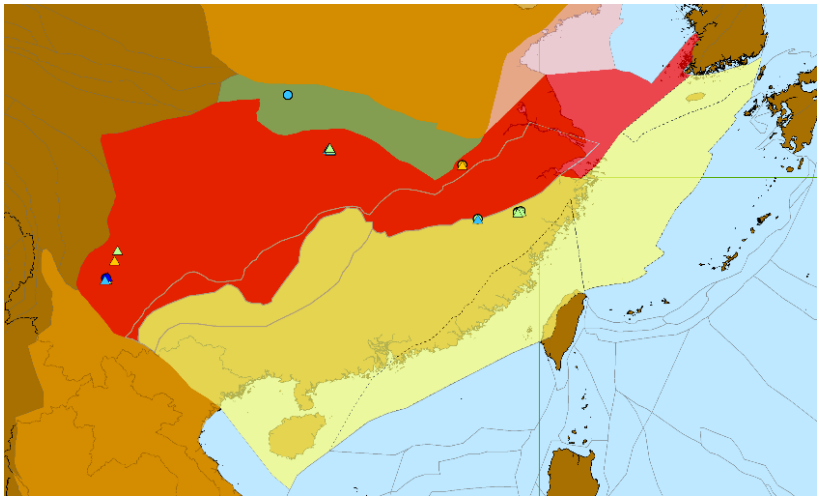

Legend:
εNd(t) sample original value is marked as triangle, εNd(t) equivalent value transposed from εHf(t) is marked as circle shape

- -20- -15
- -15 - -7
- -7 - 0
- 0- 5
- 5 - 10

A. εNd(t) value of samples U-Pb age >950 Ma

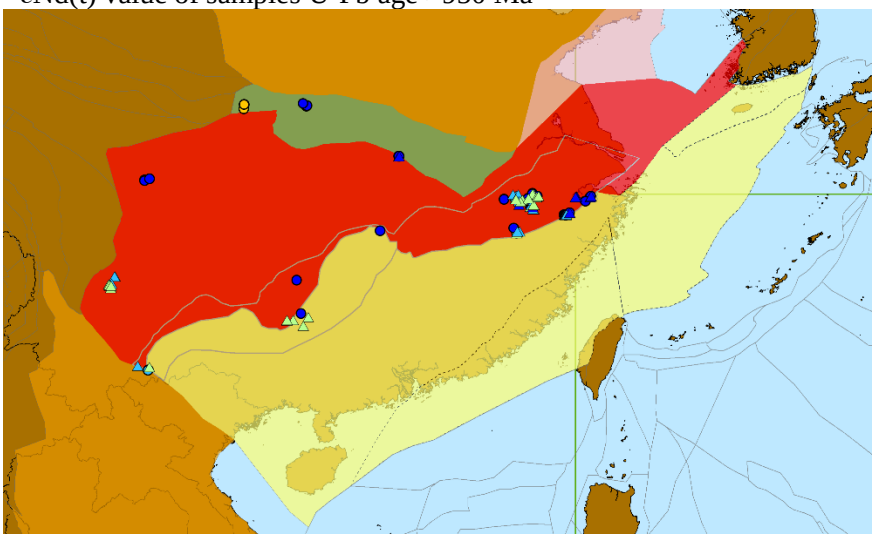

B. εNd(t) value of samples dating age of 950-746 Ma

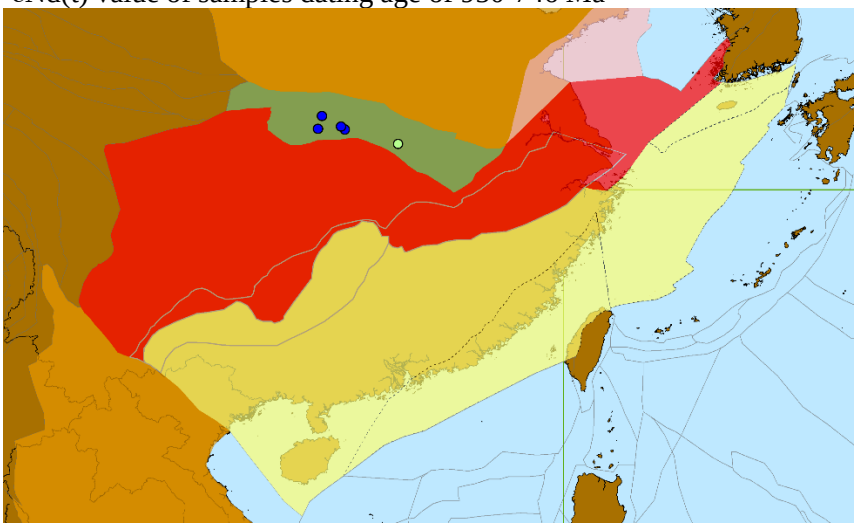

C. εNd(t) value of samples dating age of 745-551 Ma

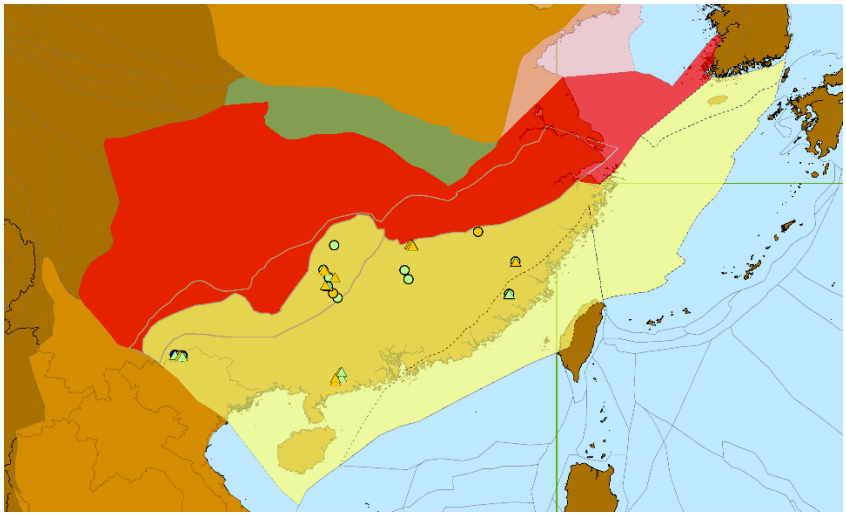

D. εNd(t) value of samples dating age of 470-381 Ma

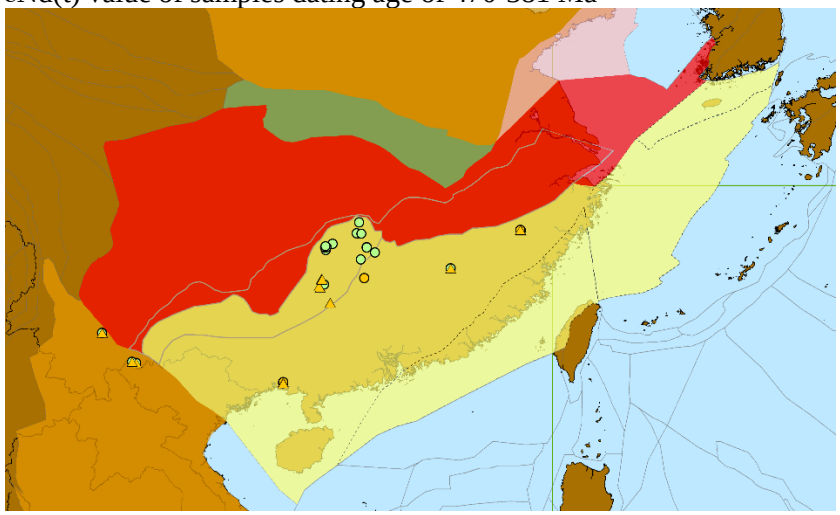

E. εNd(t) value of samples dating age of 280-181 Ma

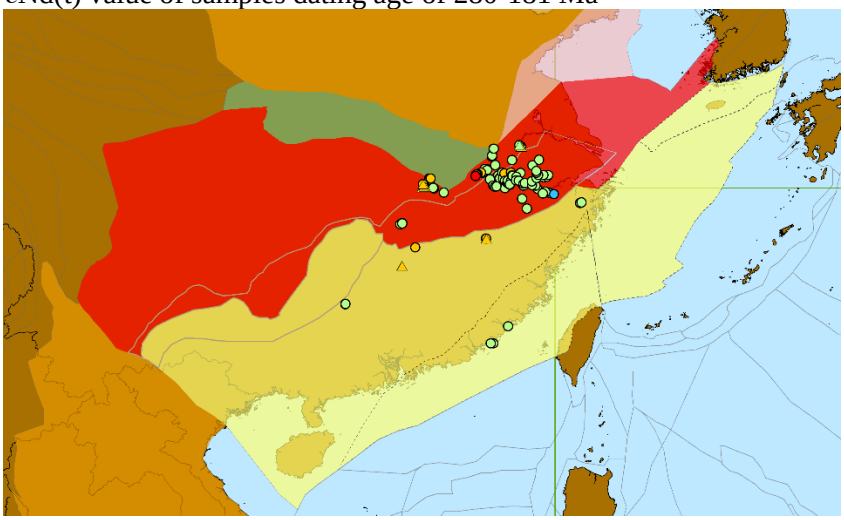

F. εNd(t) value of samples dating age of 180-115 Ma

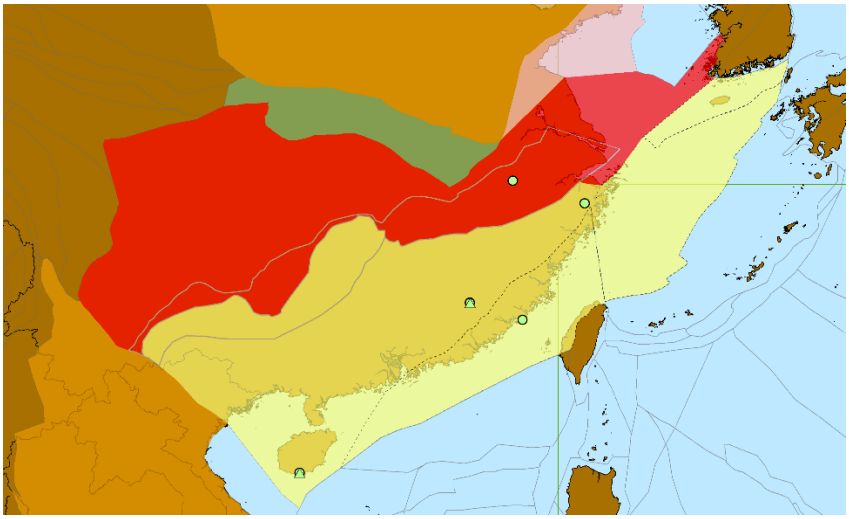

G. εNd(t) value of samples dating age of 114-0 Ma

Figure 3.3 εNd(t) value and equivalent calculated value plot on the SCB location map.

3.3 Lithochemistry and inferred tectonic settings

3.3.1 Felsic rocks

In Chapter 2 and Chapter 3, the post-collisional settings of felsic rocks were identified based on the age of samples relative to major episodes of igneous activity. In this chapter, the assessment of felsic rock tectonic settings is divided into two parts: post-collisional samples and non-post-collisional samples. Figure 3.4 and Figure 3.5 show samples, excluding those interpreted to be from post-collisional settings. Samples in Figure 3.4 are coloured as in Figure 2.12. Andesites, trachyandesites and dacites (and their plutonic equivalents) are mostly from volcanic arc settings while rhyolites occurred in all settings. Figure 3.5A illustrates the classification of felsic lithologies into volcanic arc (red), syn-collisional (yellow), within plate (blue) and ocean ridge (light blue). This diagram is based on two immobile elements (Y and Nb) and a potentially mobile element (Rb), although samples with obvious alteration have been screened out based on Figure 2.11 and Figure 2.12. Similar diagrams, utilizing Ta instead of Nb or Yb instead of Y, are shown in Figure 3.5B-D. Symbol colours for samples are the same as the classification from Figure 3.5A so as to illustrate differences in classification of some of the samples between the different diagrams. Classification for most of the samples is consistent across different diagrams, the most noticeable difference being that some syn-collisional samples plot in the within plate field of Figure 3.5C and D. For the remainder of this thesis, sample classification is based on the plot of Y+Nb vs Rb.

The chemistry data results were combined with the isotope geochemical data to further show the provenance of the igneous rocks. In Figure 3.6, Lu-Hf isotope data are shown together with the tectonic setting discrimination results. Figure 3.6A shows the age vs epsilon Hf composition of all data, symbolized by interpreted tectonic settings. Figure 3.6B-E show the similar graphs and maps with the samples subdivided into the age intervals previously identified in section 3.1. Very few Lu-Hf isotope and chemistry data are available for the oldest age group (>950 Ma) (Figure 3.6B) and these data are from a very small area of the SCB. Samples from 950-746 Ma (Figure 3.6C) mostly have positive epsilon values and all samples are from either volcanic arc or within plate settings. This could be an indication of subduction and then collision between Yangtze and Cathaysia, in agreement with the isotope geochemical results. No matching geochemical and Lu-Hf isotope data were found for samples from the 745-551 Ma and 550-471 Ma intervals. The 470-381 Ma age group (Figure 3.6D) shows many negative epsilon values indicating that these rocks were formed by reworking of older crust. Although several volcanic arc settings

are seen in this group, these samples are likely to be generated from continental arc rather than oceanic or juvenile arc settings. The younger age groups (280-181 Ma and 180-114 Ma) (Figure 3.6E and F) all show similar result to those for 470-381 Ma.

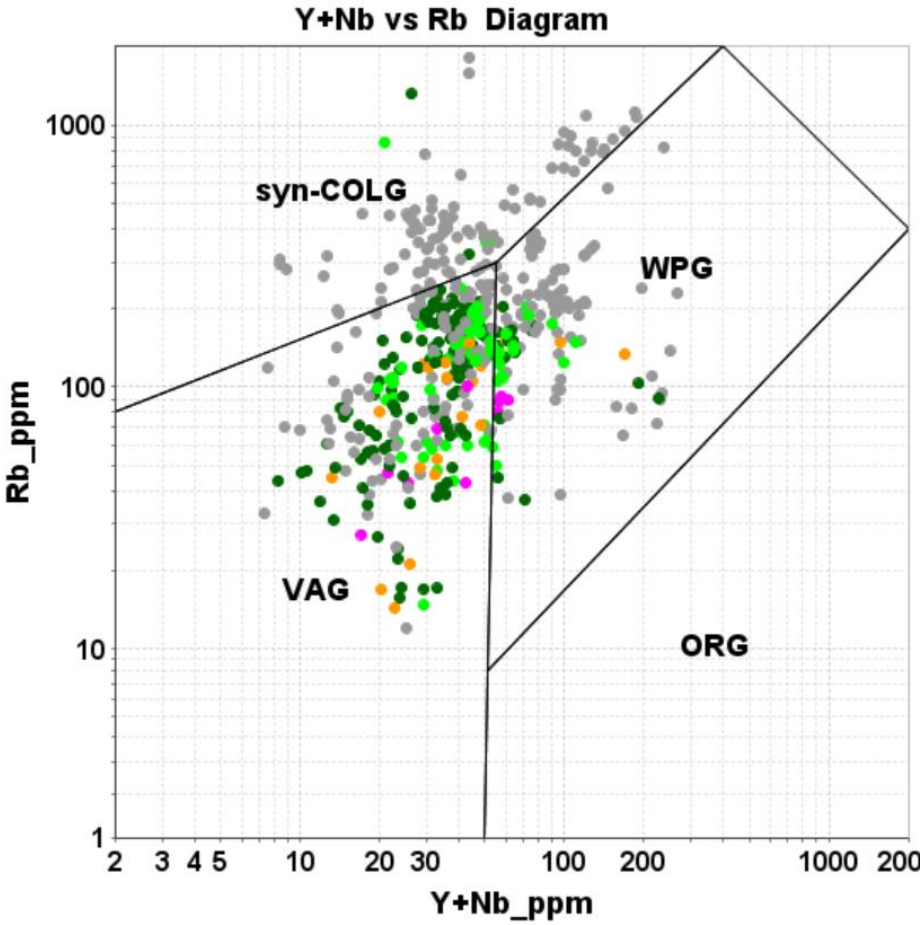

Figure 3.4. Y+Nb vs Rb discrimination of tectonic settings for felsic rocks. Sample coloured by lithology, as classified in Figure 2.12: Orange: andesite; Light green: trachyte and trachydacite; Green: dacite; Purple: trachyandesite; Grey: rhyolite. Lithology terminology used is for volcanic rocks but should also be taken to include plutonic equivalents.

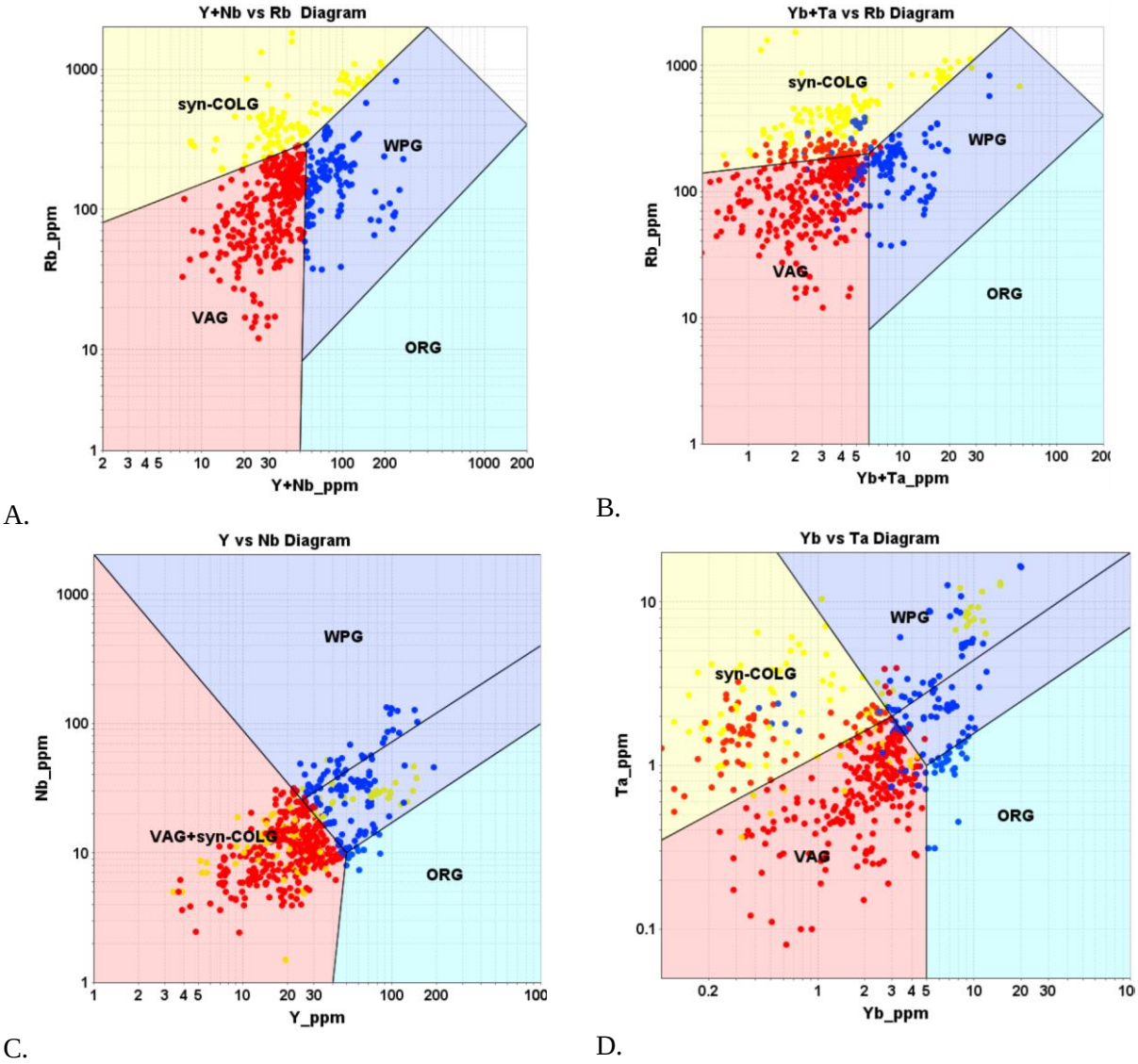

Figure 3.5 Graphs for tectonic setting discrimination of felsic rocks (post-collisional settings excluded). Classification fields after (Pearce et al., 1984). Colour symbology in all diagrams is based on the classification illustrated in the Y+Nb vs Rb diagram.

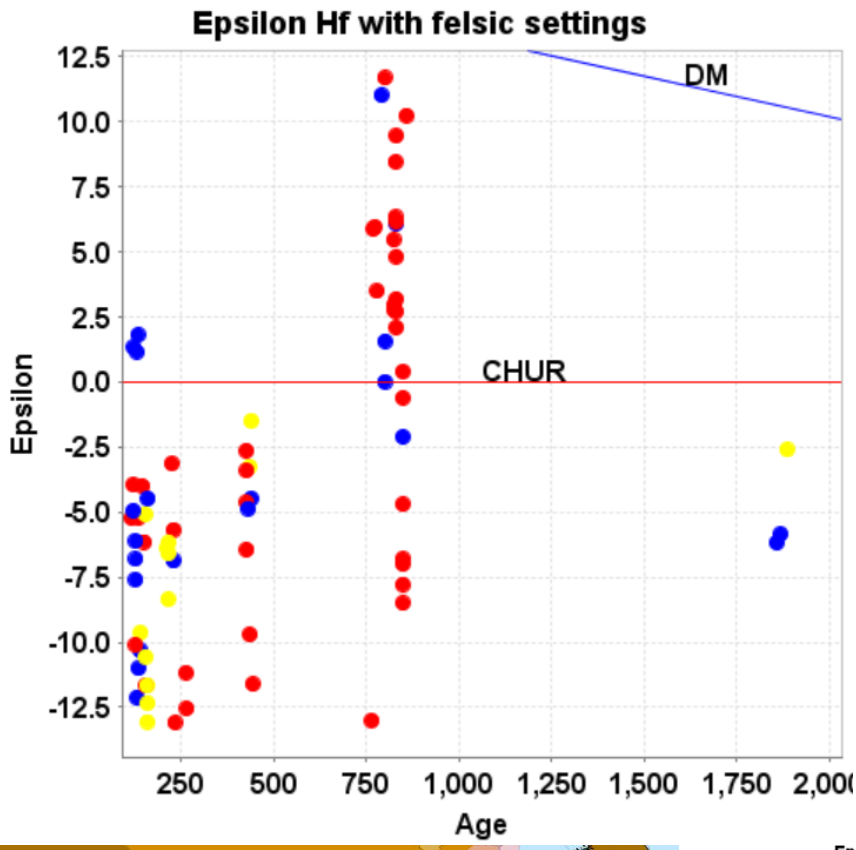

Legend

ORG
VAG
WPG
postcollision
syn-COLG

A. Felsic samples with Lu-Hf isotope data, tectonic settings labelled and εHf(t) composition graphed in this diagram

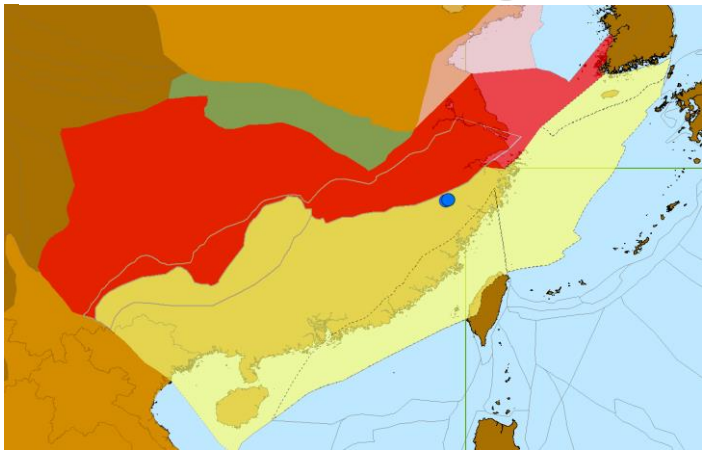

B1. Location of samples older than 950 Ma age group

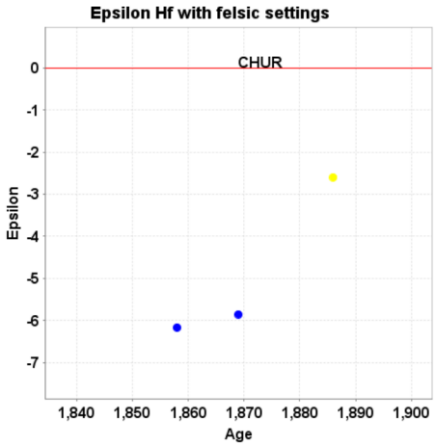

B2. εHf(t) of samples older than 950 Ma

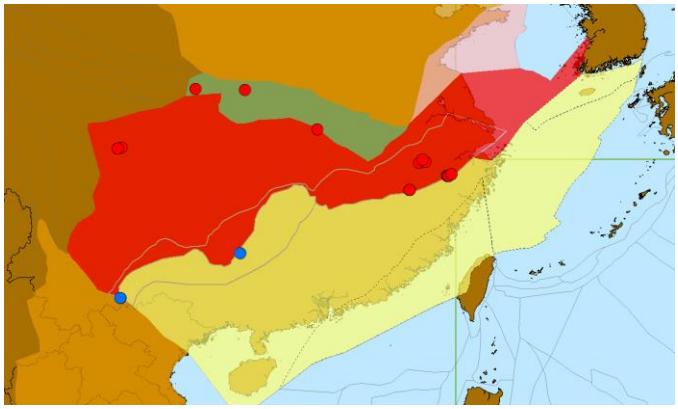

C1. Location of samples from 950-746 Ma age group

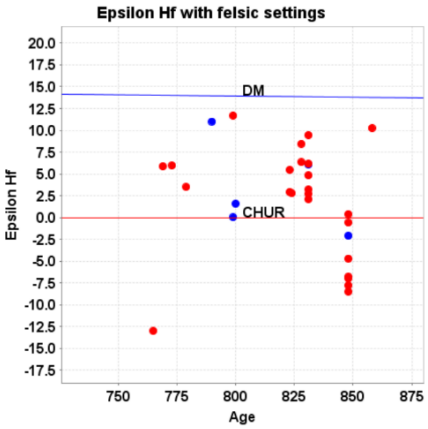

C2. εHf(t) of samples from 950-746 Ma

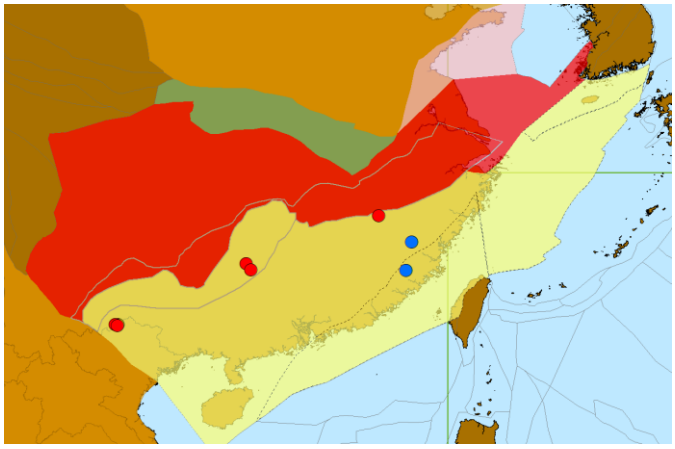

D1. Location of samples from 470-381 Ma age group

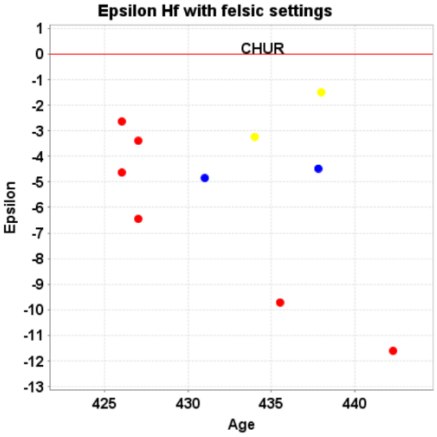

D2. εHf(t) of samples from 470-381 Ma

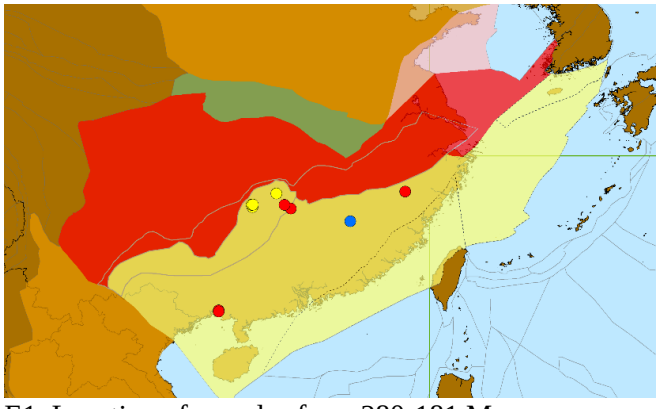

E1. Location of samples from 280-181 Ma age group

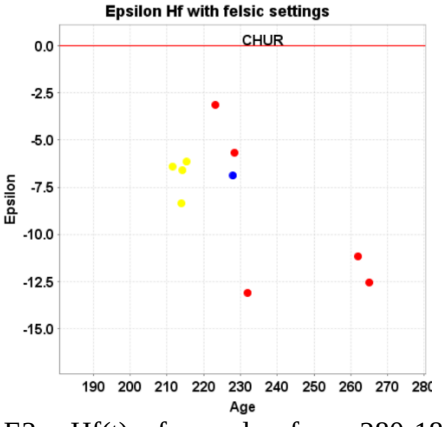

E2. εHf(t) of samples from 280-181 Ma

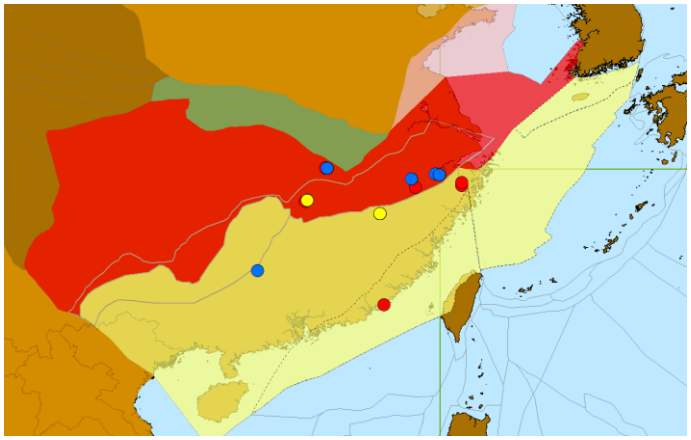

F1. Location of samples from 180-114 Ma age group

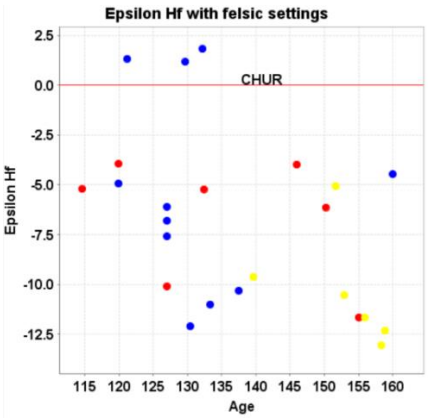

F2. εHf(t) of samples from 180-114 Ma

Figure 3.6 Lu-Hf isotope compositions and interpreted tectonic settings for felsic igneous rocks (without post-collisional settings).

Similar to the Lu-Hf samples, results for Sm-Nd isotope and chemistry data for the oldest age group (>950 Ma) (Figure 3.5B) occur in the Yangtze block and areas near the western margin of the Cathaysia block. From Figure 3.6C we can see that samples from 950-746 Ma mostly have positive epsilon values and all samples are from either volcanic arc or within plate settings. No matching geochemical and Sm-Nd isotope data were found for samples from the 745-551 Ma and 550-471 Ma intervals. The 470-381 Ma (Figure 3.6D) age group shows only negative epsilon values indicating that these rocks were formed by reworking of older crust. Many of the samples are classified as coming from syn-collisional settings. The younger age groups (280-181 Ma and 180-115 Ma) (Figure 3.6E and F) have negative epsilon values and many of the samples are classified as forming in volcanic arc settings, although it is not clear whether the chemical signature might be inherited from older formation in volcanic arcs.

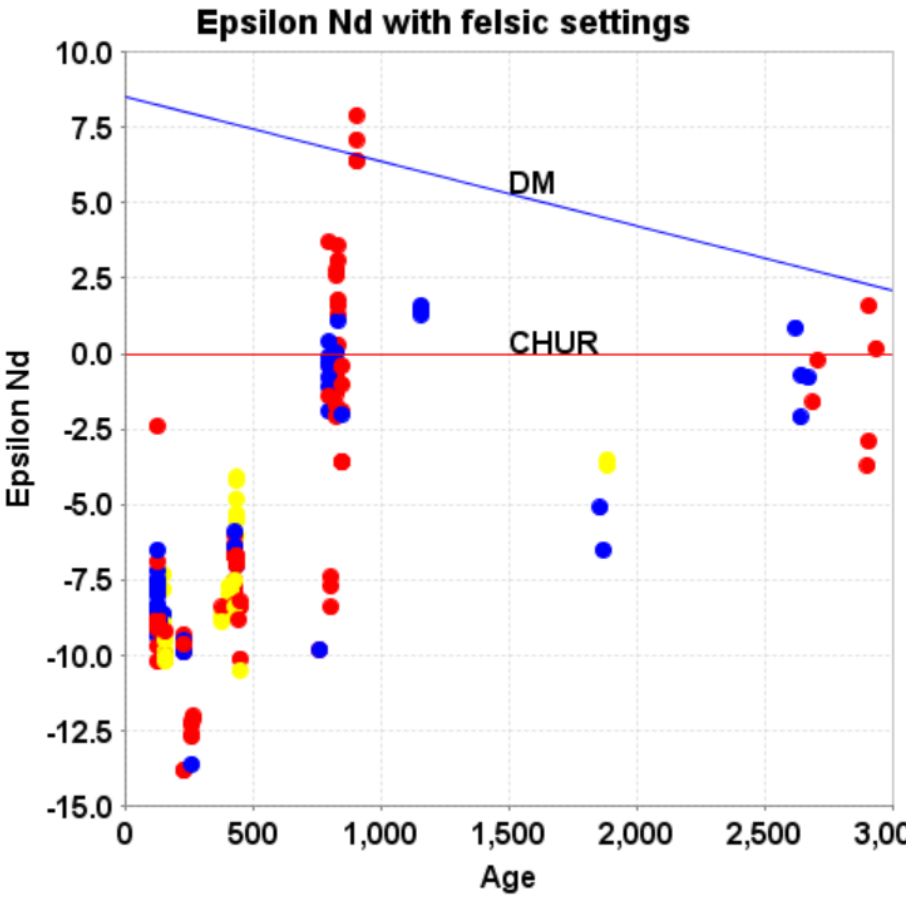

Legend

ORG
VAG
WPG
postcollision
syn-COLG

A. Felsic samples with Sm-Nd isotope data, tectonic settings labelled and εNd(t) composition graphed in this diagram

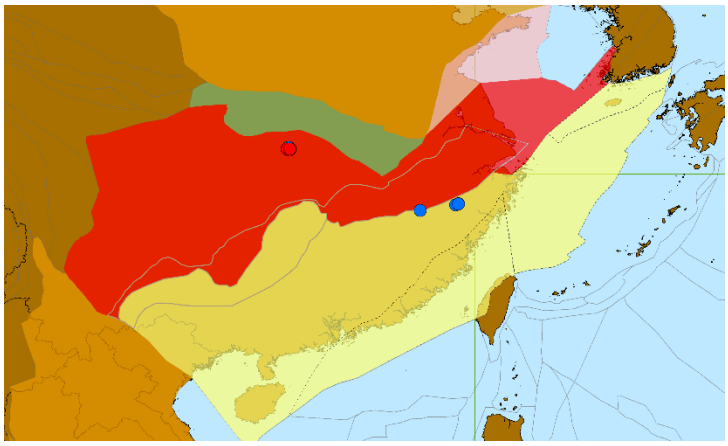

B1. Location of samples from >1000 Ma age group

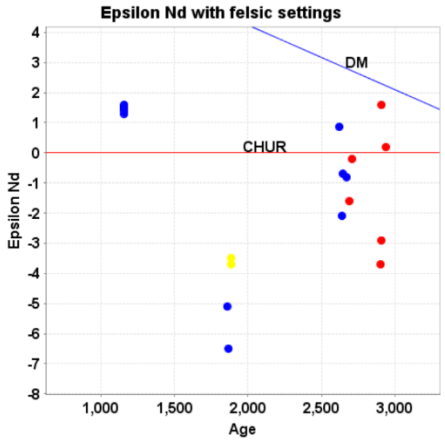

B2. εNd(t) of samples from >1000 Ma

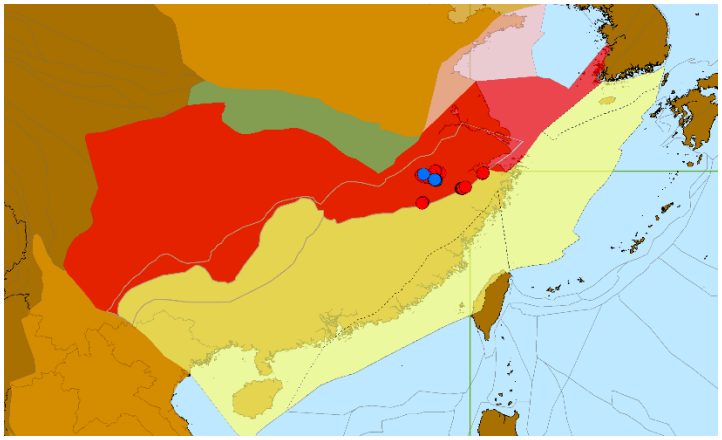

C1. Location of samples from 950-746 Ma age group

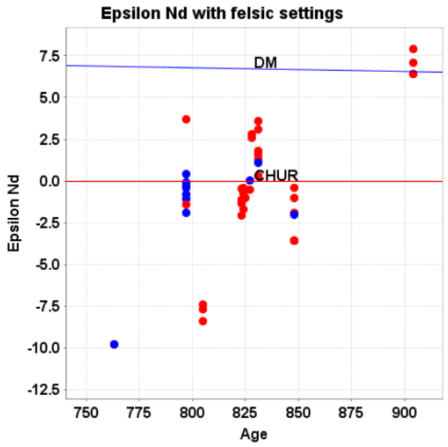

C2. εNd(t) of samples from 950-746 Ma

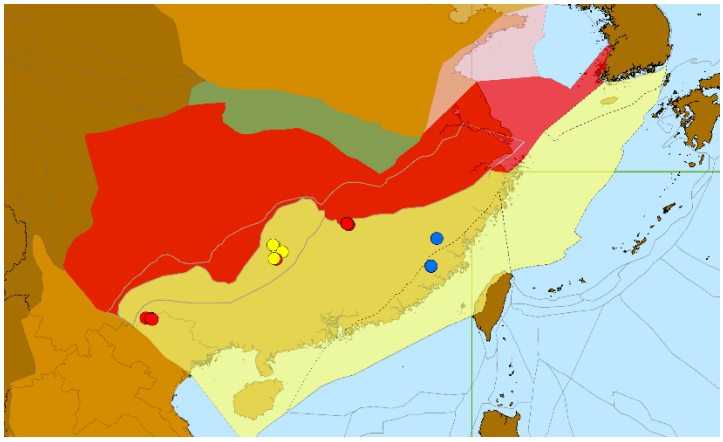

D1. Location of samples from 470-381 Ma age group

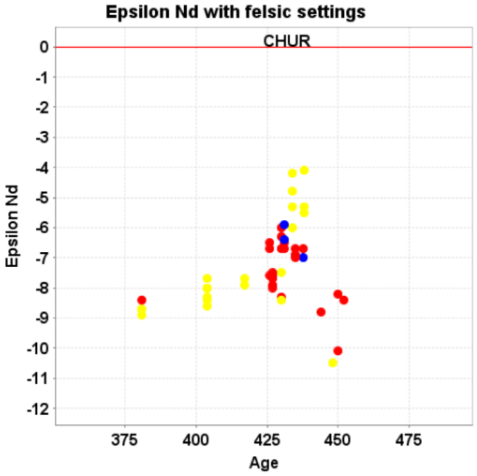

D2. εNd(t) of samples from 470-381 Ma

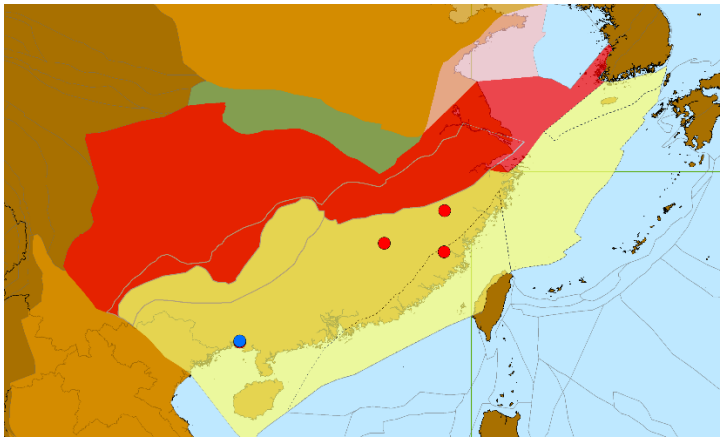

E1. Location of samples from 280-181 Ma age group

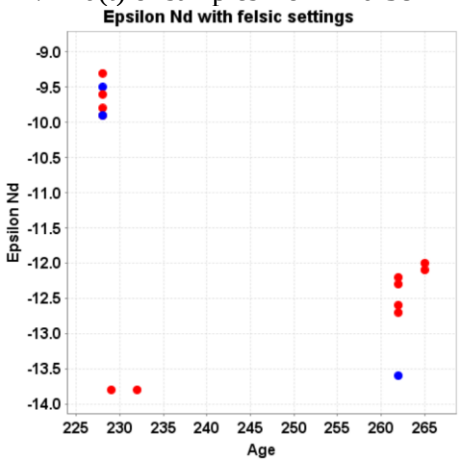

E2. εNd(t) of samples from 280-181 Ma

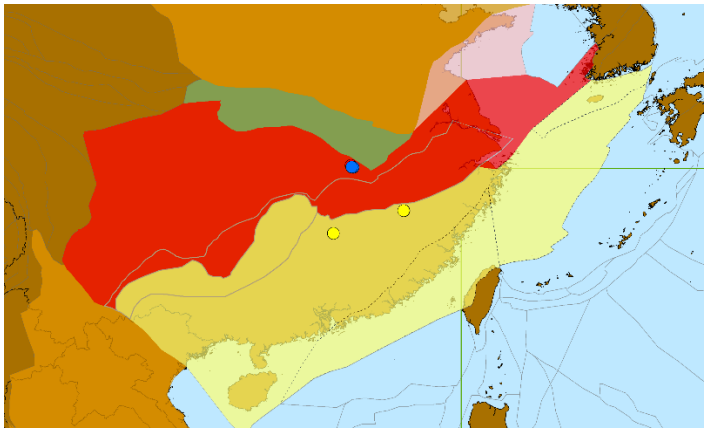

F1. Location of samples from 180-115 Ma age group

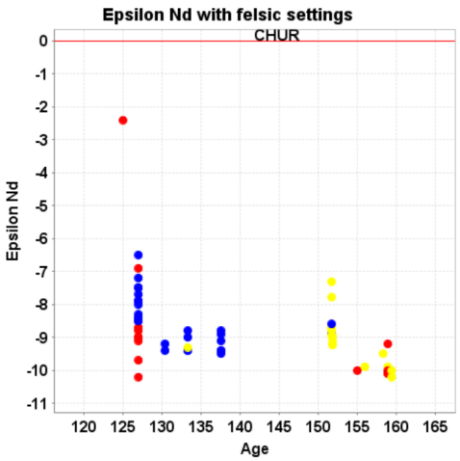

F2. εNd(t) of samples from 180-115 Ma

Figure 3.7 Sm-Nd isotope compositions and interpreted tectonic settings for felsic igneous rocks (without post-collisional settings).

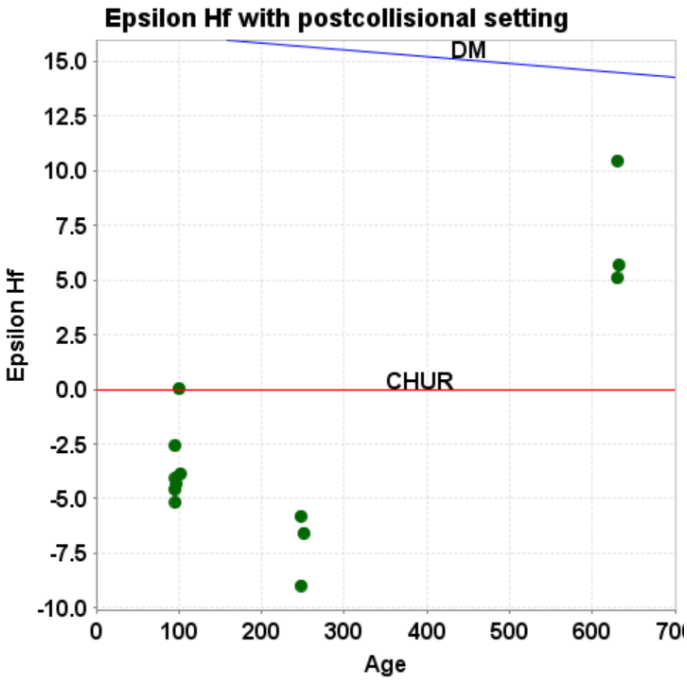

A. Post-collisional samples with Lu-Hf isotope composition

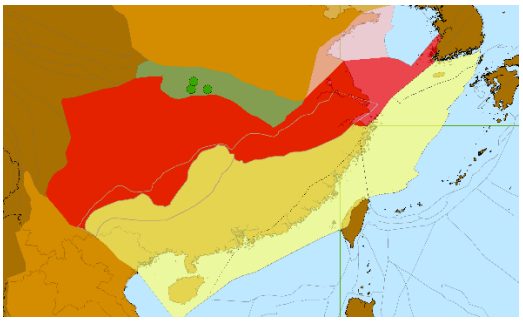

B. Location of samples from 745-551 Ma age group

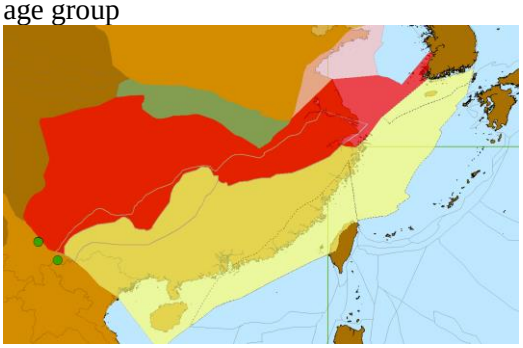

C. Location of samples from 280-181 Ma age group

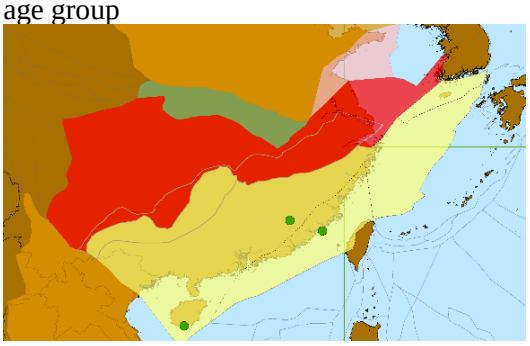

D. Location of samples from 114-0 Ma age group

Figure 3.8 Lu-Hf isotope compositions for felsic igneous rocks interpreted to have formed in post-collisional settings.

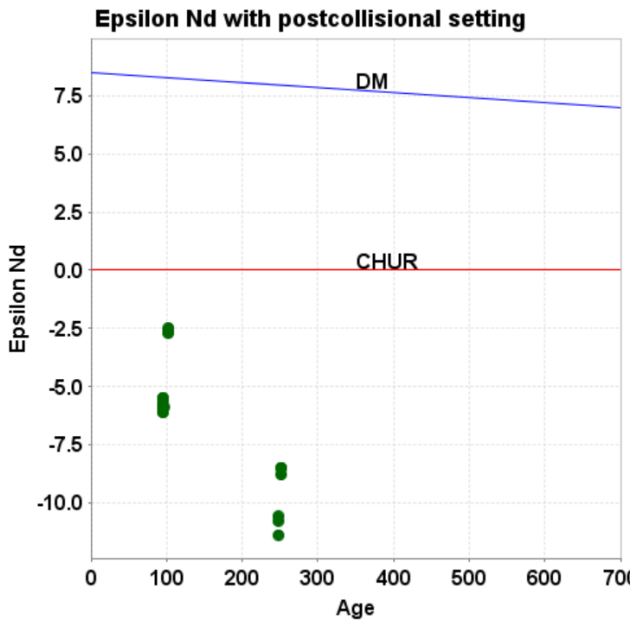

A. Post-collisional samples with Sm-Nd isotope composition

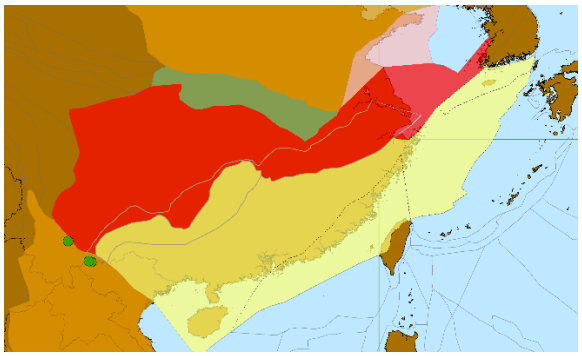

B. Location of samples from 280-181 Ma age group

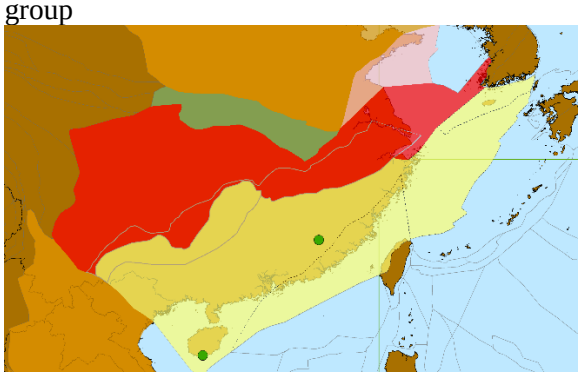

C. Location of samples from 114-0 Ma age group

Figure 3.9 Sm-Nd isotope compositions for felsic igneous rocks interpreted to have formed in post-collisional settings.

For post-collisional felsic samples, the Lu-Hf isotope data (Figure 3.8) show that only 700-600 Ma samples have a juvenile provenance. No Sm-Nd data (Figure 3.9) are available for the 700-600 Ma samples. Younger samples all have negative epsilon values, indicating that they are derived from much older protoliths.

In short, felsic igneous rocks shows very juvenile volcanic arc settings only in 950-746 Ma age group.

3.3.2 Mafic rocks

Mafic or basaltic rocks were classified using the graphs in Figure 3.10. This diagram shows two version of the same plot. Figure 3.10A clearly distinguishes between arc and mid ocean ridge settings, but does not emphasis the distinction between oceanic (more juvenile) and continental arcs, as is done in Figure 3.10B. Many samples plot outside the fields for continental and oceanic arcs and for the mantle array. Therefore, in this study we further separated the two types of arc and three types of mantle lithology using

the Nb/Yb value. Samples above the mantle array with Nb/Yb <1 are classified as oceanic arcs, while samples with Nb/Yb value between 1 and 3 are classified as mixed type arcs and samples Nb/Yb >3 are all considered as being from continental arcs. Nb/Yb values are also used to separate the MORB settings in the mantle array. Samples inside the array are separated to N-MORB (Nb/Yb<1), E-MORB (1<Nb/Yb<10) and OIB (Nb/Yb>10). Basaltic rock tectonic setting discrimination results were combined with the Lu-Hf and Sm-Nd isotope data and plotted in Figure 3.11 and Figure 3.12.

A.

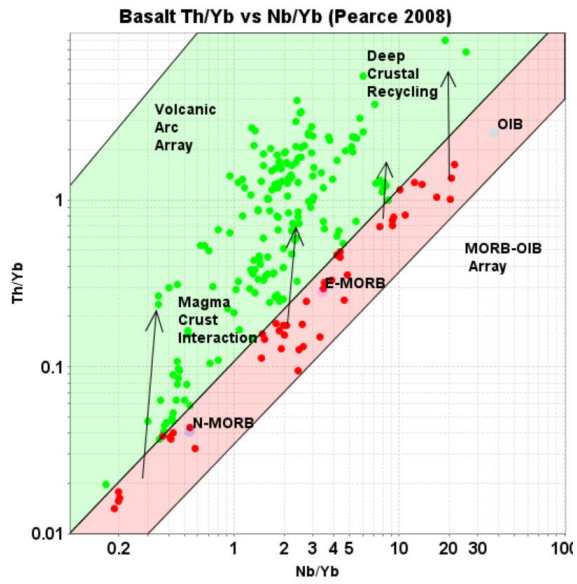

B.

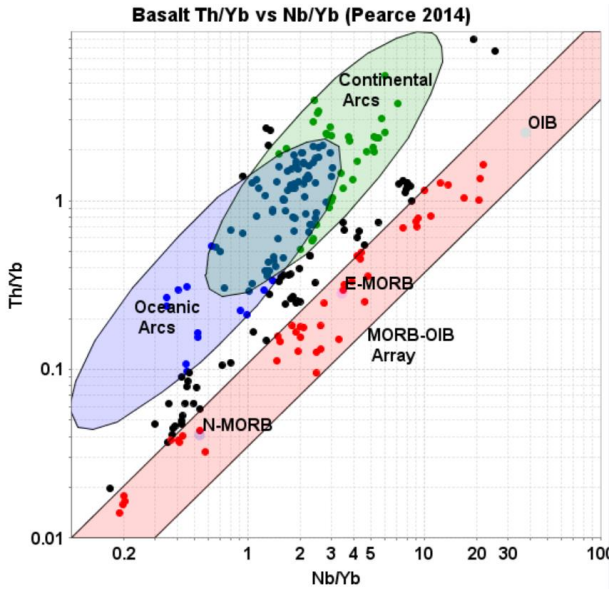

Figure 3.10 The tectonic settings discrimination diagrams for basaltic rocks produced using ioGAS

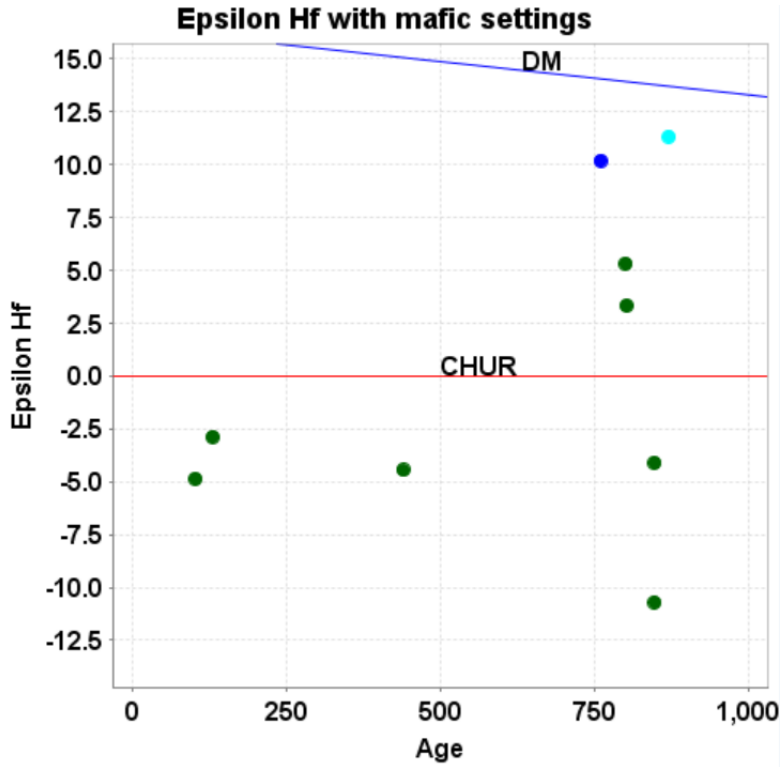

Legend

- Continentalarc
- Mixarc
- Oceanarc
- N-MORB
- E-MORB
- OIB

A. Mafic samples with Lu-Hf isotope data, tectonic settings labelled and εHf(t) composition graphed in this diagram

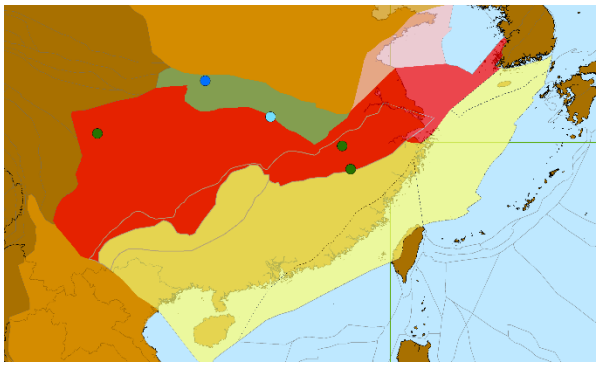

B. Location of samples from 950-746 Ma age group

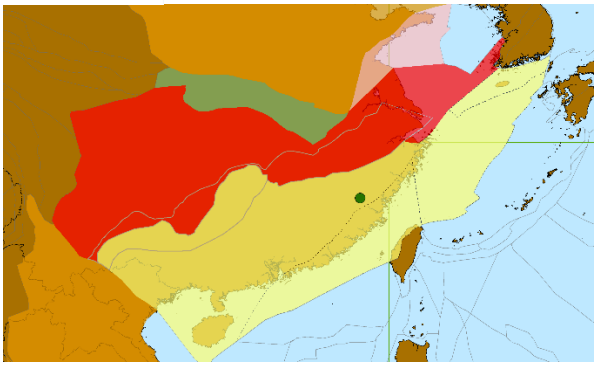

C. Location of samples from 470-381 Ma age group

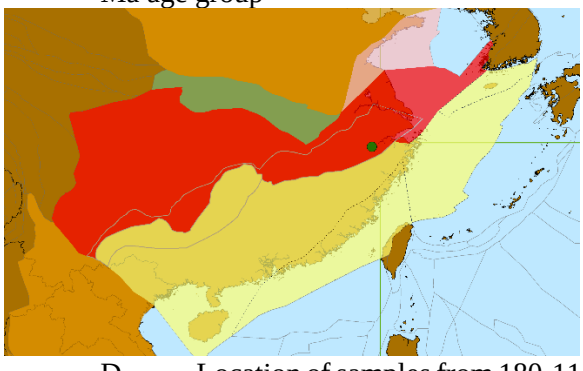

D. Location of samples from 180-115 Ma age group

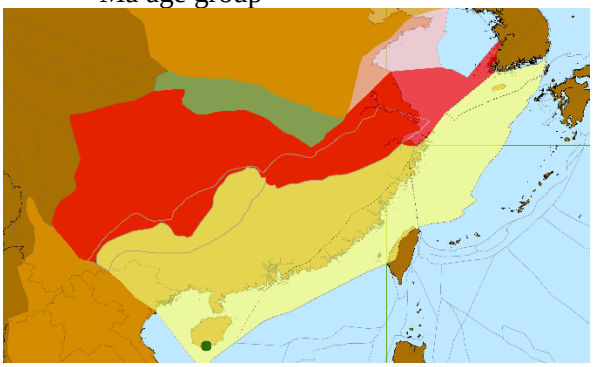

E. Location of samples from 114-0 Ma age group

Figure 3.11 Lu-Hf isotope compositions and interpreted tectonic settings for mafic igneous rocks.

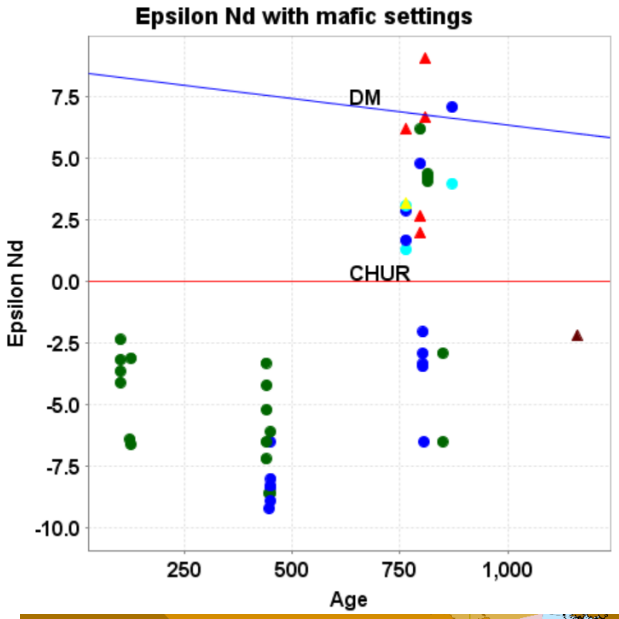

legend

Continentalarc
Mixarc
Oceanarc
N-MORB
E-MORB
OIB

A. Mafic samples with Sm-Nd isotope data, tectonic settings labelled and εNd(t) composition graphed in this diagram

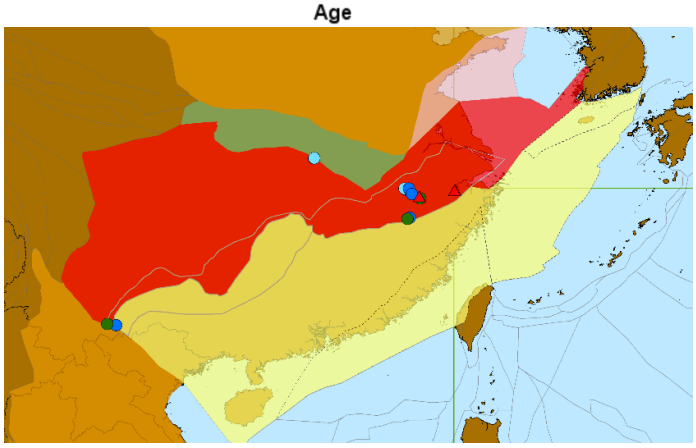

B1. Location of samples from 950-746 Ma age group

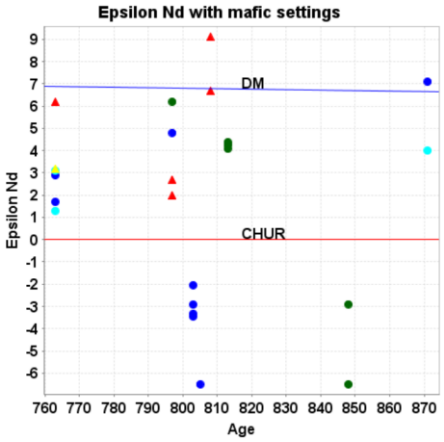

B2. εNd(t) of samples from 950-746 Ma

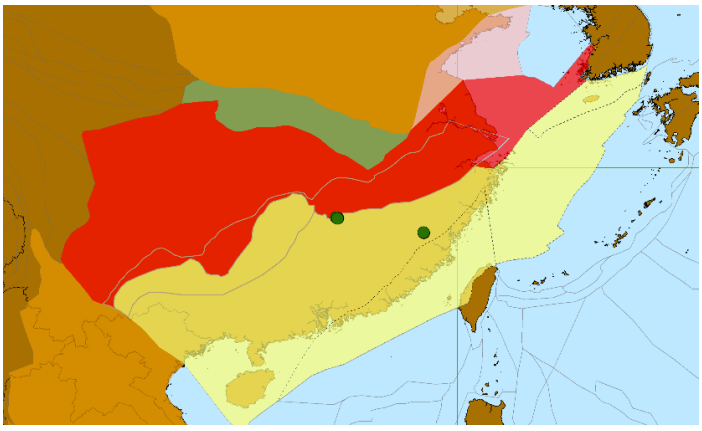

C1. Location of samples from 470-381 Ma age group

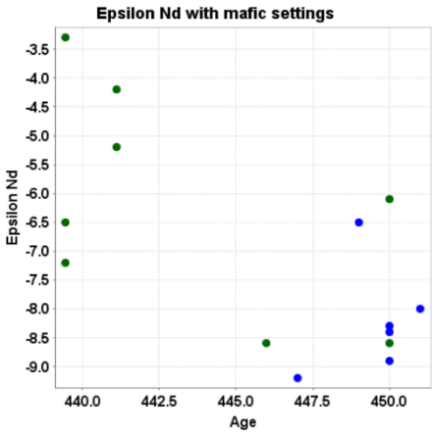

C2. εNd(t) of samples from 470-381 Ma

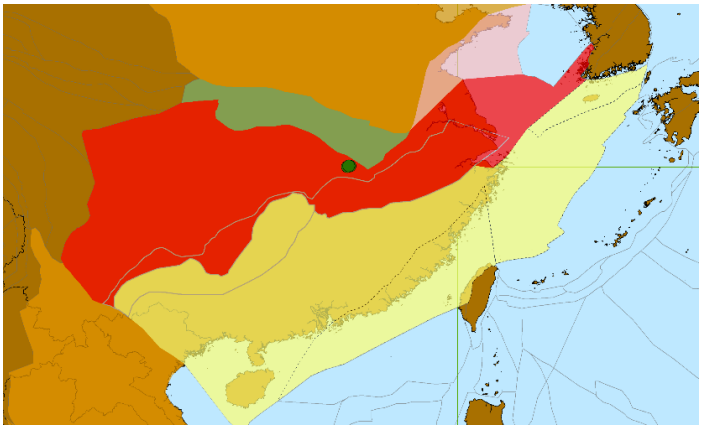

D1. Location of samples from 180-115 Ma age group

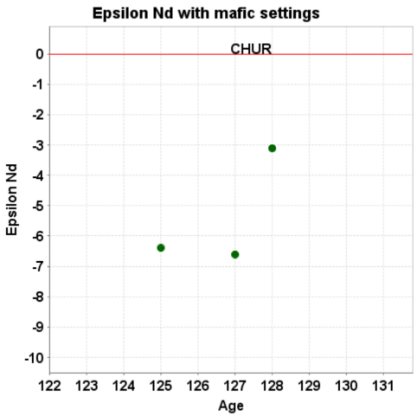

D2. εNd(t) of samples from 180-115 Ma

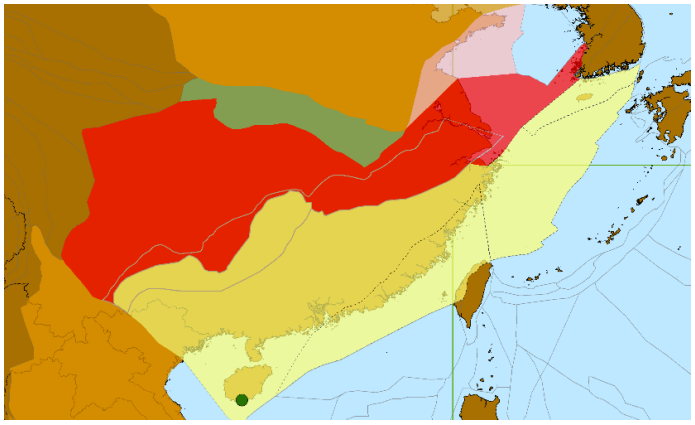

E1. Location of samples from 114-0 Ma age group

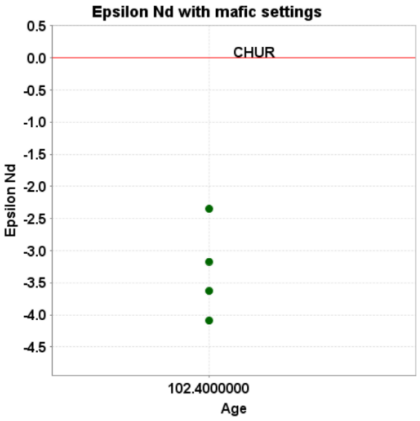

E2. εNd(t) of samples from 114-0 Ma

Figure 3.12 Sm-Nd isotope compositions and interpreted tectonic settings for mafic igneous rocks.

From Figure 3.11 and Figure 3.12, we can see that both Lu-Hf and Sm-Nd isotope systems for mafic samples show similar results. In the 950-746 Ma age group, sample protoliths were from both juvenile and older provenance. Most samples from this age interval came from the Yangtze block side of the Jiangnan Orogen. MORB and oceanic arc type of tectonic settings were also only seen in the 950-746 Ma age group. The rest of the age intervals in both isotope systems are interpreted to be only from old protoliths and mixed or continental arc settings.

To sum up, the results from the lithochemical data agree with geochronology and isotope geochemical implications that the Yangtze and Cathaysia blocks started to interact during the 950-746 Ma age interval and that subduction was likely to have happened near the Jiangnan Orogen, creating many units with volcanic arc type chemical signature on the Yangtze block side of the orogen.

CHAPTER 4
METAMORPHISM AND TECTONIC IMPLICATIONS

Metamorphic geochronology data can be used as an indication of collision time between blocks and as a comparison with sedimentary data to study the potential source region of the rocks. As mentioned in Chapter 2, metamorphic geochronology data of this thesis are from U-Pb dating of zircon and monazite and no titanite data are available. These data most closely represent the age of peak metamorphism of the samples. The analytical results of the metamorphic zircon and monazite can be seen in Figure 4.1A. To show the details of the younger age groups and to focus on the age intervals most important for this study, one peak around 2000 Ma with only 5 percent of probability was not shown in the probability curve of Figure 4.1A. The remaining four peaks were coloured, and these colours are linked to sample locality on the location map (Figure 4.1B).

Metamorphic data results are shown as follow:

1. The ~800 Ma age group only yielded one date; therefore, not enough data are applicable for this age.
2. The 479-389 Ma age group could be related to ~400 Ma igneous activities in the SCB, as suggested in Chapter 3, possibly representing the collision of the SCB with other blocks at this age
3. The 271-171 Ma age group samples in the Sulu block area are mostly for eclogite grade metamorphism which is related to the collision of the NCB and the SCB (Li et al., 2017; Schmidt et al., 2011; Wang et al., 2014).
4. Only two samples occur for the 169-140 Ma age group, one in the Sulu block and the other near the southern margin of the SCB. It is possible that the latter sample might be related to interaction of the Tolo block with the Cathaysia block (Sewell et al., 2016).

In general, the metamorphic data matched the Ordovician to Silurian magmatism in the Cathaysia block and ~220 Ma high pressure (eclogite) metamorphism associated with SCB-NCB collision (Schmidt et al., 2011). The Paleozoic metamorphism is consistent with uplift and inversion of parts of the Cathaysia block. There is no evidence for significant metamorphism in the Yangtze block during the Paleozoic event.

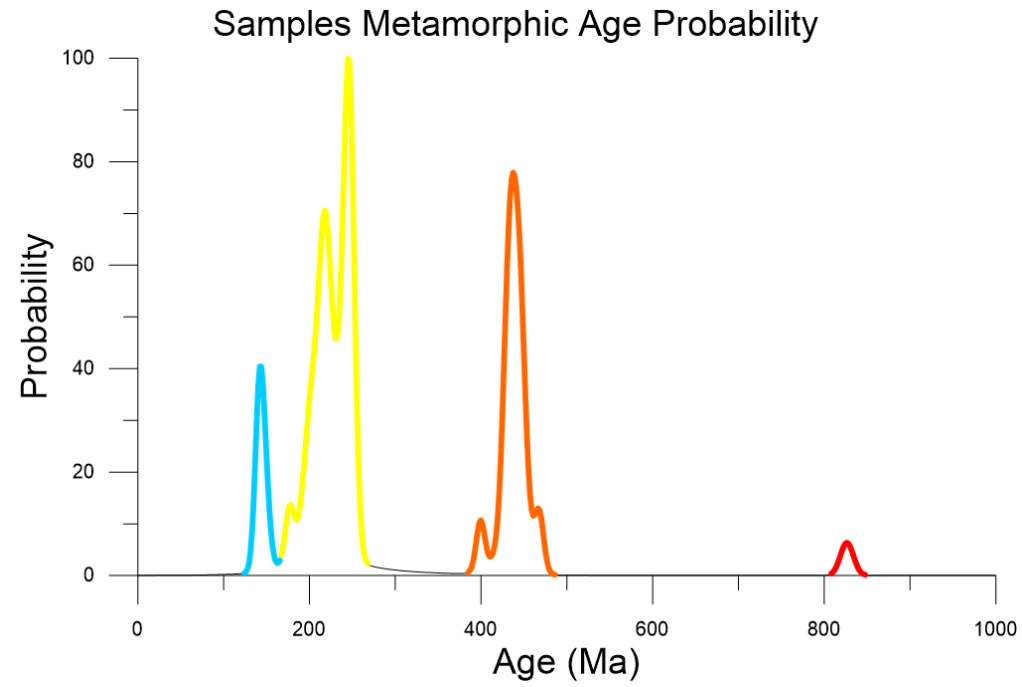

A.

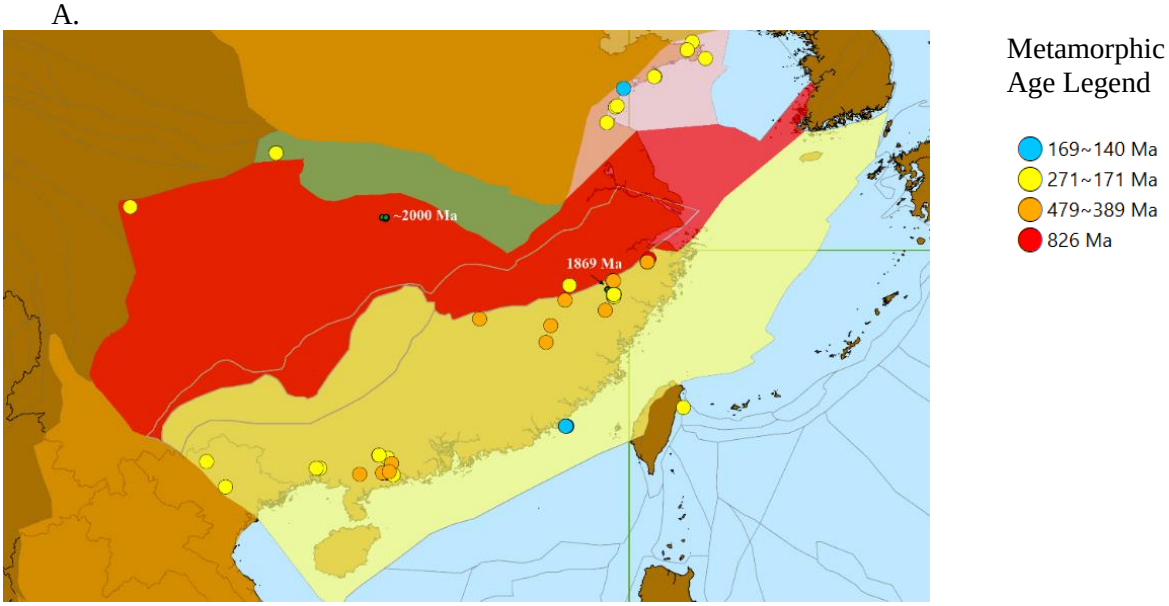

B.

Figure 4.1 A. Metamorphic age probability curve (Gaussian 'AND' summation); B. Location of the grouped metamorphic samples

CHAPTER 5
DETRITAL ZIRCON RECORDS AND THEIR POSSIBLE TECTONIC IMPLICATION

5.1 Geotectonic events suggested by detrital zircon data

As mentioned in Chapter 2, detrital zircon geochronology data for the SCB can be used to infer areas in which erosion was occurring, complementing the igneous and metamorphic data presented in Chapter 3 and Chapter 4.

Detrital zircon U-Pb data probabilities are plotted relative to deposition age in Figure 5.1A. The age probability distribution for all samples (less than 10% discordant) is shown in Figure 5.1B, together with the age probability distribution for analysis with Th/U less than 0.1. Samples with such low Th/U are thought to have formed during metamorphism (Hoskin and Schaltegger, 2003; Rubatto, 2017; Yakymchuk et al., 2018) and therefore these diagrams show the age intervals in which metamorphism occurred in the provenance regions of the detrital samples. Blue triangles in Figure 5.1A show where these metamorphic grains occur in the deposition record. The three most important age intervals for original formation of the detrital zircons from the SCB are: 900-700 Ma, 500-400 Ma and 300-200 Ma.

Detrital grains with low Th/U at ~430 Ma and ~250 Ma plot almost on the diagonal black line in Figure 5.1, indicating that they were eroded and deposited almost immediately after formation. Since metamorphism almost always occurs at depth in the crust, this requires a lot of erosion. One can correlate the ~250 Ma metamorphic grains with collision of the SCB and NCB in the Sulu block resulting in rapid exhumation of eclogitic lithologies (Li et al., 2017; Schmidt et al., 2011; Wang et al., 2014) but no similar location and setting has been reported for the ~430 Ma metamorphic grains.

Paleogeographic links between continental blocks can be identified by matching detrital zircon age probability curves with igneous and metamorphic activity in potential provenance regions. Figure 5.2 compares the detrital zircon record of the SCB with the igneous and metamorphic record of India, Indochina, China (SCB and NCB combined), Australia and North America.

The probability curve for low Th/U (metamorphic) detrital zircons in Figure 5.1 also has several peaks at 1400-1200 Ma, that does not match known metamorphic activity in the SCB (Figure 5.2), although igneous activity of this age is known from Hainan Island (Yao et al., 2017). Similar aged magmatism occurs across North America (Bickford et al., 2015; Yao et al., 2017; DateView database) although no metamorphic ages have been reported for the age range 1450-1400 Ma.

Most of the Neoproterozoic and Phanerozoic grains in the SCB could be sourced locally. Provenance of Neoproterozoic detrital grains in North America, Australia and Indochina is unlikely but is possible from India. Detrital zircon grains with low Th/U and ages in the range of 650-500 Ma are unlikely to be sourced from within the SCB since no metamorphic activity of this age is known from the region. Rather these grains are likely to have come from India suggested by Yao and Li (Yao and Li, 2016). None of the other continental blocks which were potentially joined to the SCB have this signature. The 500-380 Ma detrital grains cannot come from North America or India but might be sourced in Australia or Indochina. North America, India, and Australia are not suitable sources for the Mesozoic and Cenozoic detrital grains, but Indochina is a possibility.

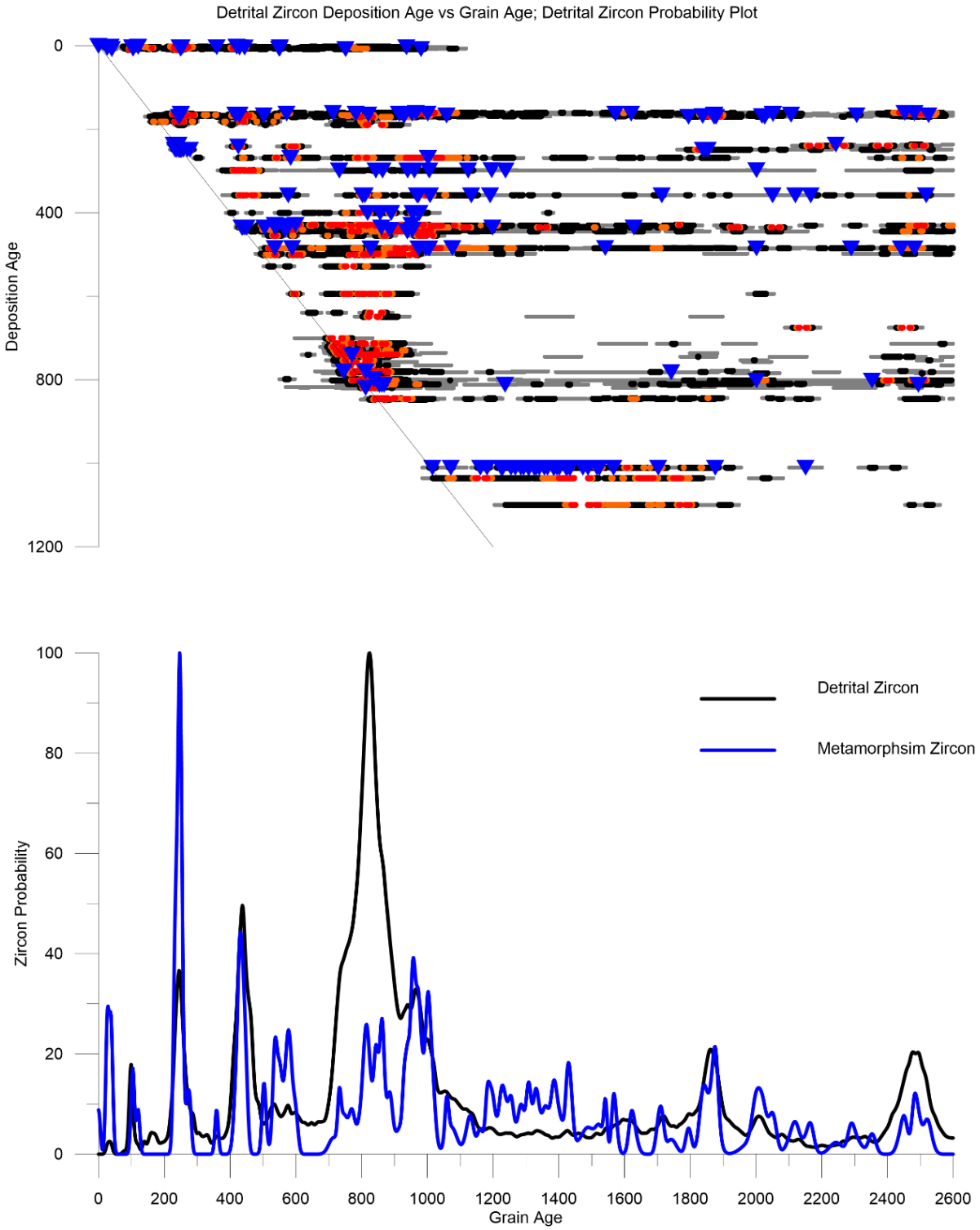

Figure 5.1 *Top:* Detrital zircon grain age vs deposition age graph. Red: detrital zircon crystallization age peak probability 80%-100% of maximum peak height; Orange: detrital zircon crystallization age peak probability 60%-80%; Black: detrital zircon crystallization age peak probability 40%-60%; Grey: detrital zircon crystallization age peak probability 10%-40%; Blue triangle: detrital zircon grains with Th/U value less than 0.1. *Bottom:* Zircon grain age probability graph (Gaussian 'AND' summation). Black: all grains; Blue: assumed metamorphic ages for grains with Th/U value less than 0.1.

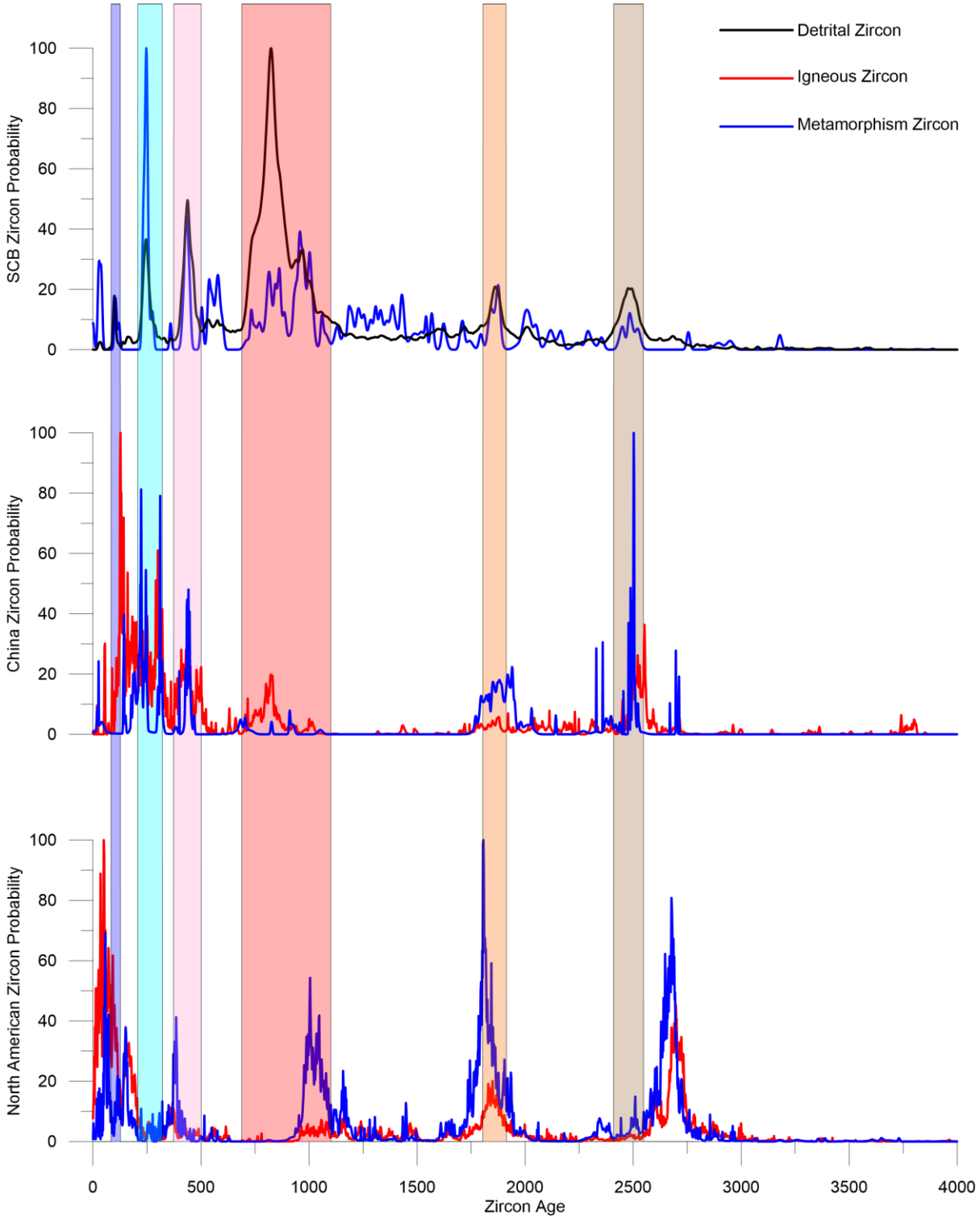

A. SCB detrital zircon age probability vs China and other continental blocks (part 1)

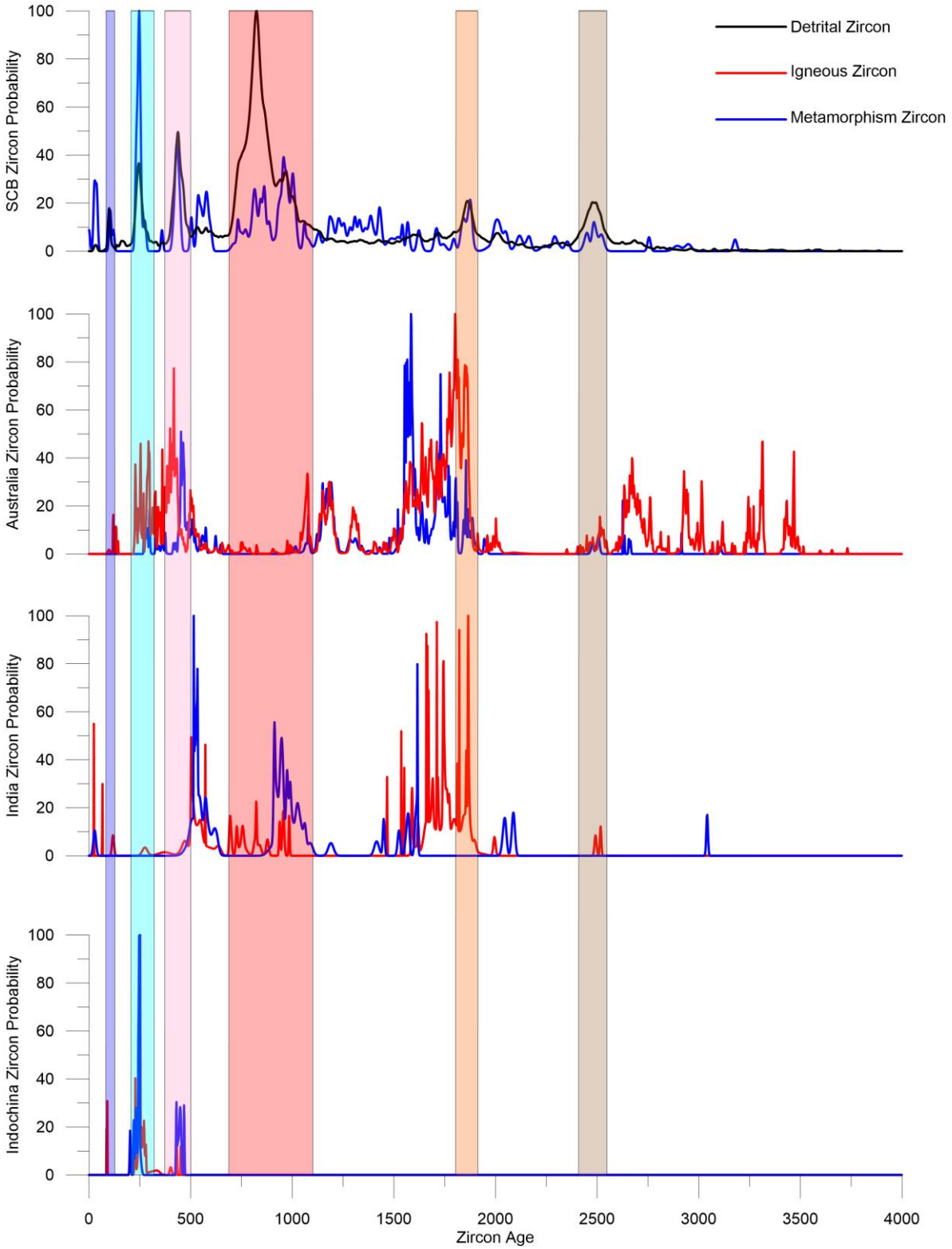

B. SCB detrital probability distributions vs other continental blocks (part 2)

Figure 5.2 Detrital Zircon in SCB vs igneous zircon and metamorphic zircon from China and other continental blocks (Gaussian 'AND' summation). Data from the DateView database.

5.2 Detrital zircon Lu-Hf isotope study

Lu-Hf data from the detrital zircons can help with the understanding of the source regions. Figure 5.3 shows the grain age vs deposition age distribution of juvenile (light blue) and reworked old (green) protolith sources for detrital zircon samples with Lu-Hf isotope data compiled for this thesis. Light blue diamonds symbolize grains with εHf>12, mostly seen in ~800 Ma detrital zircons. Green diamond symbols show grains with εHf<-10 and are seen in detrital grains formed and deposited at almost all ages. Together, these graphs show that ~800 Ma detritus was sourced from multiple protoliths, both juvenile and reworked. Since only ~800 Ma sediments contain grains from juvenile sources, the detrital zircon data supports the assumption that the SCB was assembled at ~800 Ma, not during the Paleozoic.

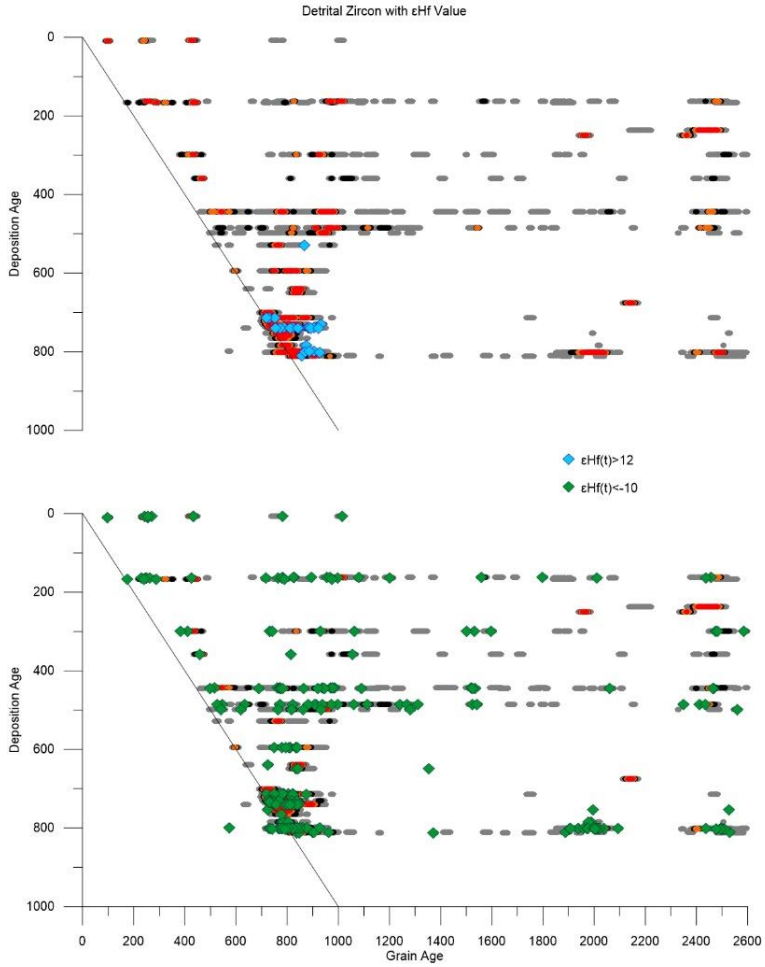

Figure 5.3 Detrital zircon age and deposition distribution with associated juvenile (top, in light blue) and non-juvenile (bottom, in green) associations inferred from Lu-Hf isotope data. Red: detrital zircon crystallization age peak probability 80%-100% of maximum peak height; Orange: detrital zircon crystallization age peak probability 60%-80%; Black: detrital zircon crystallization age peak probability 40%-60%; Grey: detrital zircon crystallization age peak probability 10%-40%

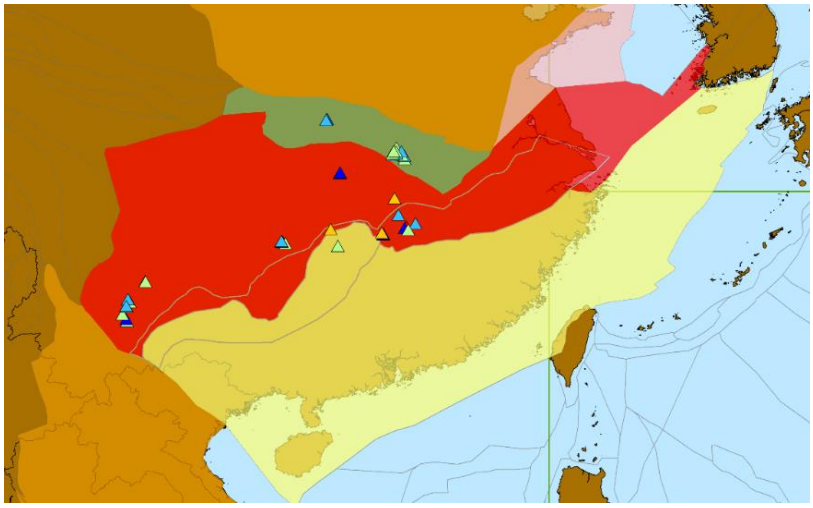

εHf value legend (colour range matches that used for εNd graphs and maps in Chapter 3)

- -30 - -22
- -22 - -10
- -10 - 1
- 1 - 9
- 9 - 17

A. Deposition ages older than 600 Ma.

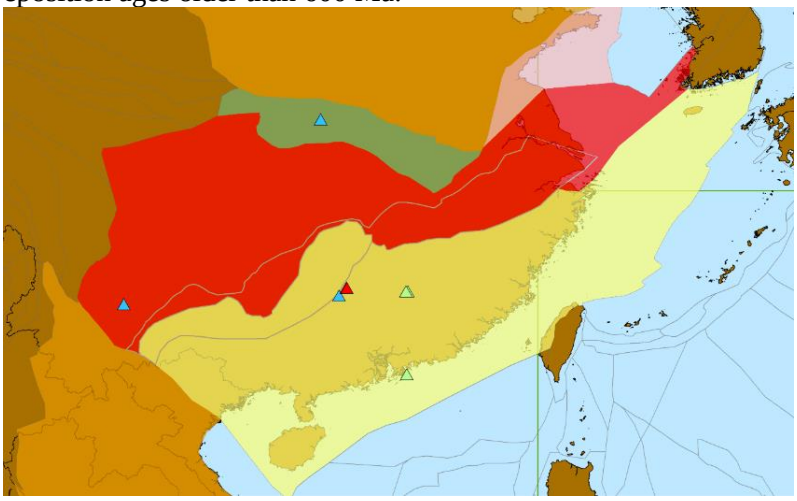

B. Deposition ages from 300 to 600 Ma.

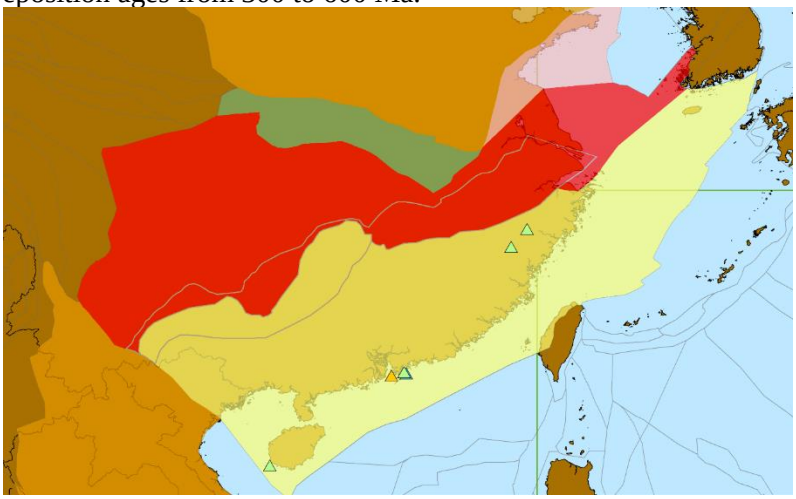

C. Deposition ages from younger than 300 Ma.

Figure 5.4 Deposition locations of detrital zircon samples for various deposition ages, symbolized by εHf value.

The combination of detrital zircon deposition location and epsilon Hf value are shown in Figure 5.4. The colour range used for the epsilon Hf values is the same as used for equivalent epsilon Nd values in Chapter 2 and Chapter 3. We can see that detrital grains with deposition ages older than 600 Ma have very positive εHf values as well as negative values. Only 3 grains with deposition ages younger than 600 Ma have positive epsilon Hf values and the rest have negative values. Based on these results, juvenile sources are almost only seen in the older sediments, deposited before 600 Ma.

5.3 Detrital zircon cumulative probability distributions

The other information provided from the detrital zircon data are the time gaps between the zircon formation and the detritus deposition. Figure 5.5 shows cumulative probability curves for the samples compiled for this thesis. These curves are classified using the method developed by Cawood et al (Cawood et al., 2012). If the time gap between zircon formation and sedimentary deposition is relatively short for most grains in a sample, then the grains must have been rapidly transferred from their igneous formation settings and this is classified as most likely being a convergent setting. On the other hand, when most detrital grains in a sample take a long time from crystallization to deposition, the deposition setting is as a divergent setting. The collisional setting is the condition between the two extremes of convergent and divergent settings.

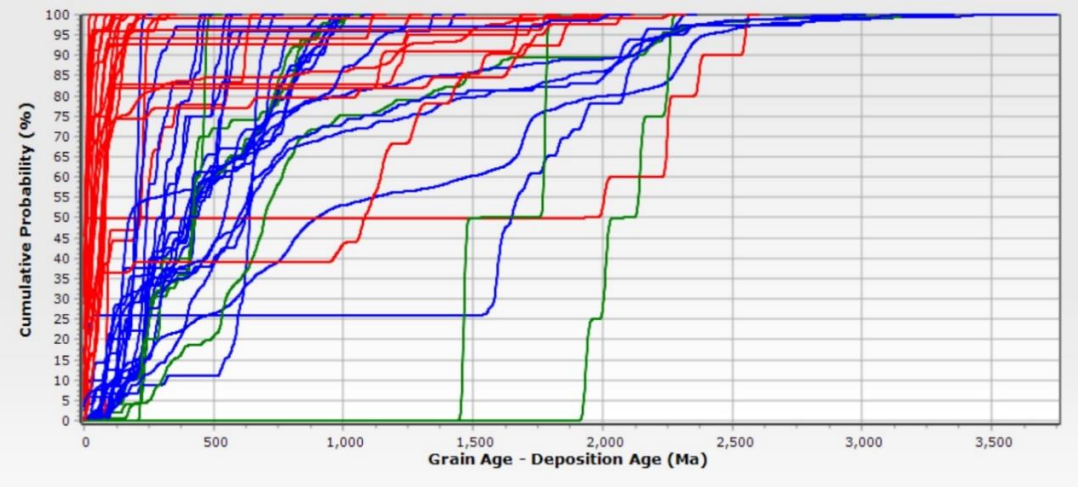

Figure 5.5 Detrital zircon cumulative graph (classification following Cawood et al., 2012). Red = Convergent; Blue = Collision; Green = Extension. Graph generated by FitPDF software.

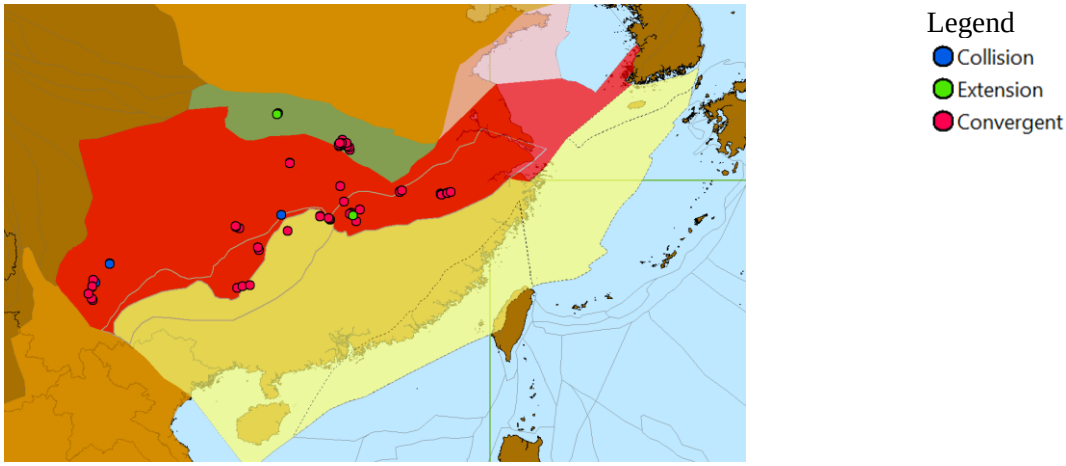

A. Deposition ages between 600 and 1000 Ma.

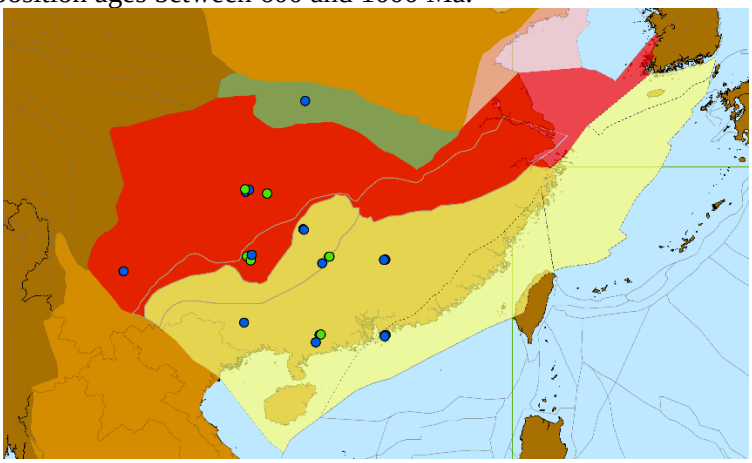

B. Deposition ages between 300 and 600 Ma.

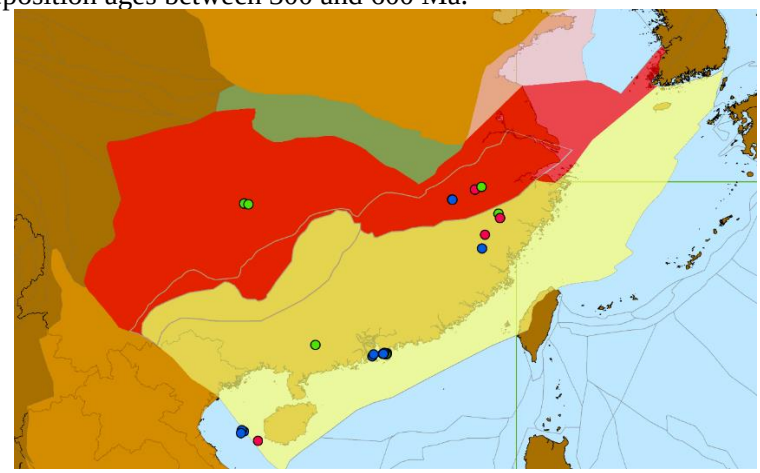

C. Deposition ages younger than 300 Ma.

Figure 5.6 Location of detrital zircon samples and their interpreted depositional settings based on the criteria of Cawood et al (Cawood et al., 2012).

Figure 5.6 maps the distribution of the detrital zircon samples, classified as convergent, extension and collision. From this figure one can see that the detrital zircon samples older than 600 Ma are dominantly

derived from convergent settings while, for the younger detrital zircon samples (between 300 and 600 Ma), no convergent settings are seen. Some samples deposited in this latter age range even show some extensional tectonic settings. No detrital samples with deposition ages in the range 1000 Ma to 600 Ma are available for the Cathaysia block.

CHAPTER 6
DISCUSSION

The previous chapters presented and summarized compiled data for igneous, metamorphic and sedimentary samples. They also summarized the interpretations that could be made from the specific techniques considered, for instance geochronology, isotope geochemistry and lithochemistry. This chapter considers situations where multiple lines of evidence support one consistent interpretation. The chapter also links these interpretations to the regional geodynamic history and plate tectonic setting of the SCB. The development of the SCB is conveniently subdivided into several age intervals.

1. Prior to 900 Ma

The older igneous and metamorphic ages of the SCB are not discussed in detail during this study. The protoliths of the Yangtze and Cathaysia blocks were generated at different ages: ~3.5 Ga and ~3.0 Ga, respectively (Figure 2.3). Maximum crystallization ages for the Yangtze and Cathaysia blocks are ~3.0 Ga and ~1.9 Ga, respectively (Figure 6.1). The pattern of igneous ages for the Yangtze and Cathaysia blocks prior to 900 Ma is different (Figure 6.1), indicating that they didn't have a shared history before 900 Ma. The absence of a shared pre 900 Ma history is not consistent with the interpretation that they rifted apart at about 900 Ma (Li, 2014).

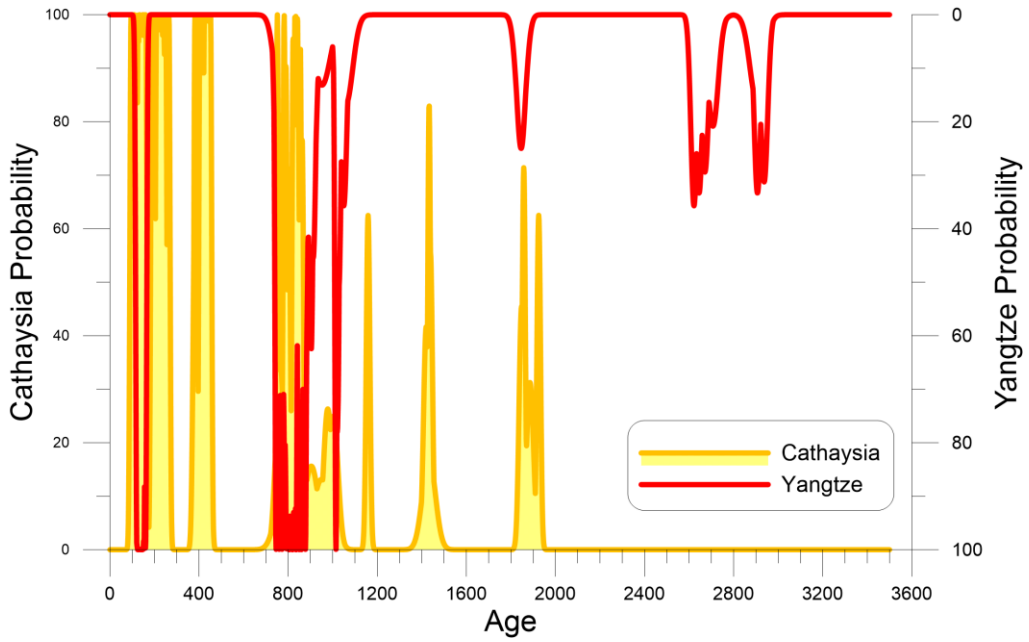

Figure 6.1 Gaussian 'OR' igneous age probability distributions for the Yangtze and Cathaysia blocks, using data form the DateView database.

2. 900~800 Ma

From Figure 6.2 and Figure 6.3 one can infer that, unlike the amalgamation times of 1000-900 Ma and ~400 Ma suggest by Li or Hsü, respectively (Hsü et al., 1990; Li et al., 2008), data from this study indicate that the amalgamation of the Yangtze and Cathaysia blocks most likely occurred at around 900-820 Ma. There is also disagreement with previous suggestions of the process of the amalgamation (Xia et al., 2015; Zhang et al., 2013; Zhang et al., 2015b). In this study, igneous activity occurs for at least 100 million years (from ~900 Ma to ~780 Ma) on the eastern margin of the Yangtze block (Figure 6.2), suggesting that the Yangtze block was in an upper plate setting throughout this time. Geochemical interpretations of tectonic settings for the igneous rocks formed at this time are consistent with mostly volcanic arc environments and both Sm-Nd and Lu-Hf isotope signatures support juvenile crust formation (Figure 6.3). A few samples are classified as coming from a within plate extensional settings but, since the majority have volcanic arc characteristics, there is no reason to infer an overall extensional setting. Detrital zircon data for sediments deposited at about 800 Ma show very juvenile Lu-Hf isotope compositions (Figure 6.4), consistent with this interpretation.

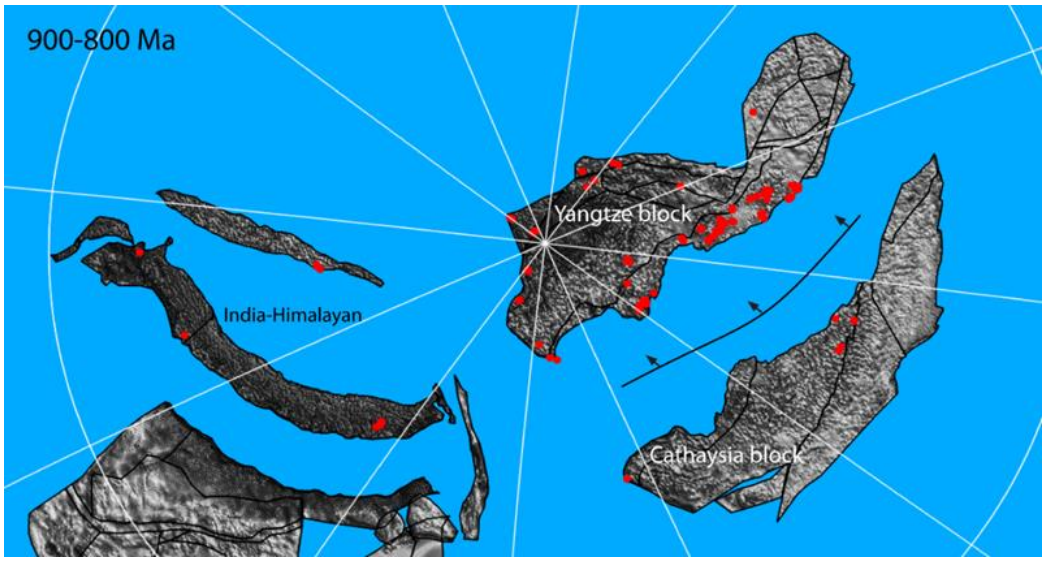

Figure 6.2 Yangtze block and Cathaysia block reconstruction at 820 Ma showing igneous activity from 900-800 Ma. Reconstruction performed using the PalaeoPlates model and GPlates software. Igneous geochronological data from the DateView database.

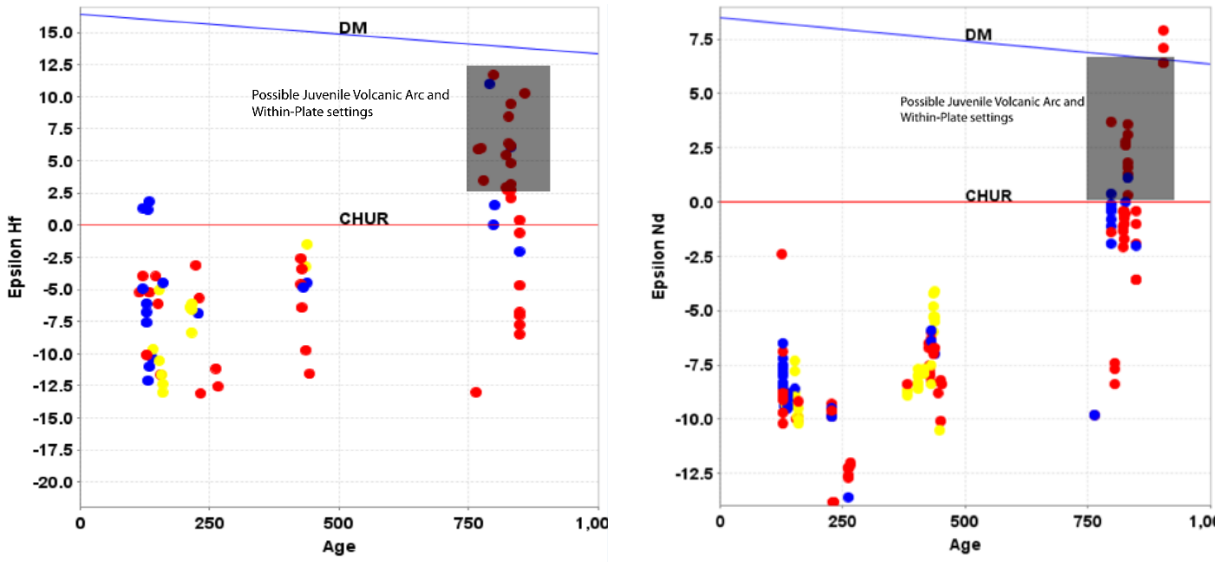

A. B.

Figure 6.3 Sm-Nd and Lu-Hf isotope geochemistry for igneous rocks from the SCB. Symbol colours represent interpreted geotectonic settings based on rock geochemsitry (Pearce et al., 1984; Pearce, 1996b). Red: volcanic arc; blue: within plate; yellow syn-collision.

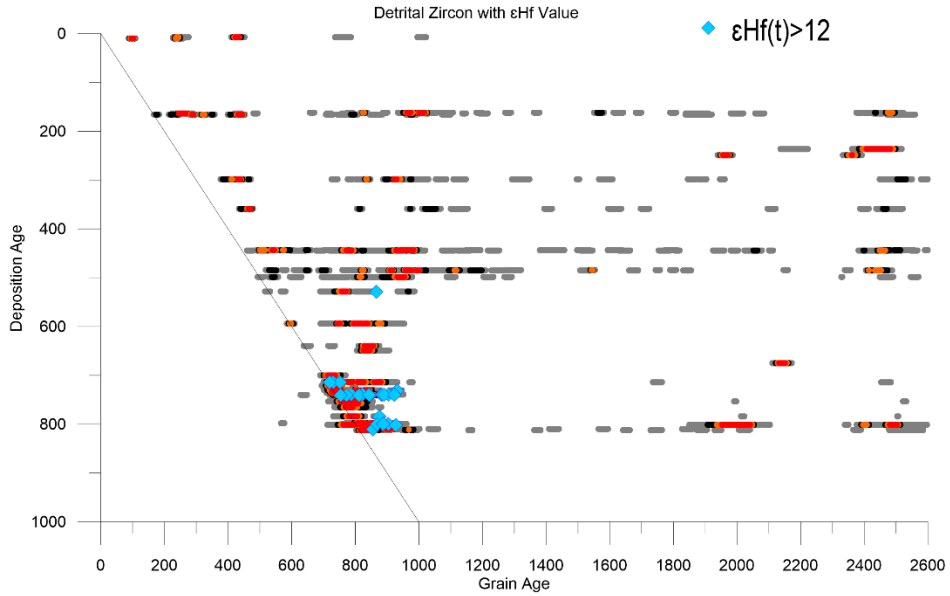

Figure 6.4 Grain age vs deposition age graph of detrital zircon age probability distributions for samples from the SCB. Light blue symbols are for detrital analyses with epsilon Hf values grater than 12. Graph produced using the FitPDF software and data from the DateView database.

It has been suggested that the Rodinia supercontinent, which formed between 1100 Ma and 950 Ma (Li et al., 2008), did not contain many volcanic arcs (Liu et al., 2017). Rodinia is generally considered

to have broken up at about 750 Ma (Li et al., 2008). The SCB exhibits extensive volcanic arc igneous activities between 900 and 800 Ma without significant 1100-950 Ma magmatism. It is therefore possible that the SCB was not part of the Rodinia supercontinent, so the interpretation of Liu et al (Liu et al., 2017) may not be directly relevant to the SCB.

3. 440~380 Ma

Data compiled for this study do not support models involving amalgamation of the SCB in the age interval from 440-380 Ma. No juvenile isotope signatures are evident in igneous or sedimentary rocks from this age and many of the igneous rocks show syn-collisional geotectonic associations (Figure 6.3 and Figure 6.4), consistent with reworking of older basement. Igneous and metamorphic activity was mostly concentrated in the Cathaysia block (Figure 6.5), associated with structural inversion (Yao and Li, 2016), hence the syn-collisional signature. In contrast to Yao (Yao and Li, 2016), who linked the structural inversion to collision with Greater India, recent paleomagnetic constraints make it more likely that the SCB collided with proto-Australia at this time (Zhang et al., 2015a), as illustrated in Figure 6.5.

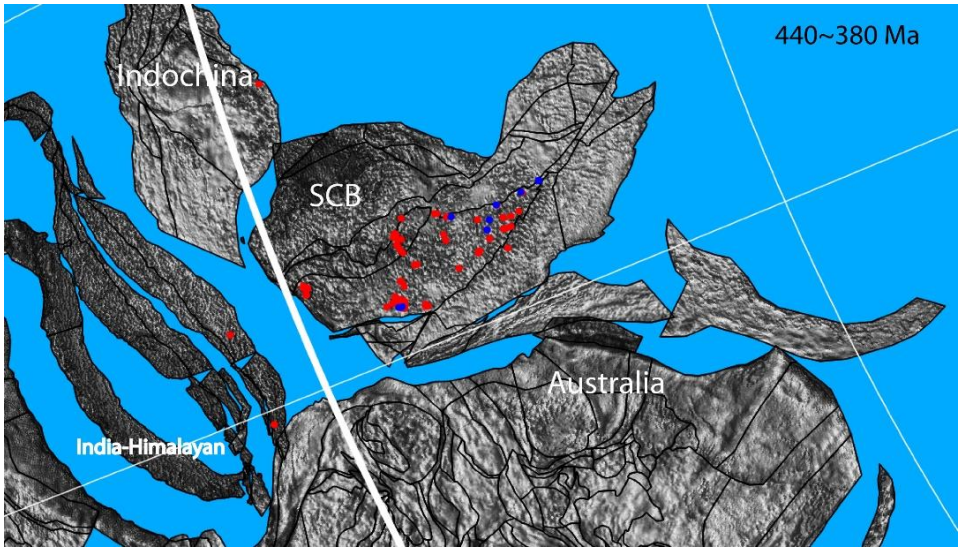

Figure 6.5 SCB reconstruction at 380 Ma showing igneous and metamorphic activity from 440-380 Ma. Reconstruction performed using the PalaeoPlates model and GPlates software. Igneous geochronological data from the DateView database.

4. 220- 200 Ma

The North China block collided with the South China block at about 220 Ma (Enkin et al., 1992), with high pressure metamorphism in the Sulu block (Schmidt et al., 2011) (Figure 6.7). Rapid exhumation

of eclogites formed during the collision resulted in deposition of metamorphic detrital zircon grains very soon after the collision (Figure 6.6). Sm-Nd and Lu-Hf isotope signatures for igneous rocks of this age show that they formed by reworking of older crust (Figure 6.3).

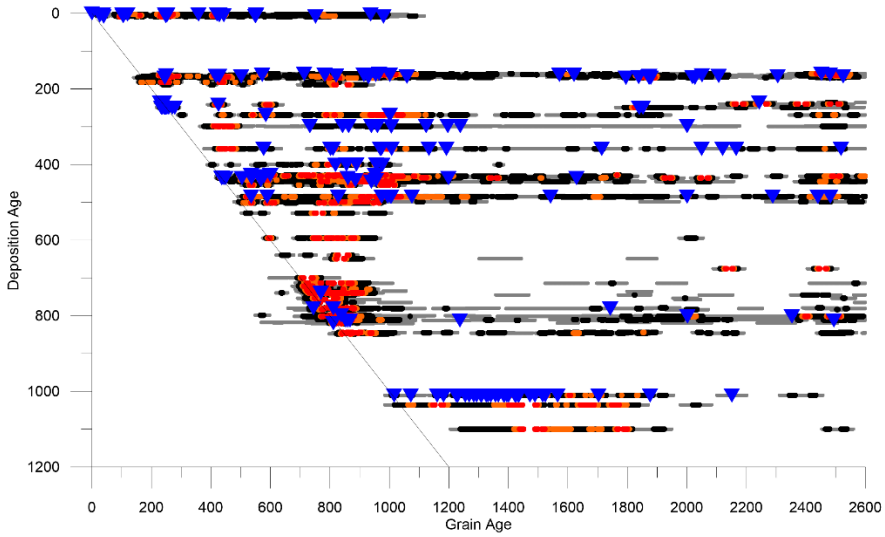

Figure 6.6 Detrital zircon grain age vs deposition age probability plot, showing the distribution of low Th/U grains, assumed to be metamorphic in origin. Graph produced using the FitPDF software and data from the DateView database.

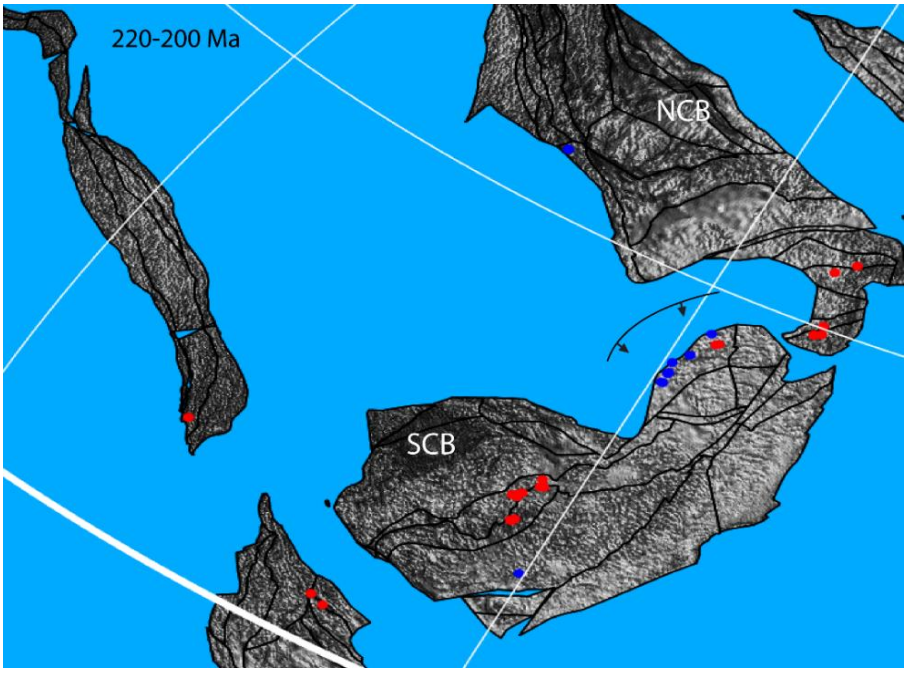

Figure 6.7 SCB reconstruction at 215 Ma showing igneous and metamorphic activity from 220-200 Ma. Reconstruction performed using the PalaeoPlates model and GPlates software. Igneous geochronological data from the DateView database.

5. 160-150 Ma

The Tolo block is thought to have collided with the rest of Cathaysia at ~160 Ma (Sewell et al., 2016) but the distribution of igneous activity at this time (Figure 6.8) does not show any obvious link to the margins of the block. It is therefore assumed that there was no major collision and that the tectonic boundary between the Cathaysia and Tolo blocks is mostly due to lateral shearing.

Recent research in the Korean peninsula identified changes in location of igneous activity thought to indicate a advancing subduction process from about 200 Ma to about 150 Ma (Wang et al., 2018).

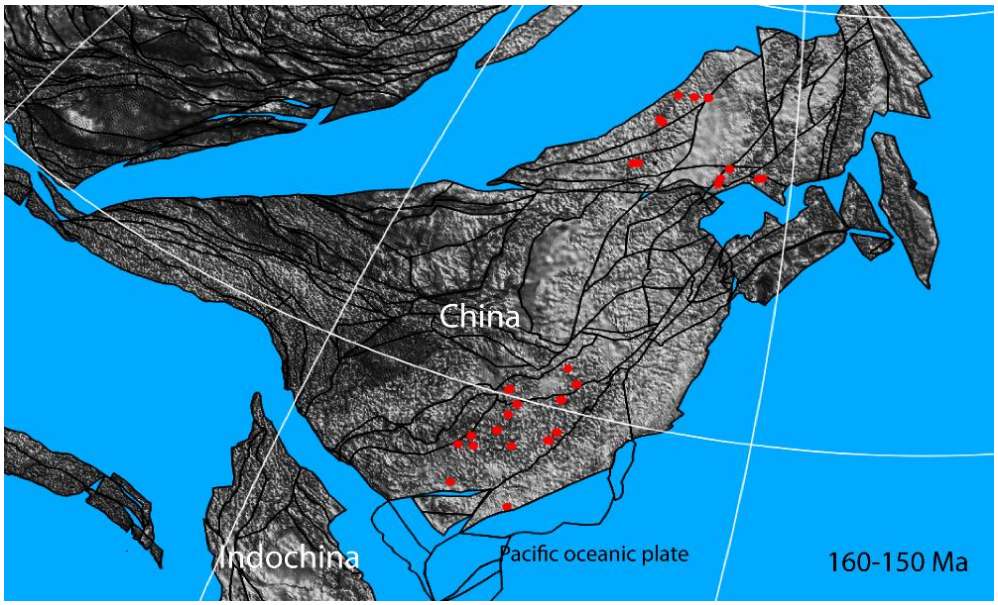

Figure 6.8 SCB reconstruction at 155 Ma showing igneous activity from 160-150 Ma. Reconstruction performed using the PalaeoPlates model and GPlates software. Igneous geochronological data from the DateView database.

6. 150-0 Ma

During this age interval, the Pacific oceanic plate continued to subduct under the SCB resulting in many igneous intrusions (Figure 6.9). Wang's research in the Korean peninsula identified a reverse in the location of younging for intrusions, interpreted to indicate a roll back of the subduction process from about 150 Ma to 60 Ma (Wang et al., 2018).

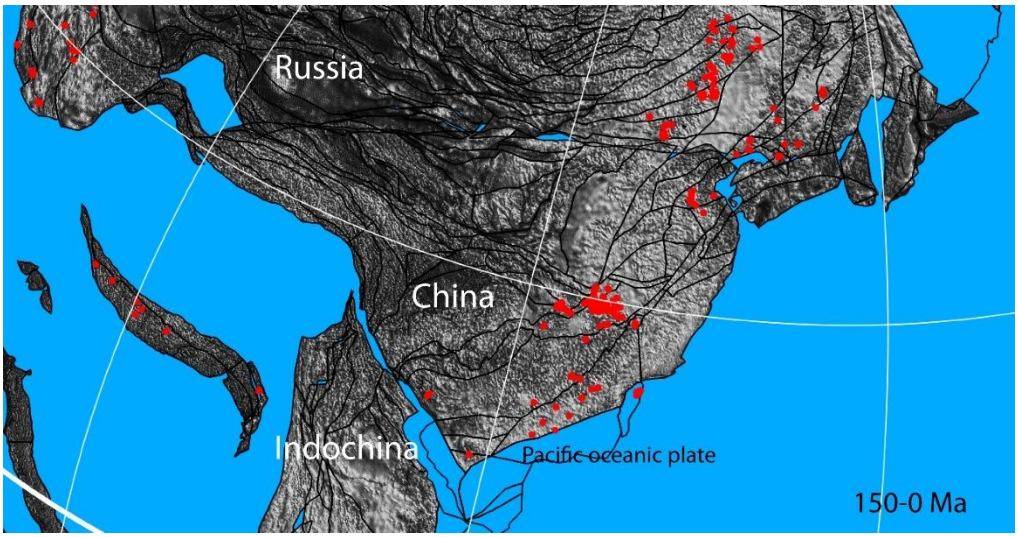

Figure 6.9 SCB reconstruction at 60 Ma showing igneous activity from 150-0 Ma. Reconstruction performed using the PalaeoPlates model and GPlates software. Igneous geochronological data from the DateView database

CHAPTER 7
CONCLUSION

Assessment of the data compiled for this thesis imply different interpretations for the timing and process of amalgamation of the SCB when compared with previous studies. Table 7.1 and Table 7.2 summarized these differences and the most important constraints relevant to development of the SCB.

Table 7.1. Important difference in interpretations derived in this thesis relative to previous publications.

	Time (Ma)	**Amalgamation process originally proposed**	**Revised interpretation (this thesis)**
Li et al 2008	1000-900	SCB situated in interior of Rodinia, implying earlier amalgamation	Amalgamation from 900 to 820 Ma at margin or separate from Rodinia
Zhang et al 2013	900-800	Scissor-style closing. The orogenic belt first appears at west of Jiangnan Orogen and propagates to the east	No progressive younging of igneous activity from SW to NE Jiangnan Orogen, implying simultaneous convergence throughout the Jiangnan Orogen
Zhang et al 2015b	900-800	Subduction direction swap. Yangtze initially as the lower plate, then swaps to upper plate	Igneous activity concentrated on the Yangtze block throughout this time period, implying that the Yangtze block was consistently in the upper plate.
Wilhem et al 2012	500-400	Amalgamation only occurred at ~460 Ma	Extensive juvenile, volcanic arc and MORB activity at 900-820 Ma implies older amalgamation. No juvenile igneous activity at 500-400 Ma. This younger magmatism is associated with structural inversion, possibly related to collision of the SCB with Gondwana.

The most important characteristics which assist in assessing various models for development of the SCB include: the presence of mid-ocean ridge mafic volcanics, volcanic arc lithologies and juvenile magmatic activity. The presence or absence of these characteristics are listed in Table 7.2 for the five main episodes of magmatism evident in the SCB.

Table 7.2. Major distinguishing features related to eposodes of magmatic and tectonic development of the SCB

	900-800 Ma	**440-380 Ma**	**220-200 Ma**	**160-150 Ma**	**150-0 Ma**
MORB	√	×	×	×	×
VAG	√	√	√	√	√
Syn-collisional	×	√	√	√	√
Reworked	√	√	√	√	√
Juvenile	√	×	×	×	×

The extensive compilation of regional data for the SCB described in this thesis provides a more consistent picture for its development when compared with interpretations based on studies of small areas. Igneous and metamorphic geochronology, isotope geochemistry, lithochemistry and detrital zircon geochronology suggest similar, internally consistent interpretations. This thesis shows that the Yangtze and Cathaysia blocks amalgamated between 900 and 820 Ma to form the South China block. Paleozoic igneous and metamorphic activity was not due to the amalgamation of the SCB, but rather because of the collision of the SCB with the Australian section of Gondwana. A distinctive detrital zircon age population is evident in sediments formed just after collision of the SCB with the NCB, consistent with rapid exhumation and erosion of eclogite grade metamorphic lithologies.

All data compiled for this thesis have been compiled in the online StratDB and DateView databases so that future researchers may easily build on the previously published information.

REFERENCES

Bickford, M.E., Van Schmus, W.R., Karlstrom, K.E., Mueller, P.A., Kamenov, G.D., 2015. Mesoproterozoic-trans-Laurentian magmatism: A synthesis of continent-wide age distributions, new SIMS U–Pb ages, zircon saturation temperatures, and Hf and Nd isotopic compositions. Precambrian Research, The structural, metamorphic and magmatic evolution of Mesoproterozoic orogens 265, 286–312. https://doi.org/10.1016/j.precamres.2014.11.024

Bouvier, A., Vervoort, J.D., Patchett, P.J., 2008. The Lu–Hf and Sm–Nd isotopic composition of CHUR: Constraints from unequilibrated chondrites and implications for the bulk composition of terrestrial planets. Earth and Planetary Science Letters 273, 48–57. https://doi.org/10.1016/j.epsl.2008.06.010

Cawood, P.A., Hawkesworth, C.J., Dhuime, B., 2012. Detrital zircon record and tectonic setting. Geology 40, 875–878. https://doi.org/10.1130/G32945.1

Champion, D.C., Huston, D.L., 2016. Radiogenic isotopes, ore deposits and metallogenic terranes: Novel approaches based on regional isotopic maps and the mineral systems concept. Ore Geology Reviews 76, 229–256. https://doi.org/10.1016/j.oregeorev.2015.09.025

Chen, K., Gao, S., Wu, Y.B., Guo, J.L., Hu, Z.C., Liu, Y.S., Zong, K.Q., Liang, Z.W., Geng, X.L., 2013. 2.6–2.7Ga crustal growth in Yangtze craton, South China. Precambrian Research 224, 472–490. https://doi.org/10.1016/j.precamres.2012.10.017

Chen, X., Wang, D., Wang, X.L., Gao, J.F., Shu, X.J., Zhou, J.C., Qi, L., 2014. Neoproterozoic chromite-bearing high-Mg diorites in the western part of the Jiangnan orogen, southern China: Geochemistry, petrogenesis and tectonic implications. Lithos 200–201, 35–48. https://doi.org/10.1016/j.lithos.2014.04.007

Chen, X.Y., Liu, J.L., Fan, W.K., Qi, Y.C., Wang, W., Chen, J.F., Burg, J.P., 2017. Neoproterozoic granitoids along the Ailao Shan-Red River belt: Zircon U-Pb geochronology, Hf isotope analysis and tectonic implications. Precambrian Research 299, 244–263. https://doi.org/10.1016/j.precamres.2017.06.024

DePaolo, D.J., 1981. Neodymium isotopes in the Colorado Front Range and crust–mantle evolution in the Proterozoic. Nature 291, 193–196. https://doi.org/10.1038/291193a0

Dickin, A.P., 2005. Radiogenic Isotope Geology, 2nd ed. Cambridge University Press.

Eglington, B.M., 2018a. FitPDF : a program to calculate and graph probability curves for data measurements with uncertainties. Saskatchewan Isotope Laboratory, Saskatoon, Canada, pp. 1–17.

Eglington, B.M., 2018b. Working with the DateView, StratDB and DepIso databases and web interfaces. Saskatchewan Isotope Laboratory, Saskatoon, Canada, pp. 1–47.

Eglington, B.M., 2018c. Geodate for windows version 4: isotope regression and modelling software. Saskatchewan Isotope Laboratory, Saskatoon, Canada, pp. 1–17.

Eglington, B.M., Meek, D.M., Mao, Y.X., in press. Detrital zircon probability visualisation and provenance identification utilising data mining, in: Applied Isotope Geochemistry, Topics in Mineral Sciences. Mineralogical Association of Canada.

Enkin, R.J., Yang, Z.Y., Chen, Y., Courtillot, V., 1992. Paleomagnetic constraints on the geodynamic history of the major blocks of China from the Permian to the present. Journal of Geophysical Research: Solid Earth 97, 13953–13989.

Faure, M., Lin, W., Breton, N.L., 2001. Where is the North China–South China block boundary in eastern China? Geology 29, 119–122. https://doi.org/10.1130/0091-7613(2001)029<0119:WITNCS>2.0.CO;2

Griffin, W.L., Pearson, N.J., Belousova, E., Jackson, S.E., van Achterbergh, E., O'Reilly, S.Y., Shee, S.R., 2000. The Hf isotope composition of cratonic mantle: LAM-MC-ICPMS analysis of zircon megacrysts in kimberlites. Geochimica et Cosmochimica Acta 64, 133–147. https://doi.org/10.1016/S0016-7037(99)00343-9

Griffin, W.L., Wang, X., Jackson, S.E., Pearson, N.J., O'Reilly, S.Y., Xu, X., Zhou, X., 2002. Zircon chemistry and magma mixing, SE China: In-situ analysis of Hf isotopes, Tonglu and Pingtan igneous complexes. Lithos, Magmatic Processes: A special issue in honor of R.H. Vernon 61, 237–269. https://doi.org/10.1016/S0024-4937(02)00082-8

Hoskin, P.W.O., Schaltegger, U., 2003. The Composition of Zircon and Igneous and Metamorphic Petrogenesis. Reviews in Mineralogy and Geochemistry 53, 27–62. https://doi.org/10.2113/0530027

Hsü, K.J., Li, J., Chen, H., Wang, Q., Sun, S., Şengör, A.M.C., 1990. Tectonics of South China: Key to understanding West Pacific geology. Tectonophysics, Geodynamic evolution of the Eastern Eurasian Margin 183, 9–39. https://doi.org/10.1016/0040-1951(90)90186-C

Hu, F.Y., Liu, S.W., Santosh, M., Deng, Z.B., Wang, W., Zhang, W.Y., Yan, M., 2016. Chronology and tectonic implications of Neoproterozoic blocks in the South Qinling Orogenic Belt, Central China. Gondwana Research, Tectonic evolution of the Qinling orogen and adjacent orogenic belts 30, 24–47. https://doi.org/10.1016/j.gr.2015.01.006

Huntington, K.W., Klepeis, K.A., 2018. Challenges and opportunities for research in tectonics: Understanding deformation and the processes that link Earth systems, from geologic time to human time. A community vision document submitted to the U.S. National Science Foundation.

Li, J.Y., Wang, X.L., Zhang, F.F., Zhou, X.H., Shu, X.J., 2016. A rhythmic source change of the Neoproterozoic basement meta-sedimentary sequences in the Jiangnan Orogen: Implications for tectonic evolution on the southeastern margin of the Yangtze Block. Precambrian Research 280, 46–60. https://doi.org/10.1016/j.precamres.2016.04.012

Li, L.M., Lin, S.F., Xing, G.F., Davis, D.W., Davis, W.J., Xiao, W.J., Yin, C.Q., 2013. Geochronology and geochemistry of volcanic rocks from the Shaojiwa Formation and Xingzi Group, Lushan area, SE China: Implications for Neoproterozoic back-arc basin in the Yangtze Block. Precambrian Research 238, 1–17. https://doi.org/10.1016/j.precamres.2013.09.016

Li, L.M., Lin, S.F., Xing, G.F., Davis, D.W., Jiang, Y., Davis, W., Zhang, Y.J., 2016. Ca. 830Ma back-arc type volcanic rocks in the eastern part of the Jiangnan orogen: Implications for the Neoproterozoic tectonic evolution of South China Block. Precambrian Research 275, 209–224. https://doi.org/10.1016/j.precamres.2016.01.016

Li, S.Z., Jahn, B., Zhao, S.J., Dai, L.M., Li, X.Y., Suo, Y.H., Guo, L.L., Wang, Y.M., Liu, X.C., Lan, H.Y., Zhou, Z.Z., Zheng, Q.L., Wang, P.C., 2017. Triassic southeastward subduction of North China Block to South China Block: Insights from new geological, geophysical and geochemical data. Earth-Science Reviews 166, 270–285. https://doi.org/10.1016/j.earscirev.2017.01.009

Li, X.H., Li, W.X., Li, Z.X., Lo, C.H., Wang, J., Ye, M.F., Yang, Y.H., 2009. Amalgamation between the Yangtze and Cathaysia Blocks in South China: Constraints from SHRIMP U–Pb zircon ages, geochemistry and Nd–Hf isotopes of the Shuangxiwu volcanic rocks. Precambrian Research 174, 117–128. https://doi.org/10.1016/j.precamres.2009.07.004

Li, X.H., Li, Z.X., Li, W.X., 2014. Detrital zircon U–Pb age and Hf isotope constrains on the generation and reworking of Precambrian continental crust in the Cathaysia Block, South China: A synthesis. Gondwana Research 25, 1202–1215. https://doi.org/10.1016/j.gr.2014.01.003

Li, Z.X., 2014. A Tectonic Overview of the South China Block, in: Tectonics of the South China Block. Science Press, pp. 1–35.

Li, Z.X., Bogdanova, S.V., Collins, A.S., Davidson, A., De Waele, B., Ernst, R.E., Fitzsimons, I.C.W., Fuck, R.A., Gladkochub, D.P., Jacobs, J., Karlstrom, K.E., Lu, S., Natapov, L.M., Pease, V., Pisarevsky, S.A., Thrane, K., Vernikovsky, V., 2008. Assembly, configuration, and break-up history of Rodinia: A synthesis. Precambrian Research, Testing the Rodinia Hypothesis: Records in its Building Blocks 160, 179–210. https://doi.org/10.1016/j.precamres.2007.04.021

Li, Z.X., Li, X.H., Kinny, P.D., Wang, J., Zhang, S., Zhou, H., 2003. Geochronology of Neoproterozoic syn-rift magmatism in the Yangtze Craton, South China and correlations with other continents: evidence for a mantle superplume that broke up Rodinia. Precambrian Research, Precambrian tectonics of East Asia and relevance to supercontintent evolution 122, 85–109. https://doi.org/10.1016/S0301-9268(02)00208-5

Liu, C., Knoll, A.H., Hazen, R.M., 2017. Geochemical and mineralogical evidence that Rodinian assembly was unique. Nature Communications 8, 1950. https://doi.org/10.1038/s41467-017-02095-x

Liu, Q., Yu, J.H., Wang, Q., Su, B., Zhou, M.F., Xu, H., Cui, X., 2012. Ages and geochemistry of granites in the Pingtan–Dongshan Metamorphic Belt, Coastal South China: New constraints on Late Mesozoic magmatic evolution. Lithos 150, 268–286. https://doi.org/10.1016/j.lithos.2012.06.031

Ludwig, K.R., 2012. User's Manual for Isoplot 3.75: A Geochronological Toolkit for Microsoft Excel. Berkeley Geochronological Center.

Ma, L.F., Qiao, X.F., Liu, N.L., 2002. Geological Atlas of China.

Pearce, J.A., 2014. Immobile Element Fingerprinting of Ophiolites. Elements 10, 101–108. https://doi.org/10.2113/gselements.10.2.101

Pearce, J.A., 2008. Geochemical fingerprinting of oceanic basalts with applications to ophiolite classification and the search for Archean oceanic crust. Lithos, Links Between Ophiolites and LIPs in Earth History 100, 14–48. https://doi.org/10.1016/j.lithos.2007.06.016

Pearce, J.A., 1996a. A User's Guide to Basalt Discrimination Diagrams.

Pearce, J.A., 1996b. Sources and Settings of Granitic Rocks.

Pearce, J.A., 1983. Role of the sub-continental lithosphere in magma genesis at active continental margins, in: Hawkesworth, C.J., Norry, M.J. (Eds.), Continental Basalts and Mantle Xenoliths. Shiva Publications, Nantwich, Cheshire, pp. 230–249.

Pearce, J.A., Harris, N.B.W., Tindle, A.G., 1984. Trace Element Discrimination Diagrams for the Tectonic Interpretation of Granitic Rocks. J Petrology 25, 956–983. https://doi.org/10.1093/petrology/25.4.956

Petrov, O.V., Leonov, Y.G., Li, T.D., Tomurtogoo, O., 2014. Tectonic map of Northern, Central and Eastern Asia - CCGM - CGMW [WWW Document]. URL

https://ccgm.org/en/maps/172-tectonic-map-of-northern-central-and-eastern-asia-9785937612151.html (accessed 10.9.18).
Qiu, X.F., Ling, W.L., Liu, X.M., Lu, S.-S., Jiang, T., Wei, Y.X., Peng, L.H., Tan, J.J., 2018. Evolution of the Archean continental crust in the nucleus of the Yangtze block: Evidence from geochemistry of 3.0 Ga TTG gneisses in the Kongling high-grade metamorphic terrane, South China. Journal of Asian Earth Sciences 154, 149–161. https://doi.org/10.1016/j.jseaes.2017.12.026
Ren, J.S., 2013. International Geological Map of Asia at 1:5 M (IGMA) - CCGM - CGMW [WWW Document]. URL https://ccgm.org/en/home/160-international-geological-map-of-asia-at-15-m-igma-9787116083646.html (accessed 10.9.18).
Rollinson, H.R., 2014. Using Geochemical Data: Evaluation, Presentation, Interpretation. Routledge.
Rubatto, D., 2017. Zircon: The Metamorphic Mineral. Reviews in Mineralogy and Geochemistry 83, 261–295. https://doi.org/10.2138/rmg.2017.83.9
Schmidt, A., Mezger, K., O'Brien, P.J., 2011. The time of eclogite formation in the ultrahigh pressure rocks of the Sulu terrane: Constraints from Lu–Hf garnet geochronology. Lithos 125, 743–756. https://doi.org/10.1016/j.lithos.2011.04.004
Sewell, R.J., Carter, A., Rittner, M., 2016. Middle Jurassic collision of an exotic microcontinental fragment: Implications for magmatism across the Southeast China continental margin. Gondwana Research 38, 304–312. https://doi.org/10.1016/j.gr.2016.01.005
Spencer, C.J., Kirkland, C.L., Taylor, R.J.M., 2016. Strategies towards statistically robust interpretations of in situ U–Pb zircon geochronology. Geoscience Frontiers 7, 581–589. https://doi.org/10.1016/j.gsf.2015.11.006
Vermeesch, P., 2012. On the visualisation of detrital age distributions. Chemical Geology 312–313, 190–194. https://doi.org/10.1016/j.chemgeo.2012.04.021
Vervoort, J.D., 2014. Lu-Hf Dating: The Lu-Hf Isotope System, in: Rink, W.J., Thompson, J. (Eds.), Encyclopedia of Scientific Dating Methods. Springer Netherlands, pp. 1–20. https://doi.org/10.1007/978-94-007-6326-5_46-1
Vervoort, J.D., Plank, T., Prytulak, J., 2011. The Hf–Nd isotopic composition of marine sediments. Geochimica et Cosmochimica Acta 75, 5903–5926. https://doi.org/10.1016/j.gca.2011.07.046
Wang, C., Liang, X.Q., Xie, Y.H., Tong, C.X., Pei, J., Zhou, Y., Jiang, Y., Fu, J.G., Dong, C.G., Liu, P., 2014. Provenance of Upper Miocene to Quaternary sediments in the Yinggehai-Song Hong Basin, South China Sea: Evidence from detrital zircon U–Pb ages. Marine Geology 355, 202–217. https://doi.org/10.1016/j.margeo.2014.06.004
Wang, J.Q., Shu, L.S., Santosh, M., Xu, Z.Q., 2015. The Pre-Mesozoic crustal evolution of the Cathaysia Block, South China: Insights from geological investigation, zircon U–Pb geochronology, Hf isotope and REE geochemistry from the Wugongshan complex. Gondwana Research 28, 225–245. https://doi.org/10.1016/j.gr.2014.03.008
Wang, L., Kusky, T.M., Polat, A., Wang, S., Jiang, X., Zong, K., Wang, J., Deng, H., Fu, J., 2014. Partial melting of deeply subducted eclogite from the Sulu orogen in China. Nature Communications 5, 5604. https://doi.org/10.1038/ncomms6604
Wang, T., Zhang, J.J., Zhang, L., Li, S., Guo, L., Tong, Y., 2018. Evolution of Late Mesozoic granitoids in NE Asia: evidence for early-stage low-angle subduction and late-stage roll-back of Paleo-Pacific Plate. Presented at the RFG2018.

Wang, X.L., Zhao, G.C., Zhou, J.C., Liu, Y.S., Hu, J., 2008. Geochronology and Hf isotopes of zircon from volcanic rocks of the Shuangqiaoshan Group, South China: Implications for the Neoproterozoic tectonic evolution of the eastern Jiangnan orogen. Gondwana Research 14, 355–367. https://doi.org/10.1016/j.gr.2008.03.001

Wang, X.L., Zhou, J.C., Qiu, J.S., Zhang, W.L., Liu, X.M., Zhang, G.L., 2006. LA-ICP-MS U-Pb zircon geochronology of the Neoproterozoic igneous rocks from Northern Guangxi, South China: Implications for tectonic evolution. Precambrian Research 145, 111–130. https://doi.org/10.1016/j.precamres.2005.11.014

Wilhem, C., Windley, B.F., Stampfli, G.M., 2012. The Altaids of Central Asia: A tectonic and evolutionary innovative review. Earth-Science Reviews 113, 303–341. https://doi.org/10.1016/j.earscirev.2012.04.001

Wu, Y.B., Zheng, Y.F., Zhou, J.B., 2004. Neoproterozoic granitoid in northwest Sulu and its bearing on the North China-South China Blocks boundary in east China. Geophys. Res. Lett. 31, L07616. https://doi.org/10.1029/2004GL019785

Xia, Y., Xu, X.S., Zhao, G.C., Liu, L., 2015. Neoproterozoic active continental margin of the Cathaysia block: Evidence from geochronology, geochemistry, and Nd–Hf isotopes of igneous complexes. Precambrian Research 269, 195–216. https://doi.org/10.1016/j.precamres.2015.08.006

Yakymchuk, C., Kirkland, C.L., Clark, C., 2018. Th/U ratios in metamorphic zircon. Journal of Metamorphic Geology 36, 715–737. https://doi.org/10.1111/jmg.12307

Yao, W.H., Li, Z.X., 2016. Tectonostratigraphic history of the Ediacaran–Silurian Nanhua foreland basin in South China. Tectonophysics 674, 31–51. https://doi.org/10.1016/j.tecto.2016.02.012

Yao, W.H., Li, Z.X., Li, W.X., Li, X.H., 2017. Proterozoic tectonics of Hainan Island in supercontinent cycles: New insights from geochronological and isotopic results. Precambrian Research 290, 86–100. https://doi.org/10.1016/j.precamres.2017.01.001

Yu, J.H., Zhang, C.H., O'Reilly, S.Y., Griffin, W.L., Ling, H.F., Sun, T., Zhou, X.Y., 2017. Basement components of the Xiangshan-Yuhuashan area, South China: Defining the boundary between the Yangtze and Cathaysia blocks. Precambrian Research. https://doi.org/10.1016/j.precamres.2017.05.017

Zhang, C.L., Santosh, M., Zou, H.B., Li, H.K., Huang, W.C., 2013. The Fuchuan ophiolite in Jiangnan Orogen: Geochemistry, zircon U–Pb geochronology, Hf isotope and implications for the Neoproterozoic assembly of South China. Lithos 179, 263–274. https://doi.org/10.1016/j.lithos.2013.08.015

Zhang, S.H., Li, H.Y., Jiang, G.Q., Evans, D.A.D., Dong, J., Wu, H.C., Yang, T.S., Liu, P.J., Xiao, Q.., 2015a. New paleomagnetic results from the Ediacaran Doushantuo Formation in South China and their paleogeographic implications. Precambrian Research 259, 130–142. https://doi.org/10.1016/j.precamres.2014.09.018

Zhang, Y.Z., Wang, Y.J., Zhang, Y.H., Zhang, A.M., 2015b. Neoproterozoic assembly of the Yangtze and Cathaysia blocks: Evidence from the Cangshuipu Group and associated rocks along the Central Jiangnan Orogen, South China. Precambrian Research 269, 18–30. https://doi.org/10.1016/j.precamres.2015.08.003

Zhao, X.F., Zhou, M.F., Li, J.W., Sun, M., Gao, J.F., Sun, W.H., Yang, J.H., 2010. Late Paleoproterozoic to early Mesoproterozoic Dongchuan Group in Yunnan, SW China: Implications for tectonic evolution of the Yangtze Block. Precambrian Research 182, 57–69. https://doi.org/10.1016/j.precamres.2010.06.021

Zhou, J.C., Wang, X.L., Qiu, J.S., 2009. Geochronology of Neoproterozoic mafic rocks and sandstones from northeastern Guizhou, South China: Coeval arc magmatism and sedimentation. Precambrian Research 170, 27–42. https://doi.org/10.1016/j.precamres.2008.11.002